

Particle Phenomenology of Gravitational Events at the TeV Scale

A Dissertation

Presented for the

Doctor of Philosophy

Degree

The University of Mississippi

Arunava Roy

June 2009

*“Fill the brain with high thoughts, highest ideals, place them day and night
before you, and out of that will come great work”*
Vivekananda, Philosopher, 12th January 1863 – 4th July 1902

Acknowledgments

I am grateful to the many people who have helped and encouraged me. I am particularly thankful to: my dissertation advisor, Marco Cavaglià, and the rest of my dissertation committee: Lucien Cremaldi, Neil Manson and Don Summers.

Luis A. Anchordoqui, Alakabha Datta, Romulus Godang and David Sanders for fruitful discussions; Peter Skands and Xerxes Tata for help with simulation software.

My parents, Tapan and Swapna; my brother and sister-in-law, Amitava and Debjani; and my nephew Aarush.

Finally, I would also like to thank my wife, Baishali, for her constant encouragement and support.

Abstract

If the fundamental scale of gravity is of the order of 1 TeV, black holes might be produced at the Large Hadron Collider. This work presents simulations of black holes and other exotic models of physics beyond the Standard Model - supersymmetry, extra dimensional models and string theory. Isolated leptons with high transverse momenta can be used to distinguish black holes from supersymmetry and models of extra dimensions. Z^0 bosons and photons with high transverse momenta allow the discrimination of black holes and string resonances. The analysis of visible and missing energy/momenta and event shape variables complement these techniques.

Contents

Introduction	1
1 Physics of the Standard Model and Beyond	4
1.1 The Standard Model	4
1.2 Physics beyond the Standard Model	6
1.3 Supersymmetry	7
1.4 Extra-dimensional Models	10
1.4.1 Kaluza-Klein Reduction	13
1.4.2 ADD	14
1.4.3 RS	17
1.5 Black hole production	18
1.6 String Resonances	23
2 Physics of Particle Collisions	27
2.1 The Large Hadron Collider	27
2.2 Luminosity	30
2.3 Event Shape variables	31
2.4 Invariant Mass and Jet Masses	32
3 Simulation Techniques	33
4 Phenomenology of New Physics at the LHC	39
4.1 SUSY and BH event analysis	39
4.1.1 Energy and Momentum	41
4.1.2 Event shape variables	42
4.1.3 High- P_T leptons	44

4.2	ED and BH Event Analysis	57
4.2.1	Energy, Momentum and Event shape variables	57
4.2.2	High- P_T leptons	59
4.3	SR and SM Event Analysis	64
4.4	SR and BH Event Analysis	68
	Conclusions	69
	Bibliography	70
	Appendix A: Units	85
	Appendix B: Acronyms	86
	Appendix C: Symbols	87

List of Tables

1.1	Charges and masses of the SM quarks [1]. Due to the asymptotic freedom structure of QCD, quarks and gluons are not capable of independent existence [2, 3, 4, 5] (and references therein). Therefore, quark masses are measured indirectly through their influence on hadrons. The computational scheme used to calculate the quark mass from experimental observations is the source of the uncertainty in their mass.	5
1.2	Charges and masses of the SM leptons [1].	5
1.3	Charges and masses of the SM bosons[1].	6
1.4	MSSM Parameters for typical LHC points. The first five points refer to ATLAS and LM1 refers to CMS (see Chapter 2). The scalar mass and the gaugino mass are given in GeV [6].	9
1.5	SUSY mass spectrum in GeV. The first two generations of squarks and sleptons are degenerate. Masses are computed using ISAJET (ver. 7.75) [7].	11
1.6	Cross section in fb for production of SUSY particles for the LHC points listed in Table 1.4 [8, 9, 10, 11].	12
1.7	LEP lower bounds on M_* and upper bounds on the size of the EDs as a function of the number of EDs for the ADD model.	16
1.8	BH radius as a function of n for a BH mass of $M=4$ TeV.	19
1.9	BH temperature and lifetime as a function of n for a BH with mass $M=4M_*=4$ TeV.	22
3.1	Abridged PYTHIA output showing a pp collision to produce a graviton (G^*). Orig refers to where the current particle originated from. Other symbols have the usual meaning. All quantities are in GeV.	36
3.2	Dof's of the known SM particles, Higgs and the graviton.	37

4.1	BRs of high- P_T isolated dileptons for SUSY and BH models. 21,000 and 100,000 events were simulated in the two cases, respectively, yielding approximately 1000 dilepton events. OS(SS) stands for opposite (same) sign and OF(SF) denotes opposite (same) flavor.	50
4.2	BRs of high- P_T isolated dileptons for SUSY points B and C for 50,000 events. The high value of $\tan\beta=10$ for point C manifests itself as a greater production of OSSF dileptons.	52
4.3	BRs of high- P_T isolated dileptons for the RS and the BH models. Respectively 2.8×10^4 and 10^6 events were simulated in the two cases, yielding approximately 1000 dilepton events.	63
4.4	Angular distributions of Z' boson and graviton decay into di-electrons. θ is the angle between the beam direction and the electron in the rest frame of the resonance.	63
1	Fundamental constants.	85
2	Conversion factors.	85

List of Figures

1	The energy of electron-positron and hadron colliders constructed (filled circles and squares) or in the planning stage [12]. . . .	2
1.1	Gauge couplings as a function of the energy in SM (left panel) and SUSY (right panel). The relative width of each line reflects current experimental uncertainties. Reproduced from [13]. . .	8
1.2	Five ATLAS points (large dots) shown in the $m_0 - m_{1/2}$ plane along with lines of constant squark and gluon mass. The shaded regions are excluded because of theoretical/experimental constraints. Reproduced from [14].	10
1.3	Typical SUSY cascade decay in a hadronic process (pp). . . .	12
1.4	Compactified extra dimension of radius R (dotted line). The solid line denotes 4D spacetime. Adapted from [15].	13
1.5	Gravitational lines of force between the two test masses leaks into the EDs. This leads to gravity being weaker on the brane. Adapted from [15]	14
1.6	RS model of EDs. The fifth extra dimension is warped leading to the weakness of gravity on our brane. SM fields are restricted to the TeV brane. The graviton can propagate in the extra dimension.	17
1.7	Mass of the first graviton excitation m_1 versus c for $kr=10$ (solid red line), 11 (dashed green line) and 12 (dotted blue line). . .	18
1.8	The u and v lines represent two shock waves moving in opposite directions, colliding at $u=v=0$. Region I is before the collision. Regions II and III are linear. Region IV is highly non-linear and curved, a closed trapped surface is formed. The BH is formed in this region.	20
1.9	Left Panel: BH cross section for different numbers of extra spatial dimensions as a function of the CM energy. The fundamental scale M_* is assumed to be 1 TeV. Right Panel: BH cross section for $M_*=1$ TeV (dashed) and $M_*=2$ TeV (dotted). . . .	21

1.10	Left Panel: BH mass for different values of M_\star . Right Panel: BH mass for different values of extra spatial dimensions, n . Both plots are for 10000 events.	22
1.11	Illustration of the Schwarzschild evaporation of a BH, showing brane and bulk emission [16]. SM particles are emitted on the brane. The graviton escapes both in the brane and bulk. . . .	23
1.12	Differential cross section of string events for $M_s= 1$ TeV (red dots) and $M_s= 2$ TeV (green crosses) with $P_{Tmin}=50$ GeV. SRs are clearly seen when $\hat{s} = nM_s^2$	25
1.13	Left panel: String cross section for $M_s= 1$ TeV (red dots) and $M_s= 2$ TeV (green crosses). The cross section for $M_s= 1$ TeV is ~ 44 times larger than the cross section for $M_s= 2$ TeV. Right panel: String cross section for the two extreme values of P_{Tmin} , 50 GeV (solid red line) and 300 GeV (dashed green line) as a function of M_\star	26
2.1	Illustration of the LHC ring structure showing four of the six experiments. The energy of the protons is increased in succession by the use of various smaller accelerators. Protons, first injected into LINAC, are emitted with an energy of 50 GeV. Next, the PS booster accelerates the protons to 1.4 GeV before it enters the Proton Synchrotron (PS). 25 GeV protons from PS is fed to the SPS (Super Proton Synchrotron), accelerating them more than 10 times their present energy to 450 GeV. In the final phase, the protons enter the LHC where they reach their final energy of 7 TeV per beam. Adapted from [17]. . . .	27
2.2	Cross section of the ATLAS and CMS [18] detectors at CERN.	29
2.3	Passage of charged particles through matter in particle colliders. Charged particles leave a track in the tracking chamber, neutral particles shower without leaving a track. Neutrinos are undetected. Adapted from [17].	30
3.1	2×2 interaction showing initial and final state radiation, multiple interactions and beam remnants. Adapted from [19]. . .	35
4.1	Comparison of visible energy (top left), \cancel{P}_T (top right) and sphericity (bottom) for 10000 events for the five ATLAS points of Table 1.4 (A: filled black circles, B: filled red squares, C: filled green triangles, D: open blue circles and E: open pink squares).	40

4.2	Comparison of 10,000 SUSY and BH benchmark events at the LHC. Visible energy and \cancel{P}_T (top panels) are comparable due to the presence of invisible channels in both models. Leptons with large P_T provide instead an effective discriminator (bottom right panel).	42
4.3	Distribution of visible energy, \cancel{P}_T and transverse momenta of leptons and hadrons & photons. SUSY plots are shown as pink open squares. The four plots show the effect of different decay modes in the Planck phase of ten-dimensional BHs: remnant formation ($n_p = 0$, black filled triangles), two-body decay ($n_p = 2$, red filled circles) and four-body decay ($n_p = 4$, green filled squares). The fundamental Planck scale is $M_\star = 1$ TeV.	43
4.4	Distribution of visible energy, \cancel{P}_T and transverse momenta of leptons and hadrons & photons. SUSY plots are shown as pink open squares. The plots show the effect of varying the fundamental Planck scale: $M_\star = 1$ TeV (black filled triangles), $M_\star = 2$ TeV (red filled circles) and $M_\star = 3$ TeV (green filled squares). The ten-dimensional BHs decay in two hard quanta at the end of the evaporation phase.	44
4.5	Sphericity (top panels), 2 nd Fox-Wolfram moment (middle panels) and thrust (bottom panels) for 10,000 BH and SUSY events. The left panels show the effect of different Planckian decay modes: BH remnant (black filled triangles), two-body decay (red filled circles) and four-body decay (green filled squares). The fundamental scale is $M_\star = 1$ TeV and the number of EDs $n=6$. The right panels show the effect of different fundamental scales: $M_\star = 1$ TeV (black filled triangles), 2 TeV (red filled circles) and 3 TeV (green filled squares). The ten-dimensional BHs decay in two quanta at the end of the Hawking phase. . .	45
4.6	Heavy and light jet masses (top and middle panels) and number of jets (bottom panels) for 10,000 BH and MSSM events. Symbols are like in previous figures.	46
4.7	The top three SUSY decay chains at point A and their branching ratios.	47
4.8	Invariant mass distribution (in GeV) for 2000 SUSY and BH OSSF dilepton events for point A. The SUSY distribution (shaded pink histogram) shows the typical endpoint due to the presence of the LSP. The high- P_T tail of the BH distribution is originated by uncorrelated lepton pairs emitted during the Hawking evaporation phase. The final BH decay is in two-quanta. The SM background is negligible.	49

4.9	Invariant mass distribution for 900 same-sign dilepton events at point A. The SM background is negligible.	50
4.10	Invariant mass distribution for 1100 OSOF dilepton events at point A. The SM background is negligible.	51
4.11	Histogram of the number of events with high- P_T leptons for 10,000 MSSM (pink filled squares) and BH interactions (black open triangles). The number of BH events with three isolated leptons is smaller than the number of SUSY events by a factor of ~ 20 . The probability of producing BH events with four or more leptons is virtually zero.	52
4.12	P_T scatter plot for ~ 1000 isolated opposite-flavor dilepton events for SUSY (pink filled squares) and BHs (black open triangles). BH leptons are harder than SUSY leptons and show a larger spread in P_T	53
4.13	Invariant mass distributions at point B (left panels) and point C (right panels). OSSF (top panels), SS (middle panels) and OSOF (bottom panels) distributions clearly discriminate SUSY and BH events.	54
4.14	Invariant mass distributions at point D (left panels) and point E (right panels). Top Panel: Distribution of 2000 SUSY and BH OSSF dilepton events. At point E there is enhanced Z^0 production because of a high value of $\tan\beta$. Middle Panel: Event distribution for ~ 1700 SUSY and BH SS dilepton events. The SM background is negligible. Bottom Panel: SUSY and BH distribution for ~ 2600 OSOF events. The major SM background due to $\bar{t}t$ is negligible.	55
4.15	Top Left Panel: Invariant mass distribution for SUSY and BH OSSF dilepton events for the CMS benchmark point LM1. Likewise to point A, the SUSY distribution shows the endpoint due to the presence of the LSP. Top Right Panel: invariant mass distribution for same sign dileptons. Bottom Panel: OSOF invariant mass distribution. A high value of $\tan\beta$ enhances the production of OSOF dileptons as explained in the text.	56
4.16	Comparison of 10,000 RS graviton and BH benchmark events. Visible energy and \cancel{P}_T (top panels) are comparable due to the presence of invisible channels in both models. Bottom panels show visible P_T due to leptons (left panel) and photons and hadrons (right panel).	57

4.17	Distribution of visible energy, P_T and transverse momenta of leptons and hadrons & photons. RS graviton plots are shown as pink open squares. The four plots show the effect of different decay modes in the Planck phase of ten-dimensional BHs: remnant formation ($n_p = 0$, black filled triangles), two-body decay ($n_p = 2$, red filled circles) and four-body decay ($n_p = 4$, green filled squares). The fundamental Planck scale is $M_\star = 1$ TeV.	58
4.18	Distribution of visible energy, P_T and transverse momenta of leptons and hadrons & photons. RS graviton results are shown as pink open squares. The four plots show the effect of varying the fundamental Planck scale: $M_\star = 1$ TeV (black filled triangles), $M_\star = 2$ TeV (red filled circles) and $M_\star = 3$ TeV (green filled squares). The ten-dimensional BHs decay in two hard quanta at the end of the evaporation phase.	59
4.19	Sphericity (top panels) and 2 nd Fox-Wolfram moment (middle panels) and thrust (bottom panels) for 10,000 BH and graviton events (pink open squares). The left panels show the effect of different Planckian decay modes: BH remnant (black filled triangles), two-body decay (red filled circles) and four-body decay (green filled squares). The fundamental scale is $M_\star = 1$ TeV and the number of EDs is six. The right panels show the effect of different fundamental scales: $M_\star = 1$ TeV (black filled triangles), 2 TeV (red filled circles) and 3 TeV (green filled squares). Here, the ten-dimensional BHs decay in two quanta at the end of the Hawking phase.	60
4.20	Heavy and light jet masses (top and middle panels) and number of jets (bottom panels) for 10,000 BH and graviton events. Symbols are like in previous figures.	61
4.21	Invariant mass distribution of 1100 OSOF dilepton events. Most high- P_T leptons in the RS model come from the decay of the graviton and Z^0 bosons. This is indicated by the two peaks in the invariant mass distribution. As discussed before in Sect. 4.1, the BH distribution is also characterized by two peaks. The discriminating signature is the high- P_T tail in the BH invariant mass distribution.	62
4.22	Angular distributions of electron from Z' and graviton decays.	63

4.23	Top panel: Visible energy distribution for string+SM and SM only events. The result for string events is shown by the solid red histogram ($M_s=1$ TeV) and the dashed green histogram ($M_s=2$ TeV). String events can be identified from the high- E_T tail for $M_s=1$ TeV. Bottom panel: Distribution of visible P_T for γ +hadrons. The high- P_T tail is a strong indicator of the presence of SR.	65
4.24	Top panel: Distribution of the highest $P_{T,\gamma}$ for each event. γ 's with high P_T created in the string decay are the source of the long tail. Bottom panel: Dijet invariant mass distribution. String decays may result in large invariant mass.	66
4.25	Histograms of event shape variables for 10 million string+SM and SM only events. String events are shown in solid red ($M_s=1$ TeV) and dashed green ($M_s=2$ TeV). SM events are shown in dotted blue. String events have on the average a slightly higher sphericity than SM events due to the slight increase in the number of jets (top panel). Similar conclusions are reached from the heavy and low jet mass distributions (middle and bottom panels, respectively).	67
4.26	SNR for an integrated luminosity of 1300 fb^{-1} (solid red line) and 300 fb^{-1} (dashed green line), corresponding to 4 year and 1 year at an instantaneous luminosity of $10^{34}\text{ cm}^{-2}\text{ s}^{-1}$, respectively. .	68

Introduction

In 1964 the theory of quarks was formulated by M. Gell-Mann and G. Zweig [20, 21, 22, 23] and in 1979 S. Glashow, A. Salam, and S. Weinberg shared the Nobel Prize in Physics for their discovery of the electroweak theory [24]. Quantum electrodynamics (QED), the theory of weak interactions, and Quantum chromodynamics (QCD), the theory of the quark interactions form the basis of Standard Model (SM) of particle physics. Results from particle collider experiments, such as Large Electron Positron LEP (at CERN) and Fermilab Tevatron agree with the predictions of the SM to a very high precision. One of the major milestones in the experimental verification of the SM was the discovery of W^\pm and Z bosons by the SPS, UA1 and UA2 experiments at CERN [25, 26, 27, 28, 29].

The framework of the SM relies on the existence of an unobserved particle known as the Higgs boson, which was postulated in 1964 by R. Brout, F. Englert and P. Higgs [30, 31]. In the minimal SM the existence of the Higgs particle is required to generate the masses of all other particles. Many questions, however, remain unanswered. The SM does not explain why there are three quark generations, it does not address charge-parity (CP) violation, it does not provide a viable candidate for dark matter, and finally it does not incorporate the gravitational force. Various models such as extra dimensions (EDs) [32] and supersymmetry (SUSY) (see Ref. [33, 34] and references therein) have been proposed to overcome the drawbacks of the SM.

The center-of-mass (CM) energy of LEP was ~ 200 GeV. Tevatron's $p\bar{p}$ beams reach a maximum energy of 1 TeV. The upcoming Large Hadron Collider (LHC) [18], with 600 million collisions per second and a CM energy of 14 TeV, is supposed to provide an answer on some, if not all, of the open questions of the SM.

The most viable candidate of new physics beyond the SM is SUSY. SUSY provides an explanation for the Higgs mass problem, a candidate for cold dark matter, and unification of low energy gauge couplings by introducing superpartners to SM fields. The lightest supersymmetric particle (LSP) in SUSY is an ideal dark matter candidate: a massive, weakly interacting and neutral particle.

Models with large extra dimensions (LEDs) are an alternative to SUSY.

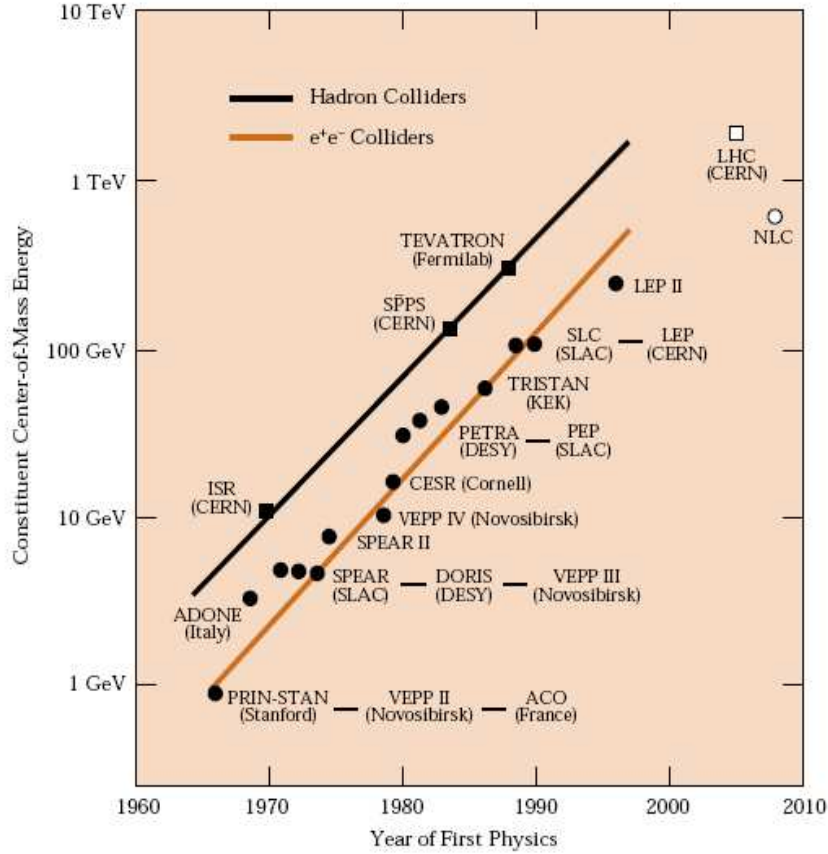


Figure 1: *The energy of electron-positron and hadron colliders constructed (filled circles and squares) or in the planning stage [12].*

LEDs provide a solution to the hierarchy problem. If they exist, gravity would become strong at the TeV scale. SUSY and LEDs are essential ingredients of string theory (ST). If ST happens to be the correct theory of physics at high energies, and LEDs do exist, the LHC could even start producing string resonances (SRs).

An interesting consequence of the presence of LEDs would be the production of micro black holes (BHs) in particle colliders [35, 36, 37, 38, 39, 40, 41, 42, 43, 44, 45, 46, 47, 48, 49, 50, 51, 52, 53, 54, 55, 56, 57, 58, 59, 60, 61, 62, 63, 64, 65, 66] (for reviews, see Refs. [16, 67, 68, 69, 70]) and Earth's atmosphere by cosmic rays [56, 57, 58, 59, 60, 61, 62, 63, 64, 65]. Production of Kaluza-Klein (KK) excitations of gravitons and SM [71, 72, 73] particles would also be consequences of EDs.

SUSY, LED models, KK excitations and ST lead to different physical signatures at the TeV scale. It is thus worthwhile to look into the means of

comparing these models [74]. Comparisons of SUSY and universal EDs/little Higgs models in colliders have been investigated in Refs. [75, 76, 77, 78, 79, 80]. However, the literature lacks comprehensive and quantitative comparisons of the various models of physics beyond the TeV scale.

The aim of this thesis is to show, in a quantitative way, how to distinguish BH events at the LHC from SUSY, graviton events and SRs. The original work of this thesis is based on Refs. [81, 82, 83]. SUSY, KK excitations and SRs can be distinguished from BHs by the use of kinematic and dynamical quantities. These methods will be discussed in detail in Chapter 4, where the original work of this thesis is included.

This thesis is organised as follows. The next chapter reviews the most important features of the SM and the various models of new physics above the TeV scale, known problems with the SM, and how new physics beyond the SM is supposed to overcome these problems. The physics of particle collisions is discussed in Chapter 2. Simulation techniques are presented in Chapter 3. Analysis and results are presented in Chapter 4. Finally, the last chapter provides some conclusions and discusses open issues. Notations, units, acronyms and symbols are included in the appendices.

Physics of the Standard Model and Beyond

In this chapter we briefly review the basics of the SM and of models of physics beyond the SM. The purpose of this chapter is to introduce concepts and notations for our analysis of new physics above the TeV scale of Chapter 4. The content of this chapter is by no means exhaustive. For a more comprehensive discussion of the SM and physics beyond the SM the reader is referred to [84, 85, 86] and references therein.

1.1 The Standard Model

The SM of particle physics describes the elementary particles and their interactions. The known elementary particles can be grouped into two categories: matter particles (fermions, half spin) and force carriers (bosons, integer spin). The particle content of the SM is shown in the figure below.

The matter particles can be further grouped into quarks and leptons which occur in three generations. The quarks are: up (u) and down (d) in the first generation, charm (c) and strange (s) in the second generation and top (t) and bottom (b) in the third generation. Quark's charges and masses are listed in Table 1.1. The leptons are the electron (e), muon (μ), tau (τ) and the corresponding neutrinos (ν_i), where i denotes e, μ or τ . The masses of leptons are listed in Table 1.2. The neutrinos are chargeless and have negligible mass. The electron and neutrinos are stable. Muons and taus have a lifetime of $\sim 10^{-6}$ and 10^{-15} seconds, respectively. Each matter particle in the SM is also accompanied by its corresponding antiparticle: antiparticles have equal mass and opposite charge of the corresponding particles. The bosons include the photon (γ), the W and Z^0 weak bosons, and eight massless gluons; these particles are the force mediators. The photon is the mediator of the electromagnetic force, the W, Z bosons mediate the weak nuclear force and the gluons carry the strong nuclear force (See Table 1.3.).

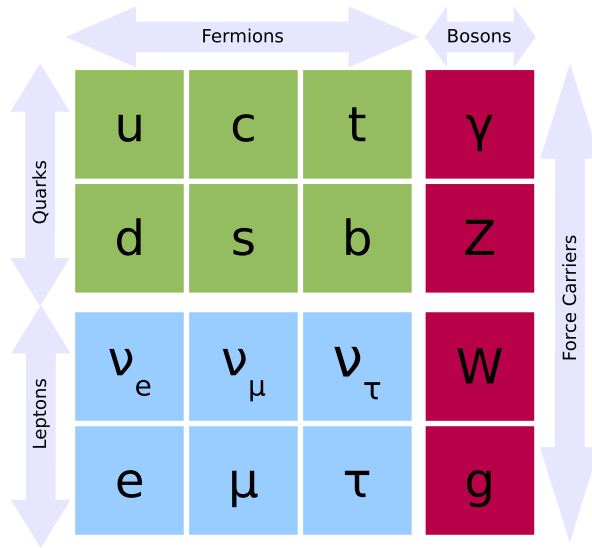


Table 1.1: Charges and masses of the SM quarks [1]. Due to the asymptotic freedom structure of QCD, quarks and gluons are not capable of independent existence [2, 3, 4, 5] (and references therein). Therefore, quark masses are measured indirectly through their influence on hadrons. The computational scheme used to calculate the quark mass from experimental observations is the source of the uncertainty in their mass.

	charge	mass (GeV)
u	$2/3$	0.002 to 0.008
d	$-1/3$	0.005 to 0.0015
c	$2/3$	3.38 to 3.48
s	$-1/3$	0.1 to 0.106
t	$2/3$	170 to 174
b	$-1/3$	4.1 to 4.5

Table 1.2: Charges and masses of the SM leptons [1].

	mass (MeV)
e^\pm	0.511 ± 0.000000013
μ^\pm	105.6 ± 0.000004 MeV
τ^\pm	1777 ± 0.017

Table 1.3: *Charges and masses of the SM bosons*[1].

	charge	mass (GeV)	force
γ	0	0	electromagnetic
W^\pm	± 1	80.39 ± 0.025	weak
Z	0	91.18 ± 0.0021	weak
g	0	0	strong
Higgs	0	> 114.4	

Gluons bind quarks together and are responsible for the production of hadrons, which are divided in baryons (quark triplets) and mesons (quark-antiquark pair). Mesons are unstable and quickly decay via the strong force or weak force into lighter particles. For example, the π and the K mesons decay through the weak interaction and are relatively long lived with lifetimes of the order of 10^{-8} seconds. The J/Ψ meson decays via the strong interaction and has a lifetime of $\sim 10^{-21}$ seconds.

The only massless particles of the SM are the photon and the gluons. The masses of other SM particles are generated through the Higgs mechanism of electroweak symmetry breaking. This model assumes the existence of a scalar field, called the Higgs field. Dedicated searches for the Higgs by CERN LEP and Fermilab Tevatron have been conducted in recent years. While the Higgs particle remains elusive, these experiments have set limits on its mass. According to the most recent data [87] the mass of the Higgs is constrained to $114.4 \leq m_{Higgs} \leq 160$ GeV or $m_{Higgs} > 170$ GeV.

1.2 Physics beyond the Standard Model

There are strong reasons to believe that the SM is not a complete theory. Firstly, it describes the electromagnetic, strong and weak forces but not gravity. In natural units, the strength of the gravitational force is determined by the Planck mass. Max Planck introduced the Planck mass $M_{PL} = \sqrt{\hbar c/G_4} \sim 10^{19}$ GeV from three fundamental constants: Newton's gravitational constant G_4 , Planck's constant \hbar and the speed of light c . At energy scales of the order of the Planck scale, quantum gravitational effects become important. This suggests that the SM may be a low energy approximation of some theory which is valid at higher energies. The SM is also plagued by the hierarchy problem [88, 89]: the fundamental scale of gravity is $\sim 10^{16}$ times higher than the electroweak scale. Why is gravity so much weaker than the other forces?

The hierarchy problem can also be understood by considering corrections to the Higgs mass. The Higgs mass receives divergent corrections, e.g. from

production of a quark-antiquark pair. The observed Higgs mass m_{Higgs} is related to the bare Higgs mass m_{bare} by [90]

$$m_{Higgs}^2 \sim m_{bare}^2 - \Lambda^2, \quad (1.1)$$

where Λ is the cutoff introduced to regulate the divergence. Assuming that the SM is valid up to M_{PL} , a natural choice for the cutoff is of the order of the Planck scale. This would cause the Higgs mass to diverge, unless a fine tuning of the order of 1 out of 10^{16} is imposed to remove the quantum corrections in Eq. (1.1):

$$1 \sim \frac{m_{bare}^2}{\Lambda^2} - \frac{m_{Higgs}^2}{\Lambda^2}. \quad (1.2)$$

The SM also does not address unification of fundamental interactions. Gauge coupling constants determine the strength of an interaction, for example the fine structure constant α determines the strength of the electromagnetic force. Coupling constants are not strictly “constants” since they vary as the momentum transfer changes in a scattering process. If the SM is indeed embedded in some theory valid at higher energies, then at those higher energies all the three forces should have the same strength. The SM coupling constants, α_i , where i denotes electromagnetic ($i=1$), weak ($i=2$) and strong ($i=3$) forces, satisfy [91]

$$\frac{1}{\alpha_i(X^2)} = \frac{1}{\alpha_i(\mu^2)} + \frac{b_i}{4\pi} \ln \frac{X^2}{\mu^2}, \quad (1.3)$$

where, $\alpha_i(X^2)$ are the coupling constants at momentum transfer scale X , $\alpha_i(\mu^2)$ are the coupling constants at energy scale μ (for example the Z^0 mass scale ~ 92 GeV), and b_i are numerical factors which depends on the particle content of the SM: $b_1=7$, $b_2=-3$, $b_3=-7$ [13]. It is observed that the coupling constants do not meet at any scale when extrapolated to higher energies using Eq (1.3) (See left panel of Fig.1.1).

1.3 Supersymmetry

The most studied model of new physics beyond the SM is SUSY. In SUSY, each boson (fermion) has a fermionic (bosonic) superpartner. Quantum corrections to the Higgs mass due to boson and fermion loops have opposite signs. If the SM particles and their supersymmetric partners are degenerate in mass, their contributions to the Higgs mass cancel. Thus a Higgs boson with mass ~ 100 GeV is possible [92]¹. The presence of superpartners leads to a modification of the b_i constants of Eq. (1.3). Therefore, in SUSY the running gauge couplings

¹Note, however, that SUSY is a broken symmetry at low energy and therefore the degeneracy in the particle and sparticle masses is not exact.

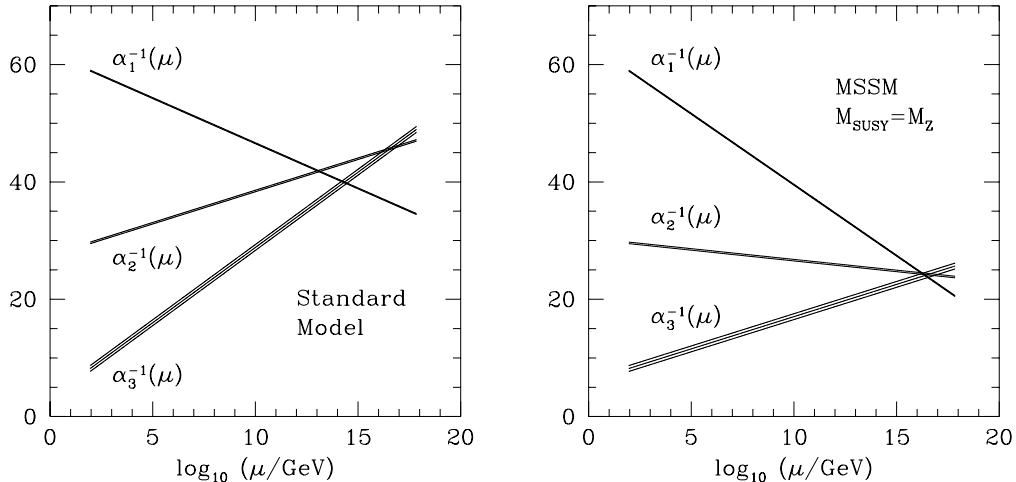


Figure 1.1: Gauge couplings as a function of the energy in SM (left panel) and SUSY (right panel). The relative width of each line reflects current experimental uncertainties. Reproduced from [13].

when extrapolated to high energies meet at the Grand Unified Theory (or *GUT*) scale 10^{16} GeV (see right panel of Fig. 1.1.).

In SUSY, superpartners have identical properties as their SM counterparts (masses, charges and quantum numbers), differing only in their spin. The supersymmetric partners of the gluons (spin 1) are gluinos (spin $\frac{1}{2}$), the superpartners of quarks (leptons) with spin $\frac{1}{2}$ are squarks (sleptons) with spin 0, the partner of the Higgs (spin 0) is the Higgsino (spin $\frac{1}{2}$) and the partners of the of W, Z and γ (spin 1) are gauginos with spin $\frac{1}{2}$. The gaugino is a common name for the supersymmetric partners of the gauge bosons. There are two charginos and four neutralinos that occur as a result of mixing between the Higgsinos and gauginos.

As we have mentioned, the Minimal Supersymmetric extension of the Standard Model (MSSM) [93, 94] allows for the unification of electromagnetic, weak and strong forces at $M_{GUT} \sim 10^{16}$ GeV. Since superpartners of SM particles are not observed at low energies, SUSY must be a broken symmetry. The SUSY breaking scale is generally assumed to be around 1 TeV. A method of SUSY breaking which is mediated by gravitational interactions is supergravity (SUGRA). The gravitino is the supersymmetric counterpart of the graviton. In its minimal version, the physics of mSUGRA is determined by a point in the five-dimensional moduli space with parameters:

- m_0 , the common mass of scalar particles (squarks and sleptons) at M_{GUT} ,
- $m_{1/2}$, the common gaugino and Higgsino mass at M_{GUT} ,
- A_0 the common trilinear coupling at M_{GUT} ,

- $\tan \beta$, the ratio of the vacuum expectation values of the two Higgs fields,
- μ , the sign of the Higgsino mass parameter.

In the MSSM, the Higgs has five states denoted by H_0, h_0, A_0, H^\pm . The masses of these states are related to the masses of the massive W^\pm and Z^0 bosons by the relations [95]

$$m_{H_0, h_0}^2 = \frac{1}{2} \left[m_{A_0}^2 + m_Z^2 \pm \sqrt{(m_{A_0}^2 + m_Z^2)^2 - 4m_{A_0}^2 m_Z^2 \cos^2 2\beta} \right], \quad (1.4)$$

$$m_{H^\pm} = m_W^2 + m_{A_0}^2. \quad (1.5)$$

Typical mSUGRA parameters which are relevant for LHC processes (LHC points) are given in Table 1.4 [96] and Fig. 1.2.

Table 1.4: *MSSM Parameters for typical LHC points. The first five points refer to ATLAS and LM1 refers to CMS (see Chapter 2). The scalar mass and the gaugino mass are given in GeV [6].*

LHC point	m_0	$m_{1/2}$	A_0	$\tan \beta$	μ
A	100	300	300	2.1	+
B	400	400	0	2	+
C	400	400	0	10	+
D	200	100	0	2	-
E	800	200	0	10	+
LM1	60	250	0	10	+

Neutralino $\tilde{\chi}_i^0$, gluino \tilde{g} and squark \tilde{q} masses are determined by m_0 and $m_{1/2}$ through the relations $\tilde{\chi}_1^0 \sim m_{1/2}/2$, $\tilde{\chi}_2^0 \sim \tilde{\chi}_1^\pm \sim m_{1/2}$, $\tilde{g} \sim 3m_{1/2}$ and $m(\tilde{q}) \sim (m_0^2 + 6m_{1/2}^2)^{1/2}$ [97]. The gluino and the first two generations of squarks masses do not depend on A_0 . The masses of the bosons depend on m_0 and the masses of the fermions depend on $m_{1/2}$ and A_0 [98].

A symmetry of the MSSM is R -parity [93, 94]. The R -parity of a particle is defined as:

$$P_R = (-1)^{3B+L+2s}, \quad (1.6)$$

where L (B) is the lepton (baryon) number and s is the particle spin. Superpartners have $P_R = -1$ and SM particles have $P_R = 1$. As a consequence, R -parity implies that SUSY particles are always pair produced in the decay of SM particles. R -parity conservation ensures that a SUSY process at the LHC ends in a state with SM particles and two lightest stable SUSY particles (LSPs), which are generally neutralinos. Being colorless and chargeless

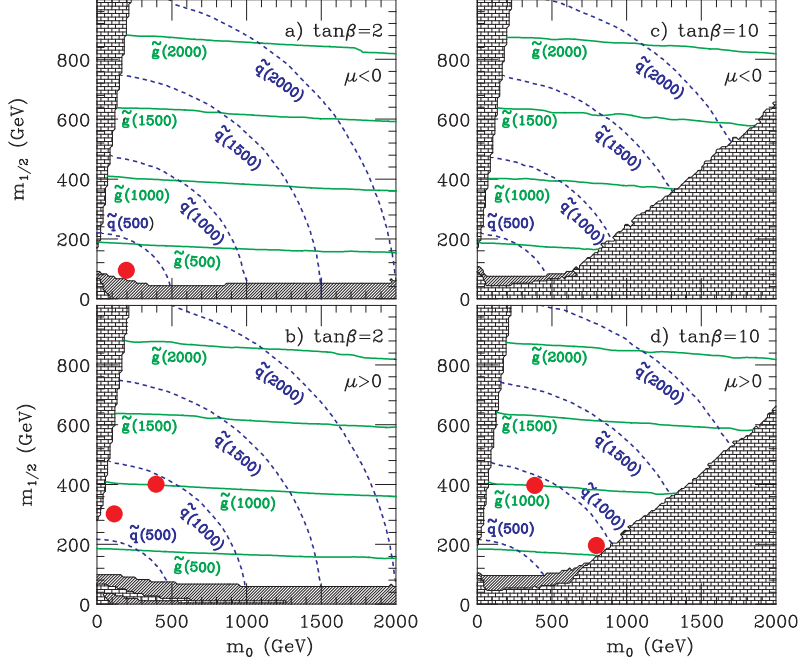


Figure 1.2: Five ATLAS points (large dots) shown in the $m_0 - m_{1/2}$ plane along with lines of constant squark and gluon mass. The shaded regions are excluded because of theoretical/experimental constraints. Reproduced from [14].

the LSPs escape the detector and are the source of missing transverse momentum \cancel{P}_T an important signature of SUSY events². Throughout this thesis we will assume that R -parity is conserved, in agreement with the mSUGRA scenario. The mass spectrum for the typical LHC points of Table 1.4 is given in Table 1.5.

Hadronic SUSY processes are dominated by $\tilde{g}\tilde{g}$, $\tilde{g}\tilde{q}$ and $\tilde{q}\tilde{q}$ channels. Table 1.6 shows the SUSY cross section for the LHC points of Table 1.4. Fig. 1.3 shows a typical SUSY decay chain. This example illustrates the three important characteristics of SUSY processes; production of jets, leptons and missing energy. The jets are produced at the beginning of the decay chain from the hadronization of quarks and gluons. The end phases of the decay are dominated by leptons produced by the decay of charginos and neutralinos. The missing energy is due to the LSPs.

1.4 Extra-dimensional Models

Alternatives to SUSY are extra-dimensional models such as LEDs [88, 99, 100], warped braneworlds [89, 101] and universal extra dimensions [102, 103]. In these scenarios, the fundamental scale of gravity M_* is lowered to ~ 1 TeV by

²If R -parity is not conserved, the missing transverse energy is reduced by the LSP decay.

	A	B	C	D	E	LM1
$q, \tilde{d}_L, \tilde{s}_L$	669	947	947	315	906	565
\tilde{u}_L, \tilde{c}_L	665	944	943	309	903	559
\tilde{d}_R, \tilde{s}_R	643	916	916	307	900	542
\tilde{u}_R, \tilde{c}_R	644	918	917	306	900	542
\tilde{b}_1	616	846	855	270	759	517
\tilde{t}_1	472	630	688	253	575	405
\tilde{b}_2	642	913	910	306	891	542
\tilde{t}_2	677	895	895	316	778	581
e_L^-, μ_L^-	230	483	484	214	810	187
e_R^-, μ_R^-	152	427	428	206	804	118
$\tilde{\nu}_{e_L}, \tilde{\nu}_{\mu_L}$	220	478	476	204	806	168
τ_1^-	154	427	423	205	795	111
$\tilde{\nu}_{\tau_L}$	218	477	474	204	803	165
τ_2^-	229	483	483	214	808	189
\tilde{g}	719	951	951	277	541	607
$\tilde{\chi}_1^0$	117	163	163	43	78	97
$\tilde{\chi}_2^0$	218	310	306	93	145	178
$\tilde{\chi}_1^\pm$	217	309	307	93	145	178
$\tilde{\chi}_2^\pm$	511	765	538	271	330	363
h_0	89	92	114	66	110	110
H_0	613	1021	703	376	856	377
A_0	604	1012	698	366	851	374
H^+	613	1021	707	376	860	385

Table 1.5: *SUSY mass spectrum in GeV. The first two generations of squarks and sleptons are degenerate. Masses are computed using ISAJET (ver. 7.75) [7].*

the presence of n extra spatial dimensions or by a warping of the metric.

The idea of extra spatial dimensions was first proposed by Kaluza and Klein in the 1920's in an attempt to unify gravity and electromagnetism. The recent interest in extra-dimensional models arises from the possibility that these models may provide a solution to the hierarchy problem.

The ArkaniHamed-Dimopoulos-Dvali (ADD) [88, 99, 100] and the Randall-Sundrum (RS) [89, 101] models assume the existence of 3-branes. A 3-brane is a surface with three spatial dimensions where matter fields are restricted. In the ADD model, the gravitons can propagate in the extra dimensions which are compactified at small scales (bulk).

The idea of EDs also find support from ST [104, 105, 106], the most complete proposal for a theory of quantum gravity as of now. According to ST all particles are different vibrational modes of a closed or open string living in 10

Table 1.6: Cross section in fb for production of SUSY particles for the LHC points listed in Table 1.4 [8, 9, 10, 11].

	A	B	C	D	E	LM1
$\tilde{g}\tilde{g}$	1751	258	259	437189	10877	10550
$\tilde{q}\tilde{q}$	2379	363	337	103059	455	8851
$\tilde{q}\tilde{q}$	2820	686	672	73769	909	6901
$\tilde{g}\tilde{q}$	8306	1486	1444	642765	8259	28560

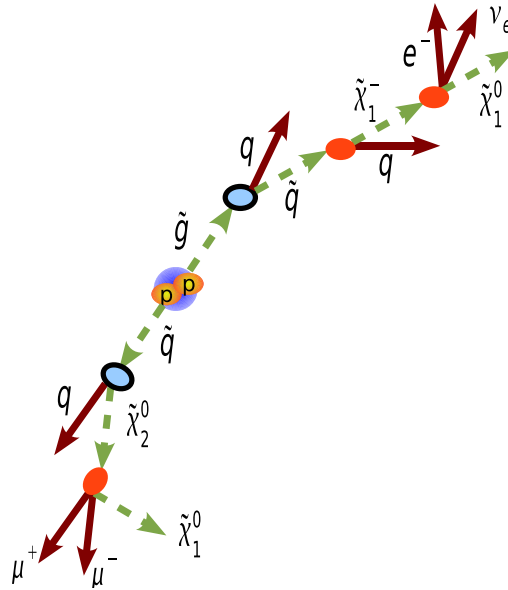


Figure 1.3: Typical SUSY cascade decay in a hadronic process (pp).

or 11 dimensions. Open strings have endpoints on the 3-brane, whereas closed strings describing force carriers or other multiplets are free to move into the bulk.

1.4.1 Kaluza-Klein Reduction

The effect of the presence of EDs can be illustrated with a simple example: the KK reduction on a circle of radius R [15, 107]. The Klein-Gordon equation

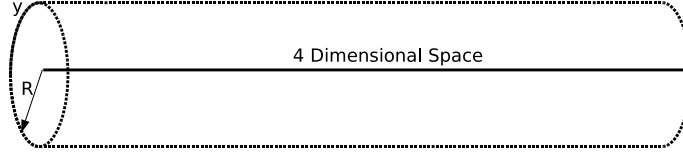


Figure 1.4: Compactified extra dimension of radius R (dotted line). The solid line denotes 4D spacetime. Adapted from [15].

for a scalar field ψ of mass m_ψ on a 5-dimensional spacetime with topology $M_4 \times S_1$, where M_4 is the four dimensional Minkowski space and S_1 is a circle (see Fig. 1.4), is

$$\left(\frac{\partial^2}{\partial t^2} - \nabla_5^2 + m_\psi^2 \right) \psi = 0, \quad (1.7)$$

where ∇_5^2 is the Laplacian in 5 dimensions:

$$\nabla_5^2 = \frac{\partial^2}{\partial x_1^2} + \frac{\partial^2}{\partial x_2^2} + \frac{\partial^2}{\partial x_3^2} + \frac{\partial^2}{\partial y^2}. \quad (1.8)$$

Here x_i ($i=1,2,3$) are the usual three spatial coordinates and y is the coordinate of S_1 . $\psi(x_i, y, t)$ is periodic under the transformation $y \rightarrow y + 2\pi R$. The solution of Eq. (1.7) is of the form

$$\psi = \sum_{l=-\infty}^{\infty} \psi_n(x_i, t) e^{ip_5 y}, \quad (1.9)$$

where $p_5 = l/R$ ($l=\pm 1, \pm 2 \dots$) is the momentum along the extra dimension. The exponential part of the solution follows from the periodicity condition on y . Substituting Eq. (1.9) into Eq. (1.7) it follows

$$\sum_{l=-\infty}^{\infty} \left(\frac{\partial^2}{\partial t^2} - \nabla_4^2 + m_\psi^2 + \frac{l^2}{R^2} \right) \psi = 0. \quad (1.10)$$

Therefore, the scalar field ψ in 4 dimensions is equivalent to an infinite number of KK states with masses

$$m^2 = m_\psi^2 + \frac{l^2}{R^2}. \quad (1.11)$$

The above equation shows that a particle in n dimensions can be described by a collection of 4-dimensional modes. The lightest field ψ_0 has mass m_ψ (this is the KK zero mode or ground state) and the excited modes are doubly degenerate $m(l) = m(-l)$. The mass of the KK excitation for $R^{-1} \ll m_\psi$ is, in natural units,

$$m \sim m_\psi + \frac{l}{R}. \quad (1.12)$$

Processes with energy $\sim R^{-1}$ should be able to probe excited KK modes. Thus, R^{-1} is the threshold energy for detecting EDs.

Models of EDs can be classified on the basis of KK excitations. In the universal extra dimension model, all particles experience KK excitations. In the flat compactification model (e.g. ADD), or in the warped compactification model (e.g. RS), there is a restriction on which particles possess KK excitations. The work in this thesis is concerned with the two latter models. These will be discussed in some detail in Sects. 1.4.2 and 1.4.3.

1.4.2 ADD

In the ADD model, all gauge fields except gravity are confined to a 3-dimensional brane. Their quanta do not show KK excitations because they do not feel the effect of the EDs; only gravitons are allowed to propagate in the bulk. According to the ADD model, gravity is a strong force in the higher-dimensional spacetime, but appears weak to a four-dimensional observer due to its “leakage” in the EDs (See Fig. 1.5). In this model, n EDs are compactified on a circle of

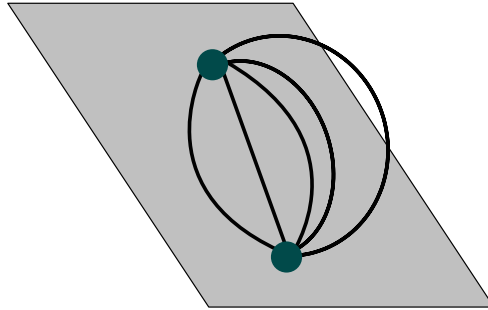


Figure 1.5: Gravitational lines of force between the two test masses leaks into the EDs. This leads to gravity being weaker on the brane. Adapted from [15].

radius R . The relation between the gravitational constants in 4 and $n + 4$ di-

mensions, G_4 and G_{n+4} , can be obtained by considering the $4 + n$ dimensional Gauss' Law [100]

$$\begin{aligned} & \text{(Net gravitational flux over a closed surface C)} \\ & = S_{(3+n)} G_{4+n} \times \text{Mass contained within C,} \end{aligned} \quad (1.13)$$

where $S_d = 2\pi^{d/2}/\Gamma(d/2)$ is the surface of an unit d -dimensional sphere. The force between two test masses m_1 and m_2 , separated by a distance r is

$$F_{4+n} = G_{4+n} \frac{m_1 m_2}{r^{n+2}} \text{ for } r \ll R. \quad (1.14)$$

For $r \gg R$, the test masses do not experience the effect of the EDs: the gravitational lines of force are constrained within the volume of the EDs. Therefore, the familiar $1/r^2$ force law is obtained:

$$F_4 = G_4 \frac{m_1 m_2}{R^n r^2}. \quad (1.15)$$

The relation between the four-dimensional and the higher dimensional Newton's constants, using Eqs. (1.14) and (1.15), is

$$G_{4+n} = R^{D-4} G_4 \equiv R^{D-4} M_{PL}^{-2}, \quad (1.16)$$

where $D = n + 4$ is the total number of spacetime dimensions. Since R in Eq. (1.16) has the dimensions of inverse mass, G_{4+n} has dimensions of $(\text{mass})^{2-D}$. The D dimensional Planck's constant M_\star is defined as

$$M_\star = G_D^{\frac{1}{2-D}}. \quad (1.17)$$

The first equality of Eq. (1.16) can also be obtained through dimensional analysis [106]. The four-dimensional gravitational potential $\Phi_{g(4)}$ satisfies

$$\nabla^2 \Phi_{g(4)} = 4\pi G_4 \rho_m, \quad (1.18)$$

where ρ_m is the mass density. In D dimensions, Eq. (1.18) can be rewritten as

$$\nabla^2 \phi_{g(n+4)} = 4\pi G_{n+4} \rho_m. \quad (1.19)$$

The left hand sides of Eq. (1.18) and Eq. (1.19) have identical dimensions. Therefore, it follows

$$G_{4+n} \frac{M}{R^{n+3}} = G_4 \frac{M}{R^3} \Rightarrow G_{4+n} = G_4 R^{D-4}. \quad (1.20)$$

Using the above equation and Eq. (1.16), the relation between the fundamental scales in 4 and $n + 4$ dimensions is

$$M_{PL}^2 \sim V_n M_\star^{n+2}. \quad (1.21)$$

If the volume of the EDs is large in M_\star^{-1} units, M_\star can be of the order of one TeV.

Setting $M_\star \sim 1$ TeV in Eq. (1.21) implies that the radius of the EDs is $R \sim 10^{32/n-19}$ meters. $n=1$ implies $R=10^{10}$ km, i.e. a large extra dimension with a size of the order of the solar system. The case $n = 2$ is ruled out from astrophysical considerations [108]. Gravity has not been tested to scales of $\sim 10^{-6}$ mm or $\sim 10^{11}$ TeV (for $n = 3$), and hence one might expect to see deviations from Newton’s laws at this scale³.

As outlined in Sect. 1.4.1, compactification of EDs causes the appearance of towers of KK modes. From Eq. (1.11), compactification of n extra spatial dimensions of radius R would result in

$$m_n(\mathbf{l}) = \frac{1}{R} \sqrt{l_1^2 + l_2^2 + \dots + l_n^2}, \quad (1.22)$$

where $m_n(\mathbf{l})$ denotes the mass of the $n - th$ KK mode \mathbf{l} . Depending on the number of EDs, the graviton modes could be very light. For example, the mass of the lowest graviton mode is ~ 25 MeV for 6 EDs. Experimental signatures of the ADD model would be production of KK excitations of gravitons and virtual gravitons. Since the mass splitting of the KK modes, $\Delta m = 1/R \sim 10^{-32/n}$ TeV is extremely small, a large number of KK modes would be produced in high energy collisions.

In the ADD model, gravitons are expected to decay producing jets and missing energy (\cancel{E}_T), i.e., a jet or photon recoiling against “nothing”. Detection of such events would establish the existence of EDs. Searches for graviton production have been conducted or are already underway: data from LEP and Tevatron have been analyzed to search processes like $e^+e^- \rightarrow \gamma + \cancel{E}_T$ and $e^+e^- \rightarrow Z + \cancel{E}_T$, $p\bar{p} \rightarrow jet + \cancel{E}_T$ and $p\bar{p} \rightarrow \gamma + \cancel{E}_T$ [1]. The combined LEP 95% CL lower bounds on the fundamental Planck mass and the upper bounds on the size of EDs are listed in Table 1.7 [110].

Table 1.7: *LEP lower bounds on M_\star and upper bounds on the size of the EDs as a function of the number of EDs for the ADD model.*

n	M_\star (TeV)	R (mm)
3	> 1.20	$< 2.6 \times 10^{-6}$
4	> 0.94	$< 1.1 \times 10^{-8}$
5	> 0.77	$< 4.1 \times 10^{-10}$
6	> 0.66	$< 4.6 \times 10^{-11}$

³Tests of the Gravitational Inverse-Square Law give bounds on the size of an extra dimension: currently it is $\leq 44 \mu m$ [109]

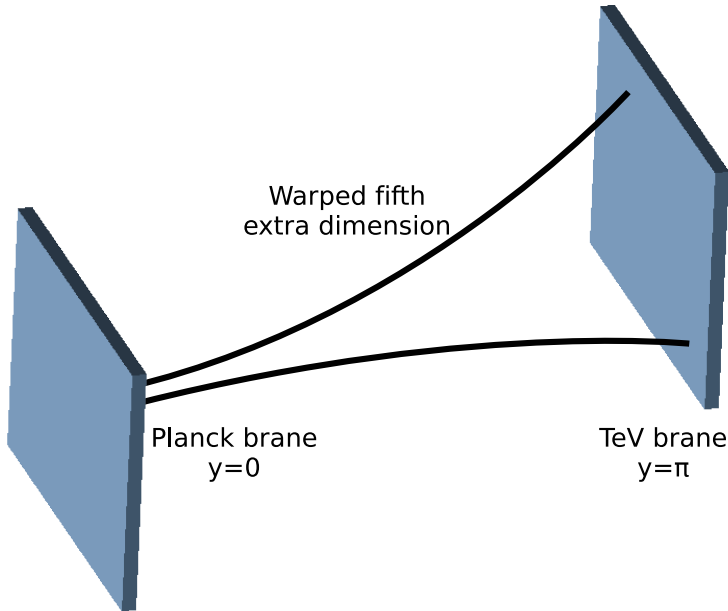


Figure 1.6: *RS model of EDs. The fifth extra dimension is warped leading to the weakness of gravity on our brane. SM fields are restricted to the TeV brane. The graviton can propagate in the extra dimension.*

1.4.3 RS

The simplest RS model assumes the existence of one extra dimension and two 3-branes. SM fields are restricted to one of the branes while gravitons are allowed to exist also in the bulk. In the RS scenario, the hierarchy problem is solved by assuming a single warped extra dimension. The perceived weakness of gravity is not due to the presence of a large flat extra-dimensional bulk as in the ADD model, but follows from the curvature of the extra dimension. RS compactification is on an orbifold which is obtained by applying a circular compactification on the extra dimension y , i.e. $y \rightarrow y + 2\pi r$, where r is the compactification radius of the extra dimension y , and identifying $y = -y$. The extra-dimensional coordinate takes values between 0 and πr . Thus, the resulting manifold can be seen as a line segment of length πr .

The branes in the RS model are located at the orbifold fixed points $y = 0$ (Planck brane) and $y = \pi r$ (TeV brane). SM particles are localized on the TeV brane and gravity can propagate in the bulk. The Planck scale is related to the fundamental scale of gravity in 5 dimensions by

$$M_{PL}^2 = 8\pi \frac{M_*^3}{k} (1 - e^{-2\pi k r}), \quad (1.23)$$

where k is of the order of the Planck scale. The hierarchy between the fundamental scales is removed by the presence of the warp factor $e^{-2\pi k r}$. If kr is

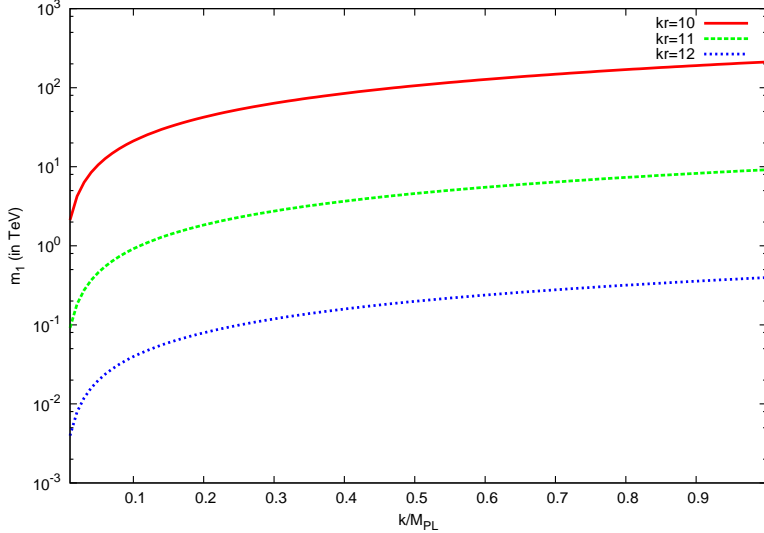


Figure 1.7: Mass of the first graviton excitation m_1 versus c for $kr=10$ (solid red line), 11 (dashed green line) and 12 (dotted blue line).

in the range 10-12, TeV scale masses can be generated from the fundamental Planck scale $\sim 10^{16}$ TeV. A field on the TeV brane with a mass kx_n has a physical mass m_n of

$$m_n = kx_n e^{-kr\pi}, \quad (1.24)$$

where x_n are the roots of the Bessel function of first order $J_1(x_n)$. The mass of the lowest graviton mode in the RS scenario is $O(\text{TeV})$. The strength of the graviton-matter coupling is determined by the scale $\Lambda = (1/\sqrt{8\pi})M_{PL}e^{-k\pi r}$. In the following sections the ratio $c = k/M_{PL}$ is chosen to be approximately 10^{-2} [111]. This leads to a graviton mass of the order of ~ 1 TeV, which could be probed at the LHC (see Fig 1.7). The mass splitting between the first and second excited states of the graviton is $\Delta m = m_2 - m_1 \sim O(1)$ TeV.

Real gravitons in hadronic collisions would be produced via $q\bar{q} \rightarrow gG, qg \rightarrow qG$ and $gg \rightarrow gG$. The experimental signatures would be multijet or jets+photons along with missing E_T . Relevant processes for virtual gravitons are $f\bar{f} \rightarrow G^*$ and $gg \rightarrow G^*$. Gravitons in the RS scenario behave differently from ADD gravitons. Being heavy, they quickly decay into SM particles as in $G^* \rightarrow f\bar{f}, gg, \gamma\gamma, Z^0 Z^0$ and $W^+ W^-$.

1.5 Black hole production

In scenarios with LEDs, pp collisions at the LHC could produce TeV-mass BHs⁴. A non-rotating BH is described by the Schwarzschild solution in $(n+4)$

⁴In this thesis we consider only BHs. For reviews on string balls and branes see [39, 112, 113, 114, 115] and references therein.

dimensions:

$$ds^2 = -R(r)dt^2 + R(r)^{-1}dr^2 + r^2d\Omega_{n+2}^2, \quad (1.25)$$

where

$$R(r) = 1 - \left(\frac{R_{BH}}{r}\right)^{n+1}. \quad (1.26)$$

The radius of the BH as a function of the BH mass M is

$$R_{BH}(M) = \frac{1}{\sqrt{\pi} M_\star} \left\{ \left[\frac{8\Gamma(\frac{n+3}{2})}{(2+n)} \right] \frac{M}{M_\star} \right\}^{\frac{1}{n+1}}. \quad (1.27)$$

Thus, a fundamental scale-mass BH has a radius of the order of M_\star^{-1} in natural units. BH radii for different values of n are shown in Table 1.8 for $M=4$ TeV and $M_\star=1$ TeV.

Table 1.8: *BH radius as a function of n for a BH mass of $M=4$ TeV.*

n	1	2	3	4	5	6
$R_{BH} \times 10^{-4}$ fm	3.64	2.45	2.10	1.98	1.93	1.93

BH production in particle collisions would occur as follows. According to Thorne's hoop conjecture [116], a BH of mass M is formed when an object is compacted in all directions such that

$$C < 2\pi R_{BH}(M), \quad (1.28)$$

where C is the circumference of the region where the object is compacted into and R_{BH} is the Schwarzschild radius for a BH of mass M . Assuming no gravitational radiation emission the black disk (BD) cross section for head on collision is

$$\hat{\sigma}(\hat{s}; n) = \pi R_{BH}^2, \quad (1.29)$$

where $\sqrt{\hat{s}}$ is the CM energy of the colliding partons. A more realistic model assumes some CM energy being lost as gravitational radiation (see Ref. [117] for a more detailed discussion) and non-zero impact parameter. Conservation of angular momentum implies that BHs formed with a non-zero impact parameter are spinning. They are described by the Kerr solution. A spinning BH has a smaller radius than a non-rotating BH of equal mass

$$R_{BH}(M, J) = \frac{1}{\sqrt{\pi} M_\star} \left\{ \left[\frac{8\Gamma(\frac{n+3}{2})}{(2+n)} \right] \frac{M}{M_\star} \right\}^{\frac{1}{n+1}} \left[1 + \frac{(n+2)^2 J^2}{4R_{BH}^2 M} \right]^{\frac{-1}{n+1}}, \quad (1.30)$$

where J is the angular momentum of the BH. To estimate the gravitational energy loss, the colliding particles are described as two Aichelburg-Sexl shock waves (see Fig. 1.8) [118]; the overlap of the shock waves (region *IV*) forms a

trapped-surface (TS) which sets a lower limit to the mass of the BH [119, 120]⁵. Depending on the model, BH masses range from 60% (TS model) to 100% (BD model) of the total center-of-mass energy.

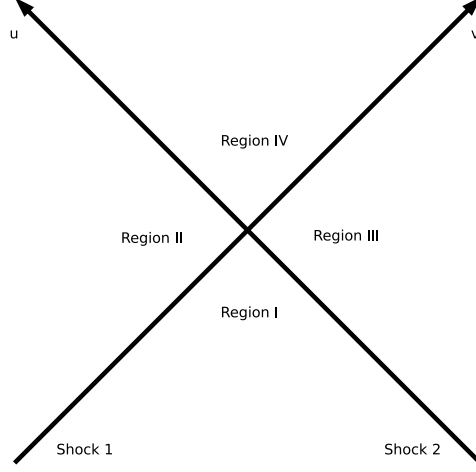


Figure 1.8: The u and v lines represent two shock waves moving in opposite directions, colliding at $u=v=0$. Region I is before the collision. Regions I, II and III are linear. Region IV is highly non-linear and curved, a closed trapped surface is formed. The BH is formed in this region.

The cross section at the parton level for the Schwarzschild BH formation process is obtained from Eq. (1.29) as

$$\hat{\sigma}_{ij \rightarrow BH}(\hat{s}, n) = \frac{1}{M_\star^2} \left[\frac{8\Gamma(\frac{n+3}{2})}{(2+n)} \right]^{\frac{2}{n+1}} \left\{ \frac{\hat{s}}{M_\star^2} \right\}^{\frac{1}{n+1}}, \quad (1.31)$$

where i, j are the incident partons with CM energy \hat{s} . The parton cross section is independent of the type of incoming partons and depends only on M, M_\star and n . If the energy loss due to graviton emission is neglected, the total cross section is obtained by summing the contributions from all possible parton pairs:

$$\begin{aligned} \sigma_{pp \rightarrow BH}(s, n) \\ = \sum_{ij} \int_{\frac{\hat{s}}{s}}^1 dx' \int_x^1 \frac{dx''}{x''} f_i(x', Q) f_j(x/x'', Q) \sigma_{ij \rightarrow BH}(\hat{s}; n), \end{aligned} \quad (1.32)$$

where s is the squared CM energy of the pp collision, Q is four-momentum transfer, $f_i(x', Q)$ are the parton distribution functions (PDFs), x' are the parton momentum fractions and $x=x'x'' = \frac{\hat{s}}{s}$.

H. Yoshino & Y. Nambu and H. Yoshino & V. S. Rychkov [119, 120] have shown that the energy loss due to gravitational radiation is significant for large

⁵For an alternative estimate of the collisional gravitational loss, see Ref. [121].

impact parameters and large number of EDs. This reduces the BH mass from $M = \sqrt{\hat{s}}$ to $M = y(z)\sqrt{\hat{s}}$, where $z = b/b_{max}$, b_{max} is the maximum impact parameter and $y(z)$ ranges between $0 \dots 1$ [122]. This condition puts a lower cutoff on the parton momentum fractions. The lower bound on the parton momentum fraction is obtained by the condition $x_{min} = M_{min}^2/[s y^2]$ where M_{min} is the minimum mass for BH formation [122]. The inelastic BH cross section is

$$\begin{aligned} \sigma_{pp \rightarrow BH}(s, n) &= \sum_{ij} \int_0^1 2z dz \int_{x_{min}}^1 dx \int_x^1 \frac{dx'}{x'} f_i(x', Q) f_j(x/x', Q) \sigma_{ij \rightarrow BH}. \end{aligned} \quad (1.33)$$

The total BH cross section (1.33) is shown in Fig. 1.9. The cross section increases with energy. For 6 extra spatial dimensions and fundamental scale $M_\star = 1$ TeV, $\sigma_{pp \rightarrow BH} \sim 6$ pb at 14 TeV. This would turn the LHC into a BH factory with $\sim 2 \times 10^5$ BHs per year at a luminosity of $10^{33} \text{ cm}^{-2} \text{ s}^{-1}$!⁶ The BH cross section decreases with the increase in the number of spacetime dimensions and for increasing M_\star .

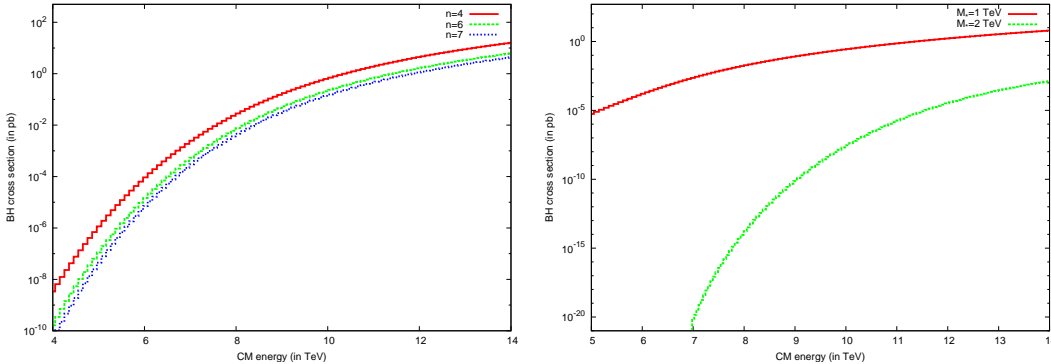


Figure 1.9: *Left Panel: BH cross section for different numbers of extra spatial dimensions as a function of the CM energy. The fundamental scale M_\star is assumed to be 1 TeV. Right Panel: BH cross section for $M_\star=1$ TeV (dashed) and $M_\star=2$ TeV (dotted).*

The distribution of BH masses is shown in Fig. 1.10 for different values of M_\star and n . Higher values of M_\star lead to more massive BHs.

TeV BHs decay immediately after formation. The decay starts via loss of excess multipole moments (balding phase). In this phase, the BH also loses mass by emitting gravitational radiation. In the spindown phase the BH loses

⁶Lepton colliders are expected to produce an even higher number of BHs than hadron colliders at equal CM energy because the collision energy is not distributed among the hadron constituents.

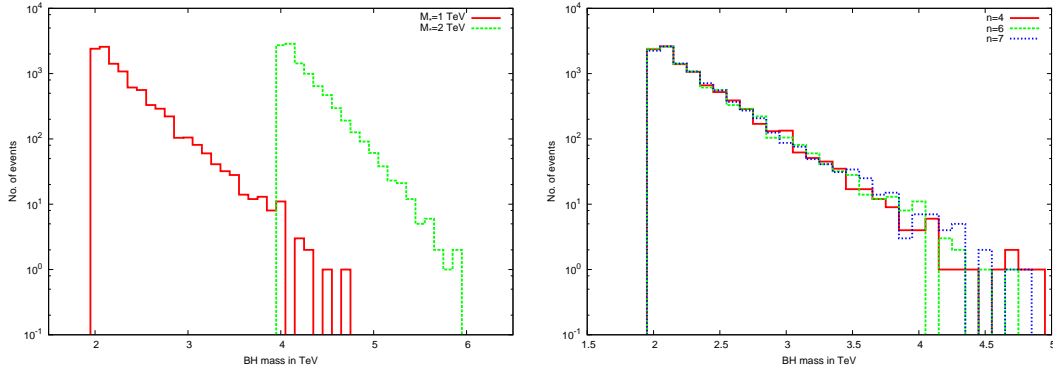


Figure 1.10: *Left Panel: BH mass for different values of M_* . Right Panel: BH mass for different values of extra spatial dimensions, n . Both plots are for 10000 events.*

angular momentum. This is followed by the evaporation phase where the BH loses the bulk of its mass by emitting Hawking radiation [123].

The Hawking temperature of a $(n + 4)$ dimensional BH is

$$T_H = \frac{n + 1}{4\pi R_{BH}}, \quad (1.34)$$

and its lifetime is approximately

$$\tau \sim \frac{1}{M_*} \left(\frac{M}{M_*} \right)^{\frac{n+3}{n+1}}. \quad (1.35)$$

The BH temperature and lifetime for a BH with mass $M=4$ TeV and $M_*=1$

Table 1.9: *BH temperature and lifetime as a function of n for a BH with mass $M=4M_*=4$ TeV.*

n	1	2	3	4	5	6
T_H (GeV)	86	192	298	397	487	570
τ ($\times 10^{-26}$ s)	1.05	0.66	0.53	0.46	0.42	0.39

TeV are shown in Table 1.9. Higher-dimensional BHs are hotter and have shorter lifetimes than their four-dimensional counterparts.

The Hawking process ends when the BH reaches a mass comparable to the fundamental scale. At this stage a final n -body decay or remnant production (Planck phase) may occur. SM particles produced during the BH decay phase are emitted on the brane and can be experimentally detected [124, 125] (see Fig. 1.11). As SM particles have overall more degree of freedoms (dofs) than bulk particles, brane emission is greater than bulk emission. This result becomes less and less significant in higher dimensions. For example, the power

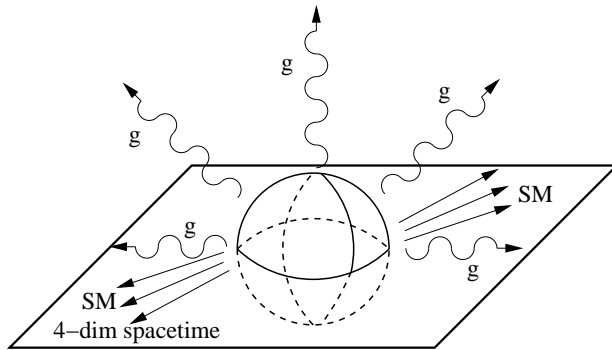


Figure 1.11: *Illustration of the Schwarzschild evaporation of a BH, showing brane and bulk emission [16]. SM particles are emitted on the brane. The graviton escapes both in the brane and bulk.*

loss due to gravitons is negligible in four dimensions whereas it is $\sim 25\%$ in 11 dimensions [126, 127].

1.6 String Resonances

ST is the leading candidate for the unification of the fundamental forces. The string scale M_s is defined as [106]

$$l_s = \sqrt{\alpha'} = \frac{1}{M_s}, \quad (1.36)$$

where α' is the slope parameter with units of inverse energy squared. The slope parameter is related to the four dimensional Newton's constant G_4 [15] by

$$\alpha' = \frac{G_4}{g_s^2}. \quad (1.37)$$

The strength of string interactions is controlled by the string coupling g_s . Combining Eq. (1.36) and Eq. (1.37), one obtains

$$M_s = g_s M_{\star}. \quad (1.38)$$

Since string effects are expected to appear just before quantum gravity effects set in, the string coupling is generally assumed to be of order one. A small coupling also justifies the use of perturbative analysis [13]. We have seen that in theories with EDs the fundamental quantum gravity scale may be as low as a TeV. Thus string effects might appear at the TeV scale. If this is the case, SRs would be observed at the LHC before the onset of non-perturbative quantum gravity effects such as BH production. String excitation modifications to SM amplitudes may even exceed amplitude modifications due to KK gravitons.

Detection of string events through corrections to SM amplitudes [128, 129, 130] at the LHC would be the most direct evidence of ST and EDs.

In Chapter 4 we will investigate the $pp \rightarrow$ string resonance $\rightarrow \gamma + \text{jet}$ process [129]⁷. The relevant process for $pp \rightarrow \gamma + \text{jet}$ events is gluon-gluon scattering: $gg \rightarrow g\gamma$. The string amplitude for this process is [129]

$$|M(gg \rightarrow g\gamma)|^2 = g_s^4 Q^2 C(N) \left\{ \left[\frac{s\mu(s, t, u)}{u} + \frac{s\mu(s, u, t)}{t} \right]^2 \right\} + g_s^4 Q^2 C(N) \{ (s \leftrightarrow t) + (s \leftrightarrow u) \}, \quad (1.39)$$

where s , t and u are the Mandelstam variables and

$$\mu(s, t, u) = \Gamma(1 - u) \left(\frac{\Gamma(1 - s)}{\Gamma(1 + t)} - \frac{\Gamma(1 - t)}{\Gamma(1 + s)} \right). \quad (1.40)$$

Here $N=3$ is the number of D -branes needed to generate the eight gluons of the SM, $C(N) = \frac{2(N^2-4)}{N(N^2-1)}$ is a constant parameter, and $Q^2 = \frac{1}{6}\kappa^2 \cos^2 \theta_W \sim 2.55 \times 10^{-3}$, where $\kappa^2=0.02$ and θ_W are the mixing parameter and the Weinberg angle, respectively. The values of these parameters are chosen as in Ref. [129].

In the limit $s \rightarrow nM_s^2$, the string amplitude possesses poles at $n=s/M_s^2$, where n is an integer. The amplitude has the form of Veneziano amplitudes [104, 105, 131], a feature common to all string models. The limiting value of the amplitude at the $n = \text{odd}$ poles is

$$|M(gg \rightarrow g\gamma)|^2 = g_s^4 Q^2 C(N) \frac{4}{(n!)^2} \frac{s^4 + u^4 + t^4}{M_s^4 [s - nM_s^2]} \left\{ \frac{\Gamma(t/M_s^2 + n)}{\Gamma(t/M_s^2 + 1)} \right\}^2. \quad (1.41)$$

The behavior of the amplitude at the even poles is obtained from Eq. (1.41) with the substitutions $s \rightarrow t$ and $n \rightarrow m = t/M_s^2$ in the square bracket term. The singularities of the amplitude are smeared with a fixed width $\Gamma = 0.1$ for all $n > 1$ and as

$$|M(gg \rightarrow g\gamma)|^2 \sim \frac{4g_s^4 Q^2 C(N)}{M_s^4} \left\{ \frac{M_s^8}{(s - M_s^2)^2 + (\Gamma^{J=0} M_s)^2} \right\} + \frac{4g_s^4 Q^2 C(N)}{M_s^4} \left\{ \frac{t^4 + u^4}{(s - M_s^2)^2 + (\Gamma^{J=2} M_s)^2} \right\}, \quad (1.42)$$

for $n=1$ [129]. Equation (1.42) includes a correction for spin dependent widths: $\Gamma^{J=0} = 0.75\alpha_s M_s$ and $\Gamma^{J=2} = 0.45\alpha_s M_s$, where $\alpha_s = g_s^2/4\pi$ is the strong coupling constant. The presence of the poles indicates the formation of SR. The total cross section for the $pp \rightarrow \gamma + \text{jet}$ event is obtained by integrating

⁷For a discussion of SR in the dileptonic and diphotonic channels see for e.g. [128, 131, 132, 133, 134].

the parton cross section over the parton distribution functions of the protons [135]

$$\sigma_{pp \rightarrow \text{string} \rightarrow \gamma + \text{jet}} = \int_{\frac{\hat{s}}{s}}^1 dx \int_x^1 dx' \int dt f_1(x', Q) f_2(x/x', Q) \frac{d\sigma}{dt}, \quad (1.43)$$

where

$$\frac{d\sigma}{dt} = \frac{|M(gg \rightarrow g\gamma)|^2}{16\pi s^2}. \quad (1.44)$$

The limits on t are fixed by the conditions $s + u + t = 0$ and $|t||u|/s \geq P_{Tmin}^2$ where P_{Tmin} is the minimum transverse momenta of the two outgoing particles of the 2×2 scattering. Figure 1.12 shows the differential cross section of the

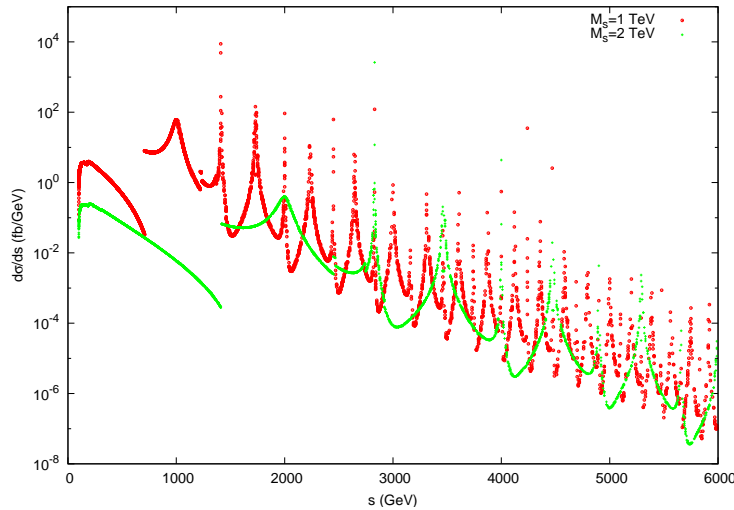


Figure 1.12: Differential cross section of string events for $M_s = 1$ TeV (red dots) and $M_s = 2$ TeV (green crosses) with $P_{Tmin} = 50$ GeV. SRs are clearly seen when $\hat{s} = nM_s^2$.

$pp \rightarrow \gamma + \text{jet}$ process

$$\frac{d\sigma}{ds} = \int \int dx' dt \frac{2\sqrt{s}}{x' E_{CM}^2} f_1(x/x', Q) f_2(x', Q) \frac{d\sigma}{dt}, \quad (1.45)$$

where we have used the CTEQ6D PDFs. The left panel of Fig. 1.13 shows the total cross section as a function of P_{Tmin} . The string cross section for $M_s = 1$ TeV (solid red line) and the cross section for $M_s = 2$ TeV (dashed green line) are $\sim 5 \times 10^4$ and 10^3 times less than SM, respectively.

The string cross-sections for $P_{Tmin} = 50$ GeV (solid red line) and 300 GeV (dashed green line) are shown in the right panel of Fig. 1.13, respectively. For $P_{Tmin} = 300$ GeV, the string cross section is ~ 100 times less than $P_{Tmin} = 50$ GeV when $M_* = 7$ TeV. The choice $P_{Tmin} = 50$ GeV leads to a signal-to-background ratio of ~ 73 . The string cross section is highly suppressed

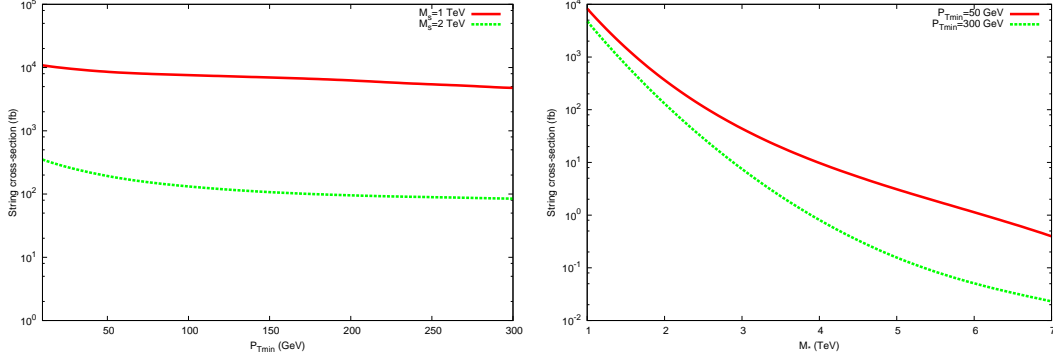


Figure 1.13: *Left panel: String cross section for $M_s = 1$ TeV (red dots) and $M_s = 2$ TeV (green crosses). The cross section for $M_s = 1$ TeV is ~ 44 times larger than the cross section for $M_s = 2$ TeV. Right panel: String cross section for the two extreme values of P_{Tmin} , 50 GeV (solid red line) and 300 GeV (dashed green line) as a function of M_* .*

w.r.t. the SM cross section for lower values of P_{Tmin} ; for example $\frac{\sigma_{string}}{\sigma_{SM}} \sim 10^{-5}$ for $P_{Tmin} = 10$ GeV. Thus, the discrimination of string events from the SM background is more difficult for events with lower P_{Tmin} . Both the SM background and the signal are substantially reduced for higher values of P_{Tmin} . For example, at 300 GeV they are reduced by a factor of $\sim 98\%$ and $\sim 42\%$ *w.r.t.* values at $P_{Tmin} = 50$ GeV, respectively. The optimal signal-to-background ratio is obtained for $P_{Tmin} \lesssim 100$ GeV.

Physics of Particle Collisions

In this chapter we briefly discuss the main features of CERN's LHC and introduce kinematical and dynamical quantities which will be used in our analysis.

2.1 The Large Hadron Collider

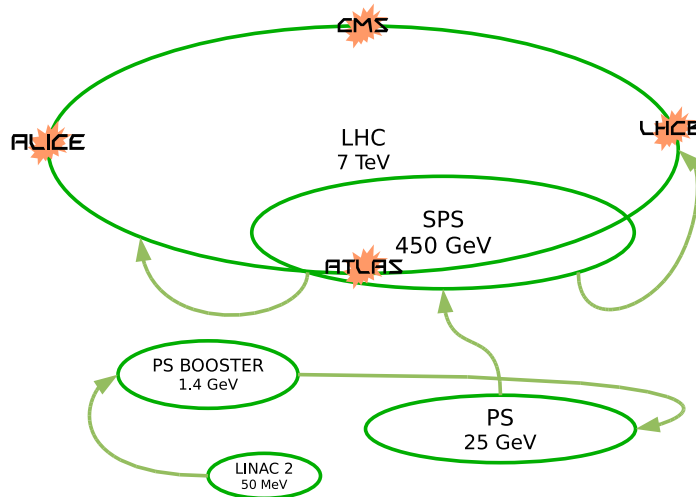


Figure 2.1: Illustration of the LHC ring structure showing four of the six experiments. The energy of the protons is increased in succession by the use of various smaller accelerators. Protons, first injected into LINAC, are emitted with an energy of 50 GeV. Next, the PS booster accelerates the protons to 1.4 GeV before it enters the Proton Synchrotron (PS). 25 GeV protons from PS is fed to the SPS (Super Proton Synchrotron), accelerating them more than 10 times their present energy to 450 GeV. In the final phase, the protons enter the LHC where they reach their final energy of 7 TeV per beam. Adapted from [17].

The LHC is a circular proton-proton collider with a circumference of 27

km. The LHC is host to various experiments: A Large Ion Collider Experiment (ALICE), A Toroidal LHC ApparatuS (ATLAS) [136], Compact Muon Solenoid (CMS) [137], the Large Hadron Collider beauty (LHCb) experiment, the Large Hadron Collider forward (LHCf) experiment and the TOTal Elastic and diffractive cross section Measurement (TOTEM) experiment. The ATLAS and CMS (see Fig. 2.2) are general-purpose high-luminosity detectors designed to cover a wide range of physics from the search for the Higgs [8, 9, 10, 30, 138, 139, 140, 141] and SUSY [14, 93, 94, 142, 143] to EDs [88, 89, 99, 100, 101, 102, 103]. The main feature of the ATLAS detector is its magnet system consisting of superconducting magnet coils. The CMS is built with the same goals as ATLAS but it offers an excellent muon tracking system. The LHC is based on the barrel plus endcaps design; a cylindrical detector covers the central region and two flat circular endcaps cover the angles close to the beam: ALICE and LHCb detectors are exceptions as they have asymmetric shapes. ATLAS and CMS detectors are entrusted with the task of studying events with large transverse momentum P_T , a signature common to SUSY, EDs and string-mediated interactions.

The primary purpose of the LHC detectors is to measure particle positions, charges, velocities, masses and energies. To achieve this goal, the detectors are composed of various sub-detectors. The calorimeter is the most important component as it measures the energy of the particles. It encloses the tracking system that electronically records the path of charged particles as they pass through matter. Calorimeters work on the following principle: they measure the ionization energy deposited in the shower when a particle interacts with a dense medium (e.g. lead). The electromagnetic calorimeter (ECAL) absorbs electrons and photons, the hadronic calorimeter (HCAL) records the energy of hadrons (e.g. pions and jets). Photons and neutrons are detected only by the calorimeter. Muons are identified by the long tracks in the calorimeter and the bulk of their energy is deposited in the muon chamber outside the calorimeter (See Fig. 2.3). At the LHC, the total P_T of the colliding particles is assumed to be zero. Neutrinos are weakly interacting particles and cannot be directly detected, but their presence can be inferred due to missing energy.

The LHC follows a right-handed coordinate system where the beam direction is along the z -axis and the vertical axis is y . The coordinates can also be expressed in terms of (r, η, ϕ) , where $\phi = \tan^{-1}(y/x)$ and the pseudorapidity is $\eta = -\ln[\tan(\theta/2)]$. The true rapidity of a particle defined as $\text{atanh}(p_z/E)$, where p_z is the momentum along the z direction and E is the energy of the particle. The rapidity for massless particles is the same as their pseudorapidity.

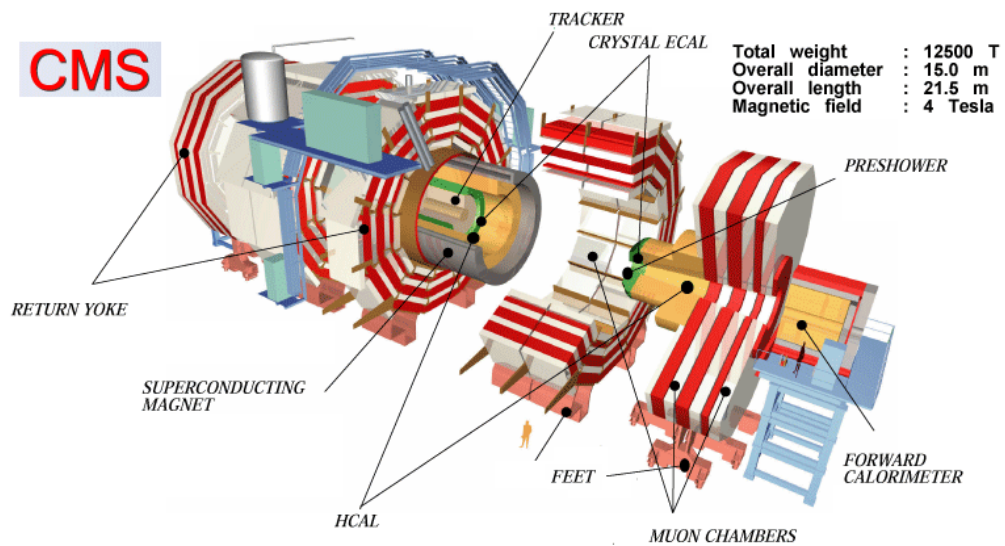
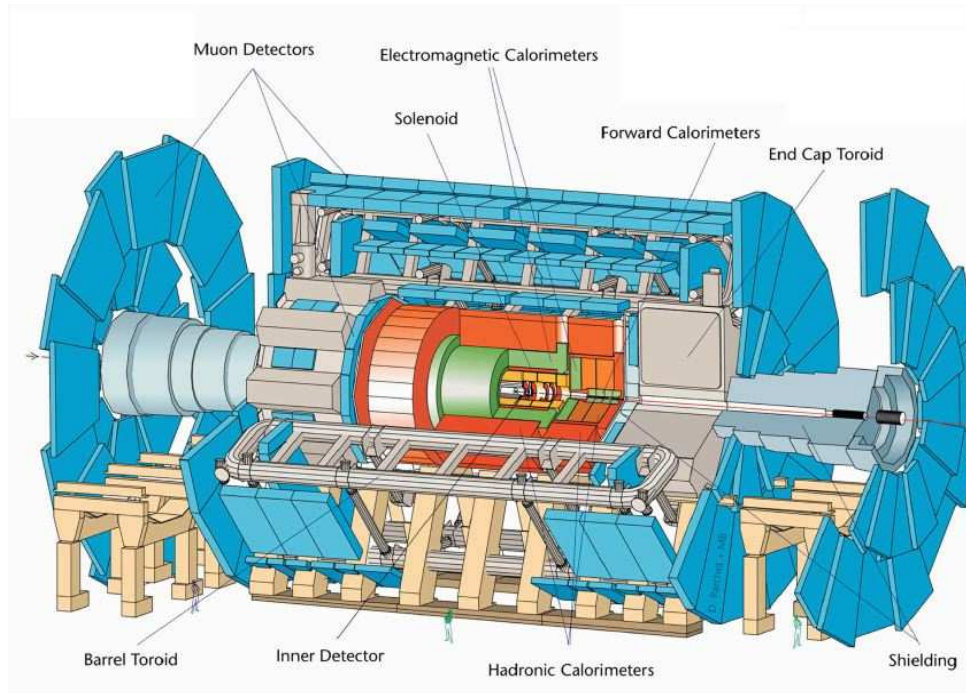


Figure 2.2: Cross section of the ATLAS and CMS [18] detectors at CERN.

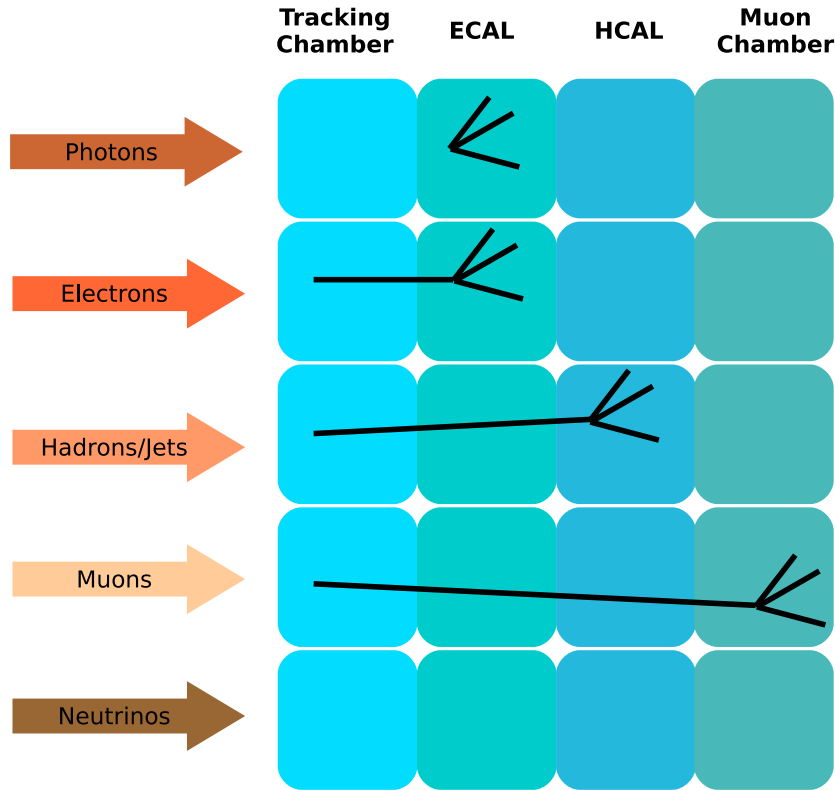


Figure 2.3: *Passage of charged particles through matter in particle colliders. Charged particles leave a track in the tracking chamber, neutral particles shower without leaving a track. Neutrinos are undetected. Adapted from [17].*

2.2 Luminosity

The performance of the LHC is described by its instantaneous luminosity L , which is a function of the number of particles in each bunch (n_b), the bunch crossing frequency f and the bunch area overlap A [1]:

$$L = f \frac{n_{b1} n_{b2}}{A}. \quad (2.1)$$

The proton beam at the LHC consists of ~ 3000 bunches, each containing about 10^{11} protons. Particle bunches are squeezed at the interaction points to increase the chances of collision to a cross-sectional area of about 10 sq. mm [17]. The luminosity can be enhanced by increasing the number of particles in each bunch and by increasing the frequency of collision. The latter can be achieved by properly focusing the beam at the interaction points.

The instantaneous luminosity has units of $cm^{-2}s^{-1}$. The number of events

N for a given process in the time Δt is

$$N = \sigma \int_0^{\Delta t} L(z) dz, \quad (2.2)$$

where σ is the total cross section. The integral in Eq. (2.2) is known as the integrated luminosity. The design luminosity of the LHC is $10^{34} \text{cm}^{-2} \text{s}^{-1}$, to be achieved within three years of running. The LHC initial or startup luminosity is $10^{29} \text{cm}^{-2} \text{s}^{-1}$.

2.3 Event Shape variables

Event shape variables are commonly used in particle physics to describe the spatial distribution of the outgoing particles. They include sphericity, 2nd Fox-Wolfram moment and thrust [144, 145].

- Sphericity:

$$S = \frac{3}{2}(\lambda_2 + \lambda_3), \quad (2.3)$$

where λ_2 and λ_3 are the two eigenvalues of the sphericity tensor $S^{\alpha\beta}$

$$S^{\alpha\beta} = \frac{\sum_i \mathbf{p}_i^\alpha \cdot \mathbf{p}_i^\beta}{\sum_i |\mathbf{p}_i|^2}. \quad (2.4)$$

Here $\alpha, \beta = 1, 2, 3$ and \mathbf{p}_i 's are the final state momenta of particles. An isotropic event is characterized by values of $S \sim 1$ whereas $S \sim 0$ for “jetty” events.

- 2nd Fox-Wolfram moment:

$$H_2 = \sum_{ij} \frac{|\mathbf{p}_i| |\mathbf{p}_j|}{E_{vis}^2} P_2(\cos \theta_{ij}), \quad (2.5)$$

where $\cos \theta_{ij}$ is the angle between hadrons i and j , E_{vis} is the total visible energy of the event and $P_2(x)$ is the Legendre polynomial of order 2. Values of H_2 closer to zero indicate spherical events whereas $H_2 \sim 1$ indicates that the event is dominated by jets.

- Thrust:

$$T = \max_{|n|=1} \frac{\sum_i |\mathbf{n} \cdot \mathbf{p}_i|}{\sum_i |p_i|}, \quad (2.6)$$

where n is the unit vector along the thrust axis. The thrust axis is defined as the axis which maximizes projected momenta. Isotropic events have $T \sim \frac{1}{2}$ and dijets have $T \sim 1$.

2.4 Invariant Mass and Jet Masses

Another two useful quantities in high energy physics are the invariant mass of outgoing particles and jet mass. They are defined as

- Invariant Mass:

For a system of m particles, the invariant mass is defined as

$$M_m \equiv \left(\sum_m E_m \right)^2 - \left(\sum_m \mathbf{p}_m \right)^2. \quad (2.7)$$

where $E(\mathbf{p})$ is the energy (momenta) of each particle. In a 2×2 collision the invariant mass of the outgoing particles is

$$M_{12} = (E_1 + E_2)^2 - (\mathbf{p}_1 + \mathbf{p}_2)^2, \quad (2.8)$$

$$= M_1^2 + M_2^2 + 2(E_1 E_2 - \mathbf{p}_1 \cdot \mathbf{p}_2). \quad (2.9)$$

in natural units. Neglecting the masses of the outgoing particles, as is often the case in high energy collisions, the invariant mass of the system is

$$M_{12} = \sqrt{(E_1 + E_2)^2 - (\mathbf{p}_1 + \mathbf{p}_2)^2} = \sqrt{2p_1 p_2 (1 - \cos \theta)}, \quad (2.10)$$

where θ is the angle between the two outgoing particles. The invariant mass is an important quantity in high energy physics because it predicts the mass of the particle formed in resonance.

- Jet Masses:

The particles of an event are randomly assigned into two groups and their squared invariant mass, M_1 and M_2 , is calculated. The heavy and light jet masses are defined as the larger and smaller of M_1 and M_2 that minimize $M_1^2 + M_2^2$, respectively.

Simulation Techniques

This chapter briefly introduces the simulation programs which will be used for our analysis: ISAJET (ver. 7.75) [7], PYTHIA (ver. 6.406) [144, 145], CATFISH [146, 147] and the string event generator. SUSY simulations will be carried out using a combination of ISAJET and PYTHIA. Simulations of graviton processes will use PYTHIA. BH simulations will be carried out using the CATFISH Monte Carlo (MC) generator. SR and SM simulations will be done with PYTHIA. The setup for each simulation is:

- SUSY:
 - The MSSM mass spectrum is generated with ISAJET;
 - The mass spectrum in SLHA format is fed into PYTHIA;
 - SUSY processes except SM Higgs production are simulated;
 - Unstable SM particles and sparticles are hadronized or decayed with PYTHIA.
- Graviton decay:
 - $f\bar{f} \rightarrow G$ and $gg \rightarrow G$ processes are simulated with PYTHIA as internal processes.
- BHs:
 - The cross section of the BH event is calculated in the CM frame;
 - The initial BH mass is sampled from the differential cross section;
 - The BH is decayed through Hawking mechanism and final n -body event (or remnant);
 - Unstable quanta are hadronized with PYTHIA.
- String resonances:
 - The differential cross section for the $pp \rightarrow \gamma + jet$ process [129] is calculated;

- The total cross section is obtained from Eq. (1.43);
 - The resonance decay is simulated with PYTHIA.
- SM background:
 - $t\bar{t}, Z^0, W, WZ^0, WW$ and Z^0Z^0 SM processes are simulated with PYTHIA.

PYTHIA

PYTHIA is a FORTRAN¹ MC code used for high energy particle collisions. Typically, a high energy collision is a complex process producing a plethora of particles. The main purpose of PYTHIA is to generate a detailed event history, for example the 2×2 hard-process, initial- and final-state radiation, beam remnants, fragmentation, decays etc., for a generic detector. Events are generated using the following three main steps (see also Fig. 3.1):

- *Hard interaction.* The primary hard interaction is generated for process under study through the appropriate cross section. The hadrons are described by a set of parton distribution functions $f(x, Q^2)$ which give the probability of finding a parton with a certain momentum fraction x of the total energy of the proton at the energy scale Q^2 . PYTHIA currently contains about 300 hard processes which are classified according to the number of final particles ($2 \rightarrow 1$ and $2 \rightarrow 2$ hard interactions) or according to the physical processes. When classifying hard processes based on their physical properties, PYTHIA currently supports about 17 different scenarios. Some of the processes relevant for this thesis include hard QCD processes, W/Z production, new gauge boson production, SUSY and extra dimensions.
- *Initial and final state radiation.* Incoming- and outgoing- state radiate before and after the hard interaction through soft or semi-hard processes. For example an initial quark produces a photon as in $q \rightarrow q\gamma$.
- *Quark-gluon confinement.* Quarks and gluons produced in the interaction are hadronized to produce stable particles.

Each event in PYTHIA is stored as an event record in a common block called PYJETS. Origin, present status, momentum, energy, mass and production vertices of the particle are recorded. The PYLIST command provides a summary of the information stored in PYJETS as shown in Table 3.1. Lines 1...9, show the event history, denoted by the exclamation marks around the particle names. The first two lines of the output show the initial 7 TeV protons along the z direction. Lines 3,4 (5,6) show the initial (final) state radiation particles. Line

¹Starting with version 8, PYTHIA is written in C++.

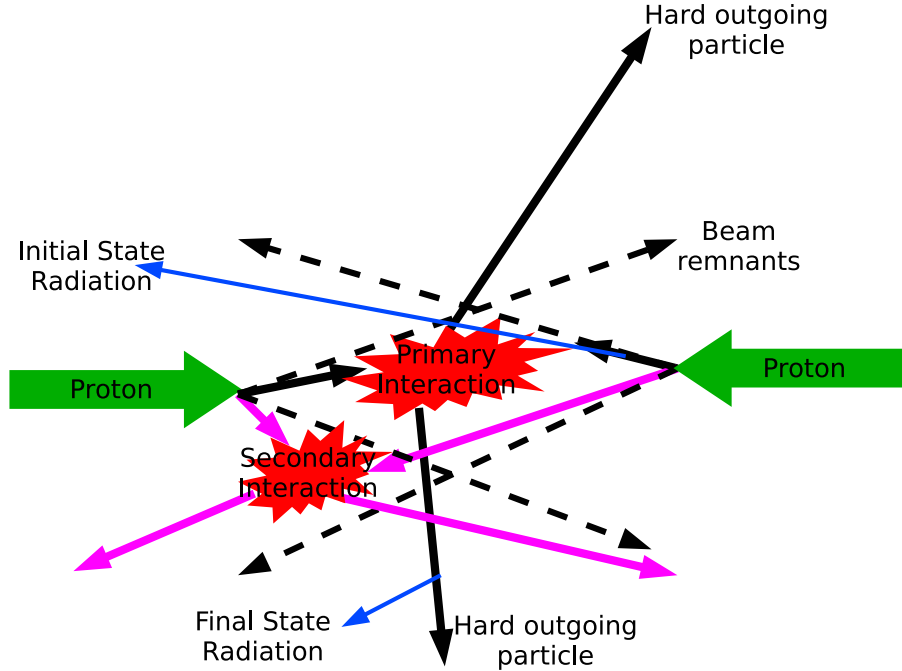


Figure 3.1: 2×2 interaction showing initial and final state radiation, multiple interactions and beam remnants. Adapted from [19].

7 contains the graviton produced from gg fusion which decays into a $q\bar{q}$ pairs (lines 8 and 9). The particles produced in the final state are shown from line 10 onwards. Particle names in brackets signify that these particles further decay. The last line of the output shows the total energy and momentum of the interaction.

ISAJET

ISAJET is another FORTRAN MC for simulating high energy pp collisions. It is similar to PYTHIA, but it is primarily used for parton level studies. Events are generated as follows in four steps:

- Computation of the cross section of the hard scattering process and simulation of the hard scattering.
- Simulation of initial state and final state radiation.
- Hadronization of partons.
- Jet simulation to describe the “soft” partonic interactions, i.e. multiple interactions, beam remnants etc.

Table 3.1: Abridged *PYTHIA* output showing a *pp* collision to produce a graviton (G^*). *Orig* refers to where the current particle originated from. Other symbols have the usual meaning. All quantities are in GeV.

Event listing (summary)							
I	particle/jet	orig	p_x	p_y	p_z	E	m
1	!p+	0	0.000	0.000	7000.000	7000.000	0.938
2	!p+	0	0.000	0.000	-7000.000	7000.000	0.938
3	!g!	1	1.363	0.703	1868.599	1868.600	0.000
4	!g!	2	-1.025	0.267	-2704.946	2704.946	0.000
5	!g!	3	2.289	-1.080	1097.417	1097.419	0.000
6	!g!	4	16.514	13.034	-240.005	240.925	0.000
7	!G*!	0	18.80	11.95	857.41	1338.34	1027.38
8	!u!	7	-443.276	-232.577	358.721	615.846	0.330
9	!ū!	7	462.079	244.531	498.691	722.499	0.330
10	(G*)	7	18.80	11.95	857.41	1338.34	1027.38
11	(\bar{d})	4	5.352	-4.349	3.821	7.891	0.330
12	(g)	4	1.490	-3.330	-0.438	3.675	0.000
13	(g)	4	0.253	0.121	-0.255	0.379	0.000
14	(g)	4	1.849	-6.459	-7.163	9.820	0.000
⋮							
185	pi+	137	-2.183	0.833	1.493	2.776	0.140
⋮							
	sum:		0.00	0.00	0.00	14000	14000

ISAJET stores particle information, momentum, origin and decay products, in a common block. Information about the production vertex is not stored by ISAJET. Contrary to *PYTHIA*, particles are produced/decayed at the origin. Therefore, it lacks detector response simulation. In this thesis *ISASUSY*, included with *ISAJET*, will be used only to generate SUSY particle masses.

CATFISH

CATFISH [146, 147] is FORTRAN MC generator for simulating BH events at the LHC. CATFISH interfaces to the *PYTHIA* MC fragmentation code. Simulations using CATFISH are controlled by a set of external parameters and switches:

- *Fundamental Planck scale*, $1 \leq M_* \leq 14$.
- *Number of large EDs*, $3 \leq n \leq 7$. As discussed in Sect.1.4.2, models with one or two large EDs are excluded. BH production in warped scenarios such as the RS models (see Sect.1.4.3) are not considered in CATFISH

since most theoretical studies concerning black holes at colliders have been derived for a flat extra-dimensional scenario.

- *Gravitational loss model.* Options include the no graviton loss BD model and the YN and YR trapped surface models.
- *Minimum BH mass at formation, M_{min}* in units of M_\star .
- *Quantum BH mass threshold at evaporation, $Q_{min} \sim 1$ TeV.* Q_{min} is defined as the mass of the BH at the end of the evaporation phase.
- *Number of quanta at the end of BH decay, $2 \leq n_p \leq 18$.*
- *Momentum transfer model in parton collision.* Two choices are allowed: M or inverse Schwarzschild radius.
- *Dilepton Invariant Mass Parameters.* (See Sect. 4.1.3.)

CATFISH simulations neglect the energy loss in the balding phase since it is poorly understood. Since emissivities of rotating BHs are not known for all fields, the description of the evaporation phase is also approximated. For simulation purposes, BH generators rely on the Schwarzschild phase. The total decay multiplicity in CATFISH is

$$N = \frac{(n+1)S}{4\pi} \frac{\sum_i c_i \mathcal{R}_i \Gamma_{\mathcal{R}_i}}{\sum_j c_j \mathcal{P}_j \Gamma_{\mathcal{P}_j}}. \quad (3.1)$$

The decay multiplicities per species N_i are

$$N_i = N \frac{c_i \mathcal{R}_i \Gamma_{\mathcal{R}_i}}{\sum_j c_j \mathcal{R}_j \Gamma_{\mathcal{R}_j}}, \quad (3.2)$$

where $\Gamma_{\mathcal{P}_i}$ and $\Gamma_{\mathcal{R}_i}$ are the relative emissivities of Ref. [126, 127], S is the initial entropy of the BH, \mathcal{P}_s and \mathcal{R}_s are spin-dependent power and emissivity

Particle	Color	Flavor	Charge	Spin	dof
Quarks	3	6	2	2	72
Gluons	8		1	2	16
Leptons		3	2	2	12
Neutrinos		3	2	1	6
W, Z			3	3	9
γ			1	2	2
Higgs			1		1
Graviton			1		1

Table 3.2: *Dof's of the known SM particles, Higgs and the graviton.*

normalization factors, respectively and c_i is the number of dof of the particle species i .

Table 3.2 shows the values of c_i for SM particles. The overall dof of a species is the product of the particle's color, flavor, charge and spin [148]. For example, quarks come in 3 color states, 6 flavor states, 2 charge states and two spin states. Therefore, the degree of freedom is $3 \times 6 \times 2 \times 2 = 72$. The ratio of the number of dofs for quarks:bosons:leptons is 72:29:18 with a $\sim 5:1$ ratio between hadrons and leptons.

STRING EVENT GENERATOR

SR simulations are implemented as an external process in PYTHIA using the UPINIT and UPEVNT subroutines. Simulation parameters include M_s , P_{Tmin} and cuts on the emitted particles.

Phenomenology of New Physics at the LHC

In this section we present our analysis of BH, SUSY, graviton and SR events at the LHC. Part of the original work in this chapter is based on Refs. [81, 82, 83].

4.1 SUSY and BH event analysis

Our analysis of SUSY and BH events is based on visible energy, missing momentum of leptons and hadrons, event shape variables and high- P_T leptons. Fig 4.1 shows visible energy, \cancel{P}_T and sphericity distribution for the five ATLAS points of Table 1.4, where all SUSY processes except SM Higgs production have been implemented. For the purposes of the first part of our analysis, the difference between the five points is not significant and any of them can be chosen as SUSY benchmark. In the following, we will consider point A. This is justified by the fact that point A allows for SUSY Higgs production [149]. Since BHs may evaporate into Higgs (see Sect. 1.5 below), a meaningful comparison of SUSY and BH events requires the presence of the Higgs channel in both models. Moreover, distinguishability of SUSY and BH events must be assessed by minimizing the differences between the two models. Since BH events are characterized by up to several TeV of \cancel{P}_T SUSY points with large \cancel{P}_T such as point A, must be considered.

The parameters for the BH benchmark model are fundamental Planck scale $M_\star = 1$ TeV, minimum BH mass $M_{min} = 2$ TeV, classical-to-quantum threshold $Q_{min} = 1$ TeV, six extra-dimensions ($n = 6$) and two-body final decay ($n_p = 2$). Particles produced in the initial-radiation phase are removed by imposing P_T cuts of 5 GeV and 15 GeV for leptons and photons+hadrons, respectively [146, 147].

In Sect. 4.1.1 we will discuss missing energy and momentum followed by an analysis of event shape variables in Sect. 4.1.2. BH events tend to be

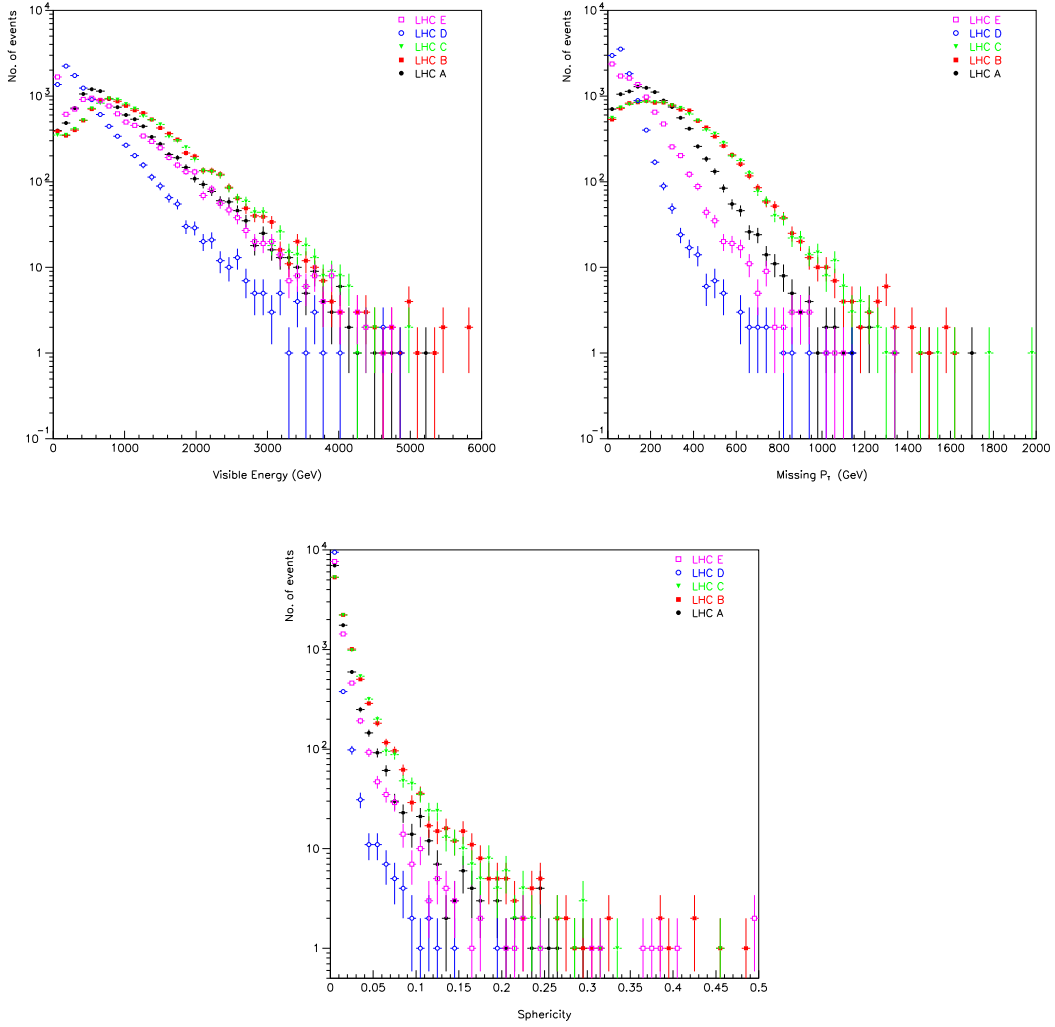


Figure 4.1: Comparison of visible energy (top left), \cancel{P}_T (top right) and sphericity (bottom) for 10000 events for the five ATLAS points of Table 1.4 (A: filled black circles, B: filled red squares, C: filled green triangles, D: open blue circles and E: open pink squares).

more spherical than SUSY events due to the spherical nature of the Hawking radiation; this is specially evident for high-mass BHs. The formation of a stable BH remnant at the end of the evaporation phase also helps to discriminate SUSY and BH events because of the large amount of energy which is carried away by the remnant.

Analysis of isolated dilepton events is another powerful method to distinguish the two models and will be discussed in Sect. 4.1.3. This is due to the fact that SUSY dileptons typically originate from a single decay chain whereas leptons are rarely emitted by BHs (the hadron-to-lepton ratio is approximately

5:1) and are uncorrelated; i.e. they can be emitted at any angle w.r.t. beam axis.

4.1.1 Energy and Momentum

Figure 4.2 shows visible energy, \cancel{P}_T and P_T of leptons and hadrons & photons for 10,000 SUSY and BH benchmark events. The amount of visible energy and \cancel{P}_T is comparable for the two scenarios, even in the absence of a BH remnant. This is due to the presence of invisible channels in both models: neutrinos+gravitons for the BH and LSP for SUSY. The flavor of the decay products is a better discriminator. SUSY interactions do not produce leptons with energy above the TeV since isolated leptons are produced by the decay of sparticles with typical energy of less than a few hundred GeV. On the contrary, quanta produced in the BH decay are characterized by an average energy $E \sim M/N$, where the multiplicity N is less than 10 for typical BHs at the LHC. Since Hawking evaporation does not distinguish leptons from hadrons, hard leptons with energy up to several TeV are likely to be produced during the BH decay. This suggests that isolated leptons may provide a powerful means to discriminate the two models. This is indeed the case, as we shall see in Sect. 4.1.3.

Fig. 4.3 shows how variations in the BH Planck phase affect the observables of Fig. 4.2. The plots compare zero (BH remnant)-, two- and four-body decays. The BH is expected to have shed its electric and color charges by the time the remnant is formed¹. The BH remnant is thus undetectable and a source of \cancel{P}_T in addition to neutrinos and gravitons which are emitted during the Hawking evaporation phase. This leads to a larger difference in \cancel{P}_T between SUSY and BH models. The visible P_T in hadrons & photons is sensibly reduced in the presence of a BH remnant. The BH remnant carries away energy which otherwise would have been emitted in visible channels (mostly hadrons) during the BH decay phase. The leptonic channel is essentially unaffected by the presence of a BH remnant since leptons are rarer than hadrons in the BH decay phase. Variations in the energy distribution of the leptonic channel are thus suppressed compared to the hadronic channel. Changes in the number of final Planckian hard quanta do not produce significant differences in the distributions; more quanta of lower energy behave statistically like less quanta with higher energy. Provided that the BH decays at the end of the Hawking phase, it is thus safe to set the number of Planckian quanta to $n_p = 2$ (or $n_p = 4$), although BHs may decay in different numbers of particles on an event-to-event basis. Variations in the classical-to-quantum threshold Q_{min} are also not expected to cause significant differences in the energy/momentum distributions. A higher threshold increases the emission in the Planck phase while decreasing Hawking radiation. Since these phases differs only in relative

¹For an alternative scenario see, Ref. [150].

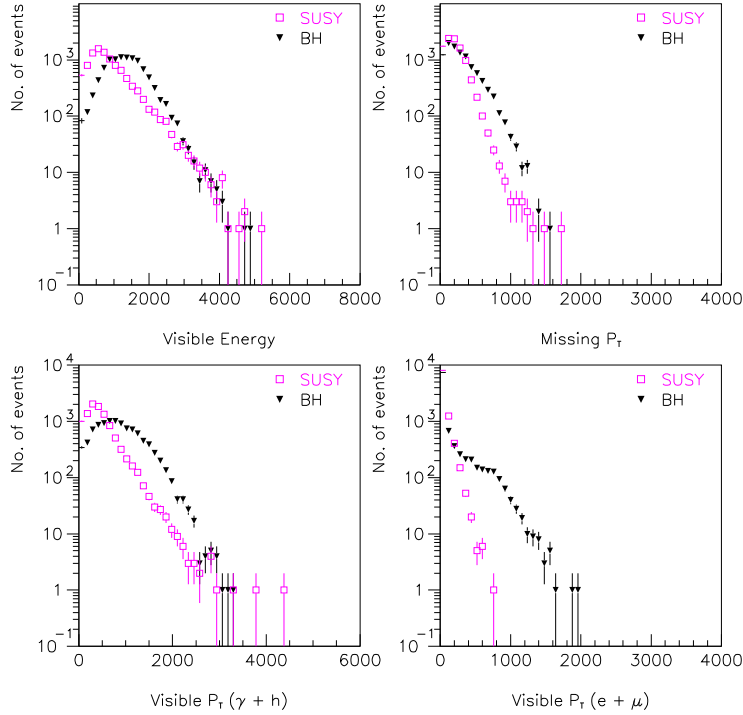


Figure 4.2: Comparison of 10,000 SUSY and BH benchmark events at the LHC. Visible energy and P_T (top panels) are comparable due to the presence of invisible channels in both models. Leptons with large P_T provide instead an effective discriminator (bottom right panel).

greybody factors, the effect is too small to be detected.

Fig. 4.4 shows visible energy, P_T , and visible transverse momenta of leptons and hadrons & photons for different values of the fundamental Planck scale. Higher values of M_* lead to more massive BHs, higher multiplicity and more energetic quanta. This causes a significant increase in missing and visible momenta. If the value of the fundamental Planck scale happens to be large, BHs are likely to be detected and easily distinguished from SUSY through detection of highly-energetic isolated leptons and hadronic jets. P_T of several TeV would also be observed. However, the LHC is expected to produce very light BHs (see Fig. 1.10) therefore such an analysis may not provide the most effective discriminators [146, 147, 151, 152, 153, 154, 155, 156]. The study of leptonic final states alleviates this problem. See Sect. 4.1.3.

4.1.2 Event shape variables

Event shape variables, such as the sphericity, 2nd Fox-Wolfram moment and thrust, and jet masses defined in Chapter 2 can be used to complement the

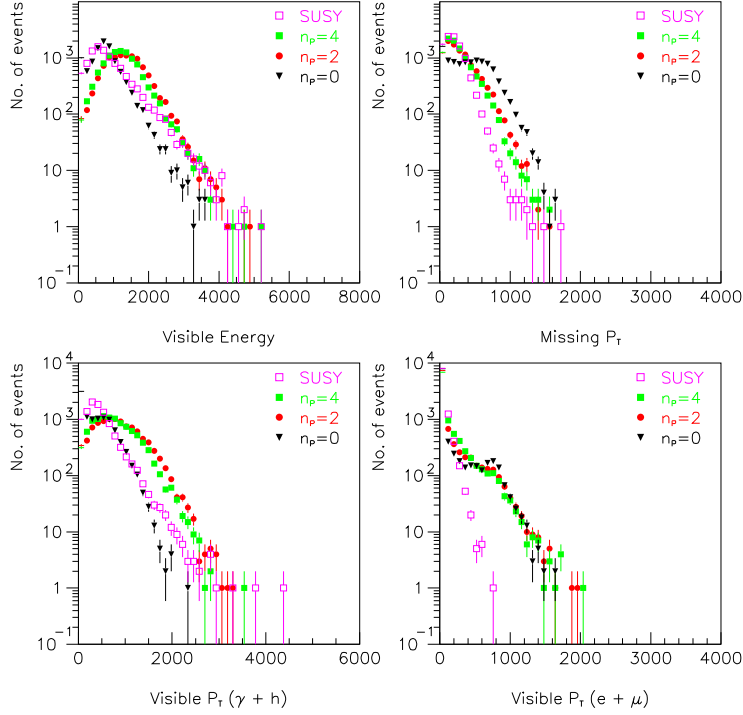


Figure 4.3: Distribution of visible energy, \cancel{P}_T and transverse momenta of leptons and hadrons \mathcal{E} photons. SUSY plots are shown as pink open squares. The four plots show the effect of different decay modes in the Planck phase of ten-dimensional BHs: remnant formation ($n_p = 0$, black filled triangles), two-body decay ($n_p = 2$, red filled circles) and four-body decay ($n_p = 4$, green filled squares). The fundamental Planck scale is $M_\star = 1$ TeV.

above analysis. Our analysis shows that BH events are more spherical because of the nature of Hawking radiation and the production of larger number of jets for SUSY decays. Formation of a BH remnant and high values of the fundamental scale lead to a significant higher sphericity than SUSY events (top panels of Fig. 4.5). The 2nd Fox-Wolfram moment (middle panels of Fig. 4.5) is stable versus changes in the BH Planck phase and provides a good SUSY/BH discriminator. BH models with higher M_\star can be differentiated more easily from SUSY events.

Similar conclusions can be reached by looking at jet masses and number of jets. SUSY events generate more and lighter jets than the BH model due to copious production of quarks (Fig. 4.6). The difference is again especially significant for high values of M_\star and in the presence of BH remnants. Absence of sub- Q_{min} hard jets could provide strong evidence for BH remnant production. (See the suppression of heavy jets below the classical-to-quantum threshold $Q_{min} = 2$ TeV in the top leftmost panel of Fig. 4.6.)

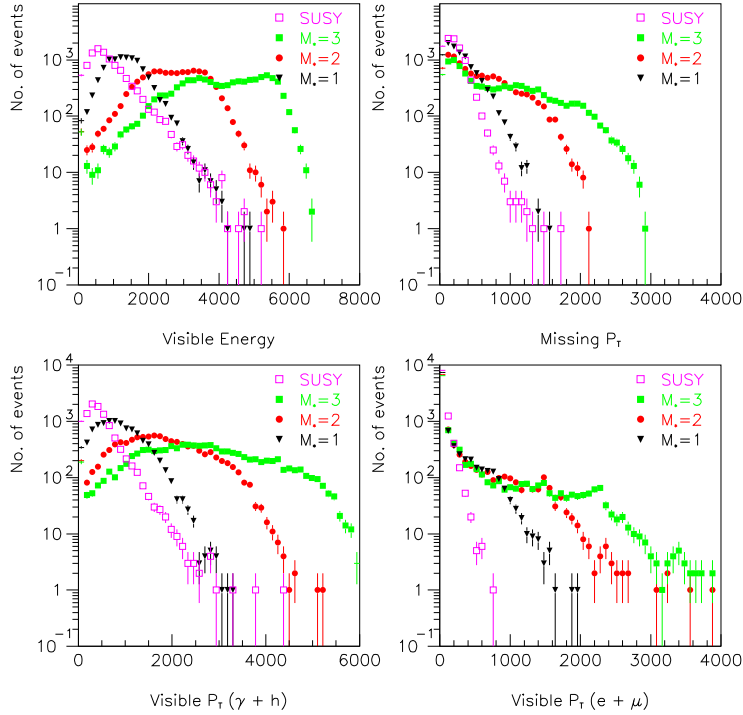


Figure 4.4: Distribution of visible energy, P_T and transverse momenta of leptons and hadrons \mathcal{E} photons. SUSY plots are shown as pink open squares. The plots show the effect of varying the fundamental Planck scale: $M_\star = 1$ TeV (black filled triangles), $M_\star = 2$ TeV (red filled circles) and $M_\star = 3$ TeV (green filled squares). The ten-dimensional BHs decay in two hard quanta at the end of the evaporation phase.

4.1.3 High- P_T leptons

SUSY events can be categorized by the number of high P_T leptons. Events with no isolated leptons can occur when a SUSY decay chain ends in the production of jets. Events with a single isolated high P_T lepton are difficult to identify because of the large SM background from W decays into leptons. Events with two isolated high P_T leptons are characterized by a lower signal-to-background ratio (due to the low branching ratio into leptons) with respect to zero lepton or one lepton events. Nevertheless, dileptons provide a clear signature because the presence of two isolated leptons can be accurately measured with early LHC data.

Production of gluinos and squarks dominate SUSY production at the LHC. The bulk of the decay modes of these sparticles are characterized by the production of the lighter chargino and two neutralinos. Thus, the decay of the second lightest neutralino $\tilde{\chi}_2^0$ forms an important part of this analysis. Charginos decays are more difficult to analyse as they involve either a missing neutrino or

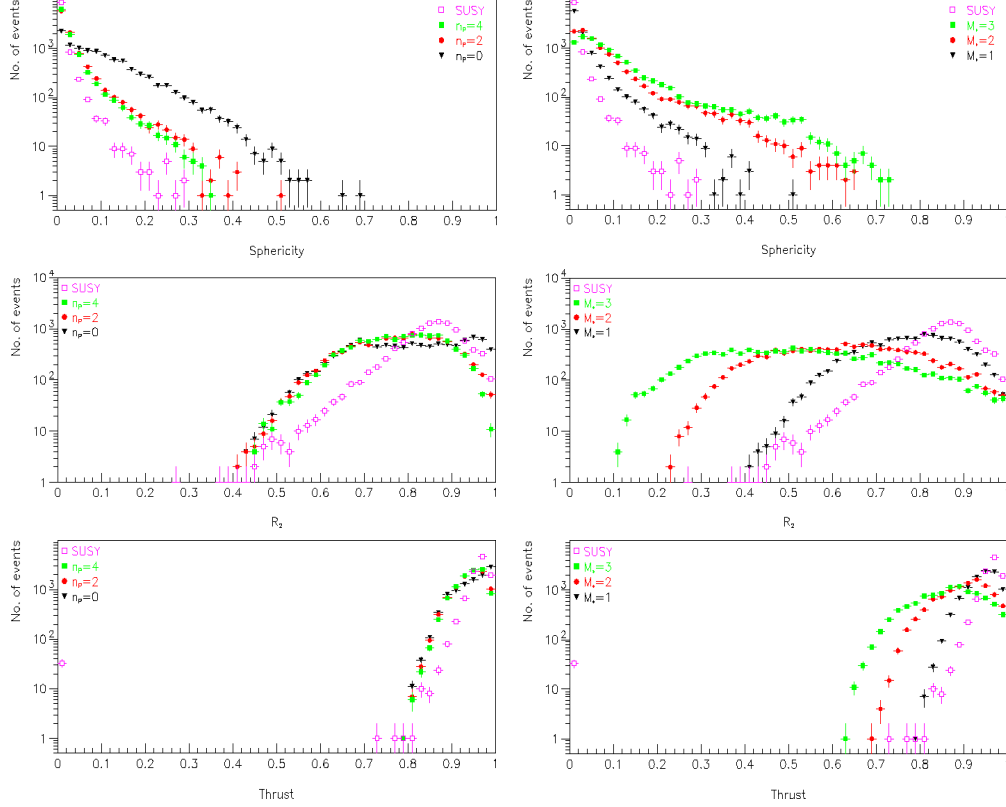


Figure 4.5: *Sphericity (top panels), 2nd Fox-Wolfram moment (middle panels) and thrust (bottom panels) for 10,000 BH and SUSY events. The left panels show the effect of different Planckian decay modes: BH remnant (black filled triangles), two-body decay (red filled circles) and four-body decay (green filled squares). The fundamental scale is $M_\star = 1$ TeV and the number of EDs $n=6$. The right panels show the effect of different fundamental scales: $M_\star = 1$ TeV (black filled triangles), 2 TeV (red filled circles) and 3 TeV (green filled squares). The ten-dimensional BHs decay in two quanta at the end of the Hawking phase.*

quark jets. Two body decays of neutralinos have large branching ratios. If two body decays are not kinematically allowed, then the three body leptonic mode dominates [137]. A list of dominant SUSY interactions leading to dileptons at the LHC is described below for the LHC points of Table 1.4.

The relevant decay chains for ATLAS point A are shown in Fig. 4.7. The third decay chain allows the separation of leptons from the hadronic background [157]. Requiring the leptons to be isolated and have high P_T (in excess of 15 GeV) ensures that they were indeed produced from the above decay chain and not from the initial 2×2 hard interaction. In the rest frame of the second lightest neutralino, the dilepton invariant mass is

$$M_{ll} = \left[M_{\tilde{\chi}_2^0}^2 + M_{\tilde{\chi}_1^0}^2 - 2 M_{\tilde{\chi}_2^0} M_{\tilde{\chi}_1^0} \left(1 + \frac{P_{\tilde{\chi}_1^0}^2}{M_{\tilde{\chi}_1^0}^2} \right) \right]^{1/2}. \quad (4.1)$$

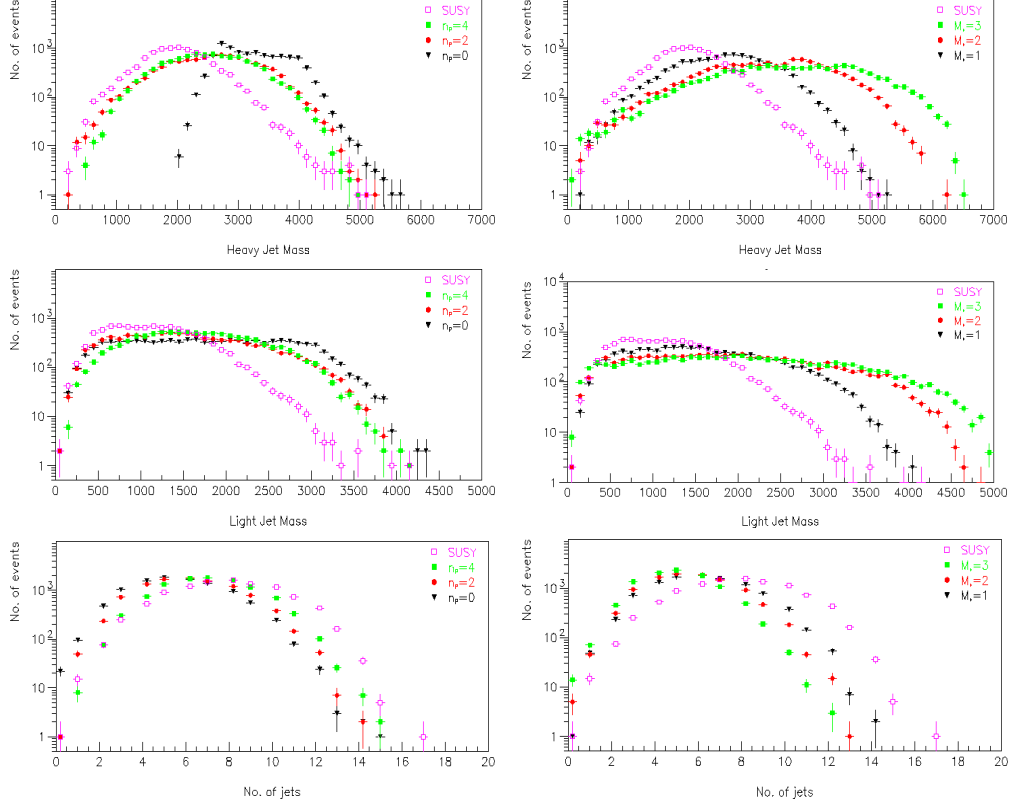


Figure 4.6: Heavy and light jet masses (top and middle panels) and number of jets (bottom panels) for 10,000 BH and MSSM events. Symbols are like in previous figures.

The invariant mass is a function of the masses of the particles involved in the decay. Since the momentum of the LSP is not constrained, the invariant mass distribution shows an edge at ~ 100 GeV. This is because M_{ll} reaches a maximum when the LSP is produced at rest. In that case the dilepton invariant mass is the difference between the masses of the LSP and $\tilde{\chi}_2^0$ which is ~ 100 GeV for point A.

Heavy sparticles are produced at points B and C, where $m_0=400$ GeV and $m_{1/2}=400$ GeV. The dominant decay mode at these points is $\tilde{\chi}_2^0 \rightarrow \tilde{\chi}_1^0 h$ because $\tilde{\chi}_2^0$ decay into sleptons is forbidden due to the high mass of the slepton [8, 9, 10]. Dileptons are produced from the decay of heavy charginos. Thus, the dilepton invariant mass plot does not have an edge as observed at point A. The large value of $\tan\beta$ at point C increases production of Z^0 bosons and thus the number of dileptons.

Point D ($m_0=200$ GeV, $m_{1/2}=100$ GeV) is characterized by light SUSY particles, thus sparticle production rates are large [149]. The dominant SUSY processes, where the percentages in parenthesis are the corresponding BRs, is $\tilde{g}g$ with $\tilde{g} \rightarrow \tilde{b}\bar{b}$ (89%) $\rightarrow \tilde{\chi}_2^0 b\bar{b}$ (86%) $\rightarrow \tilde{\chi}_1^0 b\bar{b}l^+l^-$ (33%) [8, 9, 10]. The above

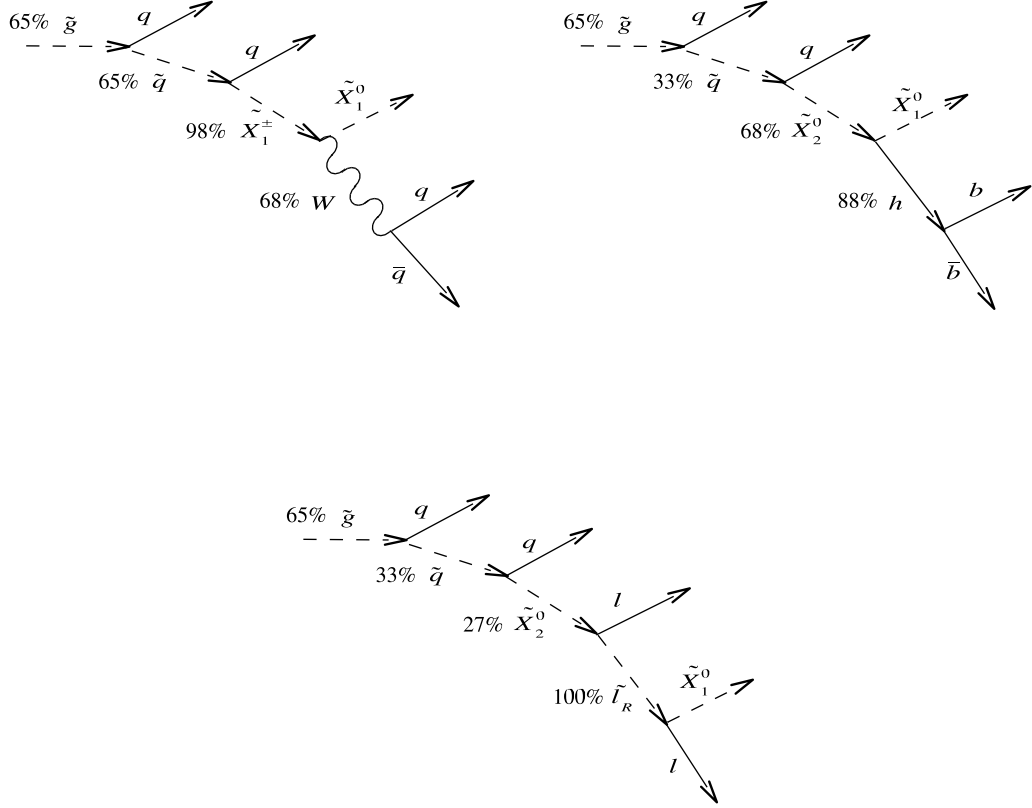


Figure 4.7: The top three SUSY decay chains at point A and their branching ratios.

interactions imply that sparticle decays at this point are characterized by b jets and dileptons.

At point E ($m_0=800$ GeV and $m_{1/2}=200$ GeV) gluino production is dominant because $M_{\tilde{g}} < M_{\tilde{q}}$. Neutralino decay into sleptons is suppressed because of the high mass of the slepton. There is significant Z^0 production a feature common to models with large $\tan\beta$. Dominant processes and branching ratios at this point are $\tilde{\chi}_{3,4}^0 \rightarrow Z^0 \tilde{\chi}_{1,2}^0$ (39%) and $\tilde{\chi}_2^0 \rightarrow Z^0 \tilde{\chi}_1^0$ (32%) [8, 9, 10]. Dileptons are produced from $\tilde{\chi}_2^0 \rightarrow \tilde{\chi}_1^0 l^+ l^-$ (6%) [8, 9, 10] and from the decay of Z^0 into leptons.

Point LM1 [6, 11] ($m_0=60$ GeV and $m_{1/2}=250$ GeV) is characterized by a large value of $\tan\beta$, which leads to a lower mass of $\tilde{\tau}$ and \tilde{b} . This results in the decay of the second lightest neutralino into $\tilde{\tau}$, producing dileptons via the process $\tilde{\chi}_2^0 \rightarrow \tilde{\tau}_1^\pm \tau^\mp \rightarrow \tau^+ \tau^- \tilde{\chi}_1^0$ and $\tilde{\chi}_2^0 \rightarrow \tau^+ \tau^- \tilde{\chi}_1^0$, where the τ decays in the lepton channel [158, 159, 160]. Moreover, Z^0 production is enhanced

due to higher sbottom production. This is due to the decay chain $\tilde{b}_1 \rightarrow \tilde{\chi}_{3,4}^0 b, \tilde{\chi}_{3,4}^0 \rightarrow Z^0 \tilde{\chi}_{1,2}^0$ [158, 159]. Since the mass of the gluino is larger than the squark mass, the dominant process is $\tilde{g} \rightarrow \tilde{q}q$ as at point A. The branching ratios of the dominant decays are $\tilde{\chi}_2^0 \rightarrow \tilde{\tau}_1^\pm \tau^\mp$ (46%), $\tilde{\chi}_1^\pm \rightarrow \tilde{\nu}_l l$ (36%) and $\tilde{\chi}_2^0 \rightarrow \tilde{l}_R l$ (11.6%) [11]. The invariant mass distribution of dileptons is expected to show an edge due to the process $\tilde{\chi}_2^0 \rightarrow \tilde{l}_R l$.

The SM dilepton background contribution can be removed by applying suitable cuts on the transverse momenta of the leptons [96]: $P_{Tl} \geq 15$ GeV, $|\eta_l| < 2.5$, isolation cut $\sum_l P_{Tl} < 7$ GeV in a cone of $R = 0.2$, and $\cancel{p}_T \geq 200$ GeV. Here P_{Tl} is the transverse momentum of the leptons, $R = \sqrt{\Delta\eta^2 + \Delta\phi^2}$, where ϕ and θ are the azimuthal and polar angles of the lepton w.r.t. beam axis. The use of isolated dileptons as a SUSY signature has been previously discussed in the literature [149, 161, 162]. Although the production of leptons is not as high as the production of colored particles, high energy isolated leptons provide a cleaner environment by allowing the removal of the SM background. The dominant SUSY interaction for opposite-sign, same-flavor (OSSF) dileptons at ATLAS point A is $\tilde{\chi}_2^0 \rightarrow l^\pm \tilde{l} \rightarrow l^\pm l^\mp \tilde{\chi}_1^0$ with a 27% branching ratio (BR) [157]. The maximum dilepton invariant mass for this interaction is

$$M_{ll}^{max} = m_{\tilde{\chi}_2^0} \left[\left(1 - \frac{m_{\tilde{l}}^2}{m_{\tilde{\chi}_2^0}^2} \right) \left(1 - \frac{m_{\tilde{\chi}_1^0}^2}{m_{\tilde{l}}^2} \right) \right]^{1/2} \sim 100 \text{ GeV}. \quad (4.2)$$

Dilepton production in BH events differ greatly from dilepton production in the MSSM. There is no single process of dilepton production for BHs. Dileptons are either produced by the BH directly or by the decay of heavier particles such as the Z^0 boson, $t\bar{t}$ pairs or a combination of the two. Therefore, the BH dilepton invariant mass does not show a sharp cut-off at high energy. Since the decay of top quarks into leptons is rare [163], and the BR of Z^0 into leptons is small, $\Gamma(l^+l^-)/\Gamma_{\text{tot}} \sim 0.034$ [1], production of OSSF dileptons is less frequent for BHs than SUSY events. Our analysis shows that an OSSF dilepton event occurs approximately every 100 BH and 20 SUSY events, with a $\sim 1:5$ ratio of BH-to-SUSY dilepton events at fixed luminosity.

Fig. 4.8 shows the invariant mass distribution for 2000 SUSY OSSF dilepton events and 2000 BH OSSF dilepton events. As was expected, the SUSY invariant mass distribution shows a sharp edge at ~ 100 GeV. The BH invariant mass distribution is characterized by two peaks, at ~ 90 GeV and a smaller peak at 1 TeV, and a tail at high P_T . The first peak is due to dilepton events from single Z^0 bosons which are directly emitted by the BH. This is the dominant channel of OSSF dilepton production in BH events. The peak at 1 TeV is due to dileptons emitted at the end of the Hawking phase [146, 147]. The BH mass and the number of final hard quanta at the end of the Hawking phase have been chosen to be $Q_{min}=1$ TeV and $n_p=2$, respectively. Since the BH at the end of the Hawking phase is expected to be electrically neutral,

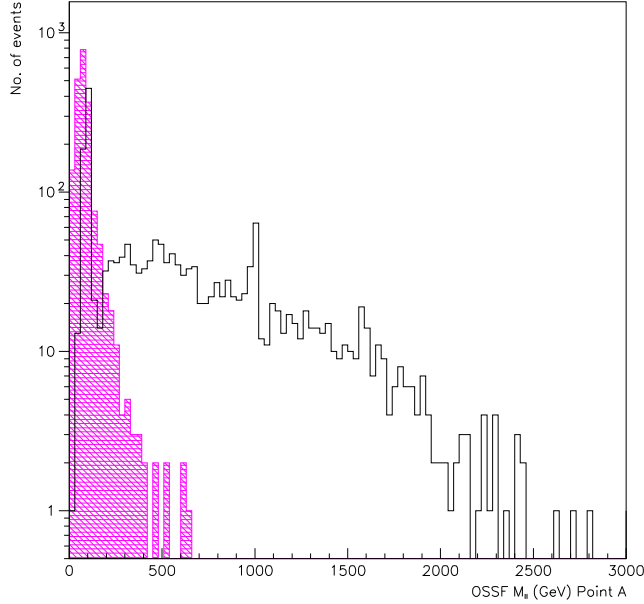


Figure 4.8: *Invariant mass distribution (in GeV) for 2000 SUSY and BH OSSF dilepton events for point A. The SUSY distribution (shaded pink histogram) shows the typical endpoint due to the presence of the LSP. The high- P_T tail of the BH distribution is originated by uncorrelated lepton pairs emitted during the Hawking evaporation phase. The final BH decay is in two-quanta. The SM background is negligible.*

isolated OSSF dilepton events can occur. This peak is expected to be smeared out in a more realistic description of the final BH phase [81]. The high- M_{ll} tail of the distribution is originated by pairs of uncorrelated leptons from the BH.

Fig. 4.9 shows the invariant mass distribution for 900 same-sign (SS) SUSY and BH events. In SUSY SS dileptons are produced by $\tilde{\chi}_2^\pm \rightarrow W^\pm \tilde{l}^\pm$, $\tilde{\chi}_1^\pm \rightarrow W^\pm \tilde{\chi}_1^0$, and from top quark decay into leptons. SS dileptons from BHs are originated either from the BH itself or from the decay of heavier quarks and bosons (t, \bar{t}, W, Z^0). In both cases SS dilepton events are expected to be rare because of the low BR of W into leptons ($\sim 11\%$ [1]). SS dileptons are selected using the same cuts of the OSSF channel. The high- M_{ll} tail of the BH invariant mass distribution can be clearly distinguished from the SS case. Isolation requirements reduce the SM background to virtually zero [164, 165].

Dilepton events with same sign and/or opposite flavor leptons can also be used as discriminators (Fig. 4.10). The “democratic” nature of BH decay makes events with same/opposite flavor leptons roughly equally probable, whereas BRs of SUSY events favor same-flavor dileptons. OS dileptons from the decay of \tilde{X}_2^0 are of the same flavor. On the other hand, leptonic decays of

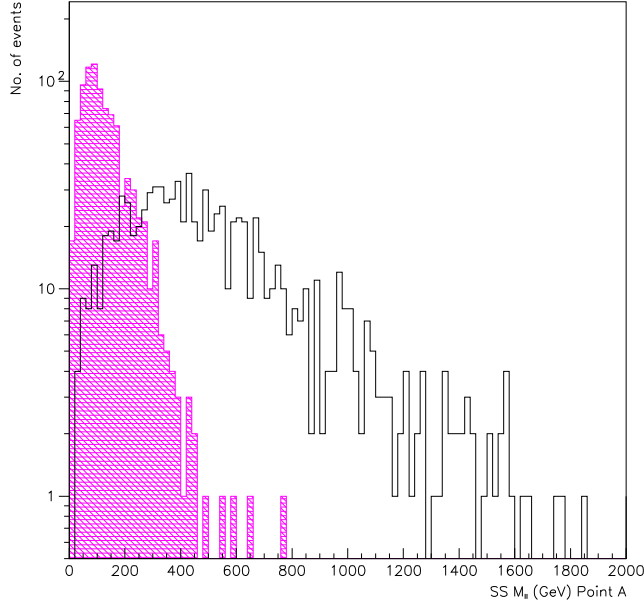


Figure 4.9: *Invariant mass distribution for 900 same-sign dilepton events at point A. The SM background is negligible.*

charginos or third generation quarks and squarks would produce equal amounts of opposite-sign, opposite flavor (OSOF) dilepton pairs as compared to same flavor lepton pairs [14, 142, 143].

Table 4.1 shows the BRs of same-/opposite-sign, same-/opposite-flavor isolated dilepton events for SUSY and BH processes. The dominant channel is the OSSF channel for both models. However, SUSY and BH events can be easily discriminated by comparing the rate of same-flavor events to the rate of opposite-flavor events.

Table 4.1: *BRs of high- P_T isolated dileptons for SUSY and BH models. 21,000 and 100,000 events were simulated in the two cases, respectively, yielding approximately 1000 dilepton events. OS(SS) stands for opposite (same) sign and OF(SF) denotes opposite (same) flavor.*

High P_T isolated dileptons	SUSY	%	BH	%
OSSF	768	73	523	50
SSSF	65	6	103	10
OSOF	169	16	341	32
SSOF	52	5	87	8

The number of isolated, high- P_T leptons can also be used to complement

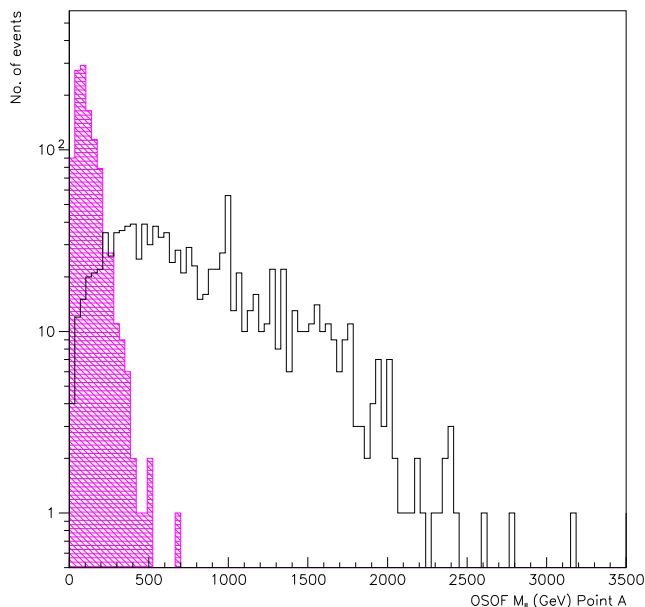


Figure 4.10: *Invariant mass distribution for 1100 OSOF dilepton events at point A. The SM background is negligible.*

the dilepton analysis (Fig. 4.11). SUSY events are capable of producing up to five isolated leptons from the cascade decay of heavy sparticles. Events with $\tilde{\chi}_2^0 \tilde{\chi}_2^0$ or $\tilde{\chi}_1^\pm \tilde{\chi}_2^0$ may produce four or three isolated leptons, respectively [166]. On the contrary, events with three or more isolated leptons are very suppressed in BH decays at the LHC energy. Although multilepton events are rare, there is very little background and they could be effectively used to distinguish the MSSM and the BH model.

Other effective discriminators can be constructed by looking at dilepton events with same sign and/or opposite-flavor leptons. The “democratic” nature of the BH decay makes all dilepton events roughly equally probable, whereas the MSSM favors same-flavor dileptons. Presence of hard opposite-flavor leptons is a clear indication of BH decay (Fig. 4.12). Our analysis shows that 73% of SUSY dilepton events are OSSF, compared to only 50% in the BH model. Conversely, opposite-flavor events are twice more frequent in the BH model (40%) compared to the MSSM (21%).

Dilepton analysis at other LHC points

Figure 4.13 shows the dilepton invariant mass distributions for points B and C. The background cuts remove the SM contribution. Unless otherwise stated all dilepton histograms in this section show 2000 OSSF events, 900 SS events and 1100 OSOF events for both SUSY and SM. The SUSY invariant mass

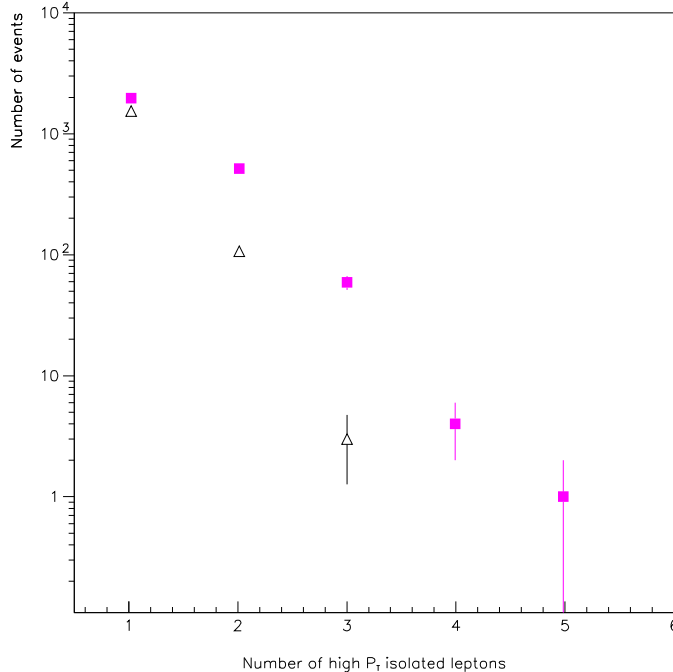


Figure 4.11: Histogram of the number of events with high- P_T leptons for 10,000 MSSM (pink filled squares) and BH interactions (black open triangles). The number of BH events with three isolated leptons is smaller than the number of SUSY events by a factor of ~ 20 . The probability of producing BH events with four or more leptons is virtually zero.

distribution is represented as the shaded (pink) histogram.

Table 4.2: BRs of high- P_T isolated dileptons for SUSY points B and C for 50,000 events. The high value of $\tan\beta=10$ for point C manifests itself as a greater production of OSSF dileptons.

High P_T isolated dileptons	OSSF	OSOF
Point B	12%	11.5%
Point C	16%	11.6%

The dilepton invariant mass distributions for point D (left panel) and E (right panel) are shown in Fig. 4.14. From the edge in the OSSF invariant mass distribution (top panel of Fig. 4.14) the difference in mass of the two lightest neutralinos can be obtained: $M_{\tilde{\chi}_2^0} - M_{\tilde{\chi}_1^0} \sim 50$ GeV. \cancel{P}_T calculations are generally not performed at point D [14, 142, 143]. This is because lepton isolation requirements and the presence of b jets are effective in reducing the SM background [8, 9, 10]. The bottom panel of Fig. 4.14 shows the OSOF dilepton distribution for ~ 2600 SUSY and BH events. More than half of the

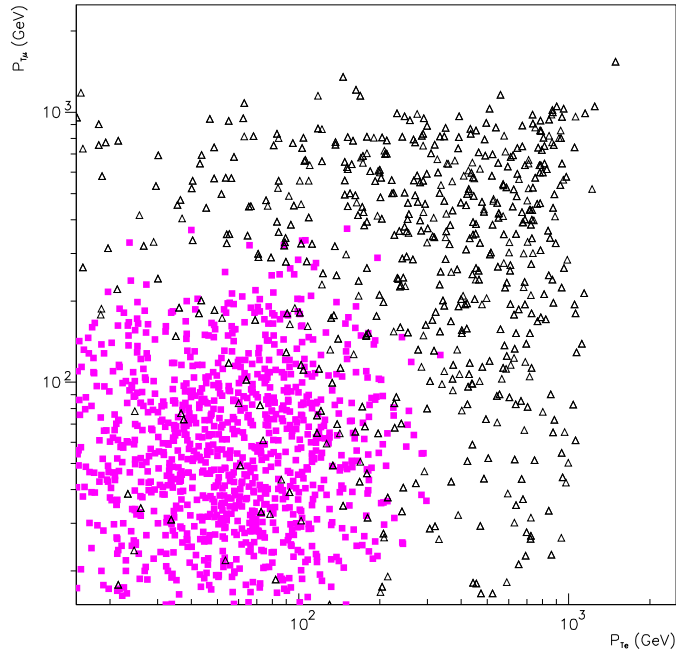


Figure 4.12: P_T scatter plot for ~ 1000 isolated opposite-flavor dilepton events for SUSY (pink filled squares) and BHs (black open triangles). BH leptons are harder than SUSY leptons and show a larger spread in P_T .

background contribution is from $\bar{t}t$ events [160]. Simulations show that this background is negligible due to the low BR of W bosons into leptons. The OSOF dilepton invariant mass distribution at point E is characterized by the Z^0 peak and an undistinct invariant mass edge. The dilepton distribution for point LM1 is shown in Fig. 4.15. The edge in the OSSF dilepton invariant mass distribution is not as evident as in point A because of the large amount of missing momentum which is carried away by the neutrinos in the τ decay [160].

Therefore, in conclusion, it is observed that irrespective of the LHC point the dilepton invariant mass always provides effective discrimination between SUSY and BHs.

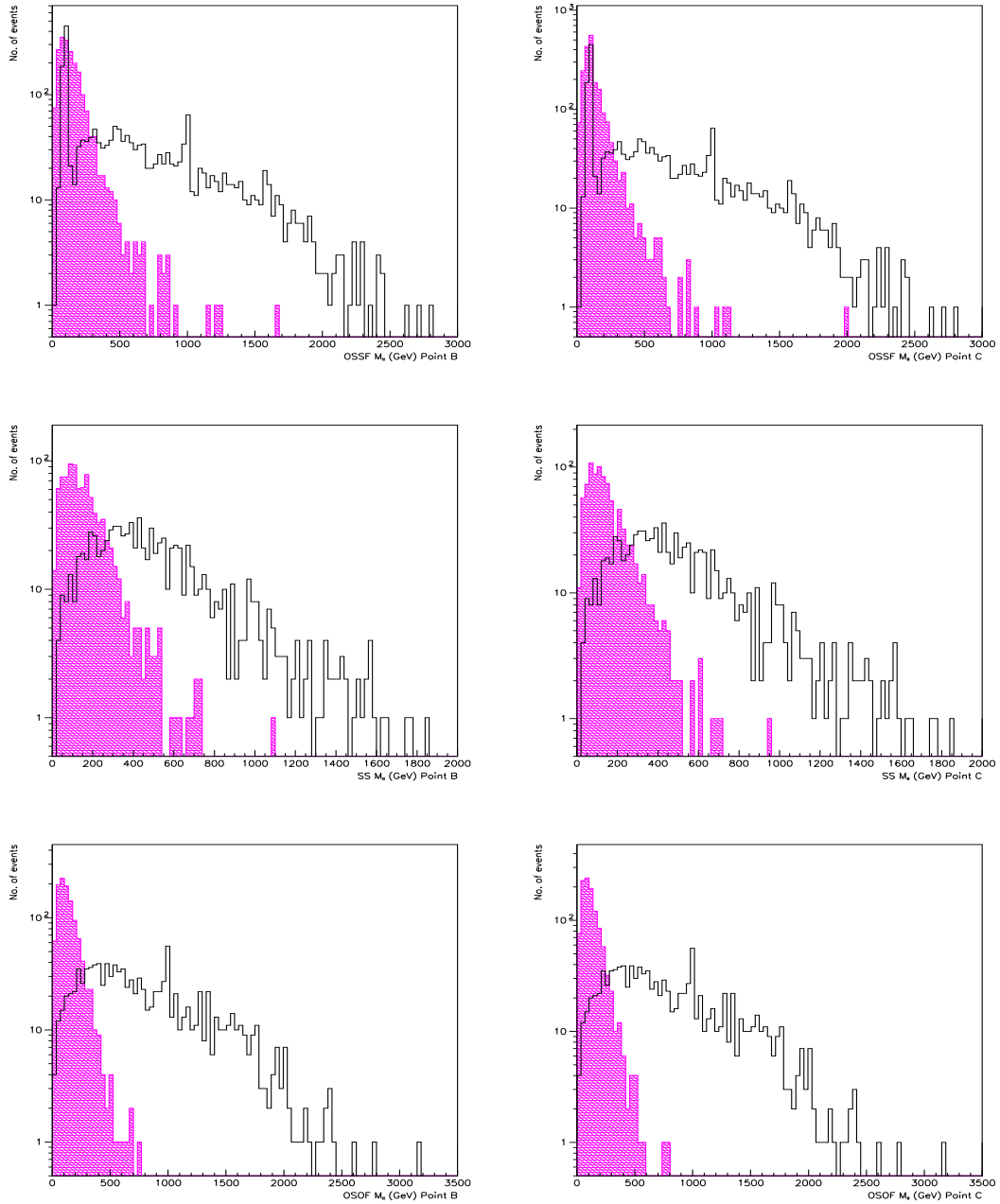


Figure 4.13: *Invariant mass distributions at point B (left panels) and point C (right panels). OSSF (top panels), SS (middle panels) and OSOF (bottom panels) distributions clearly discriminate SUSY and BH events.*

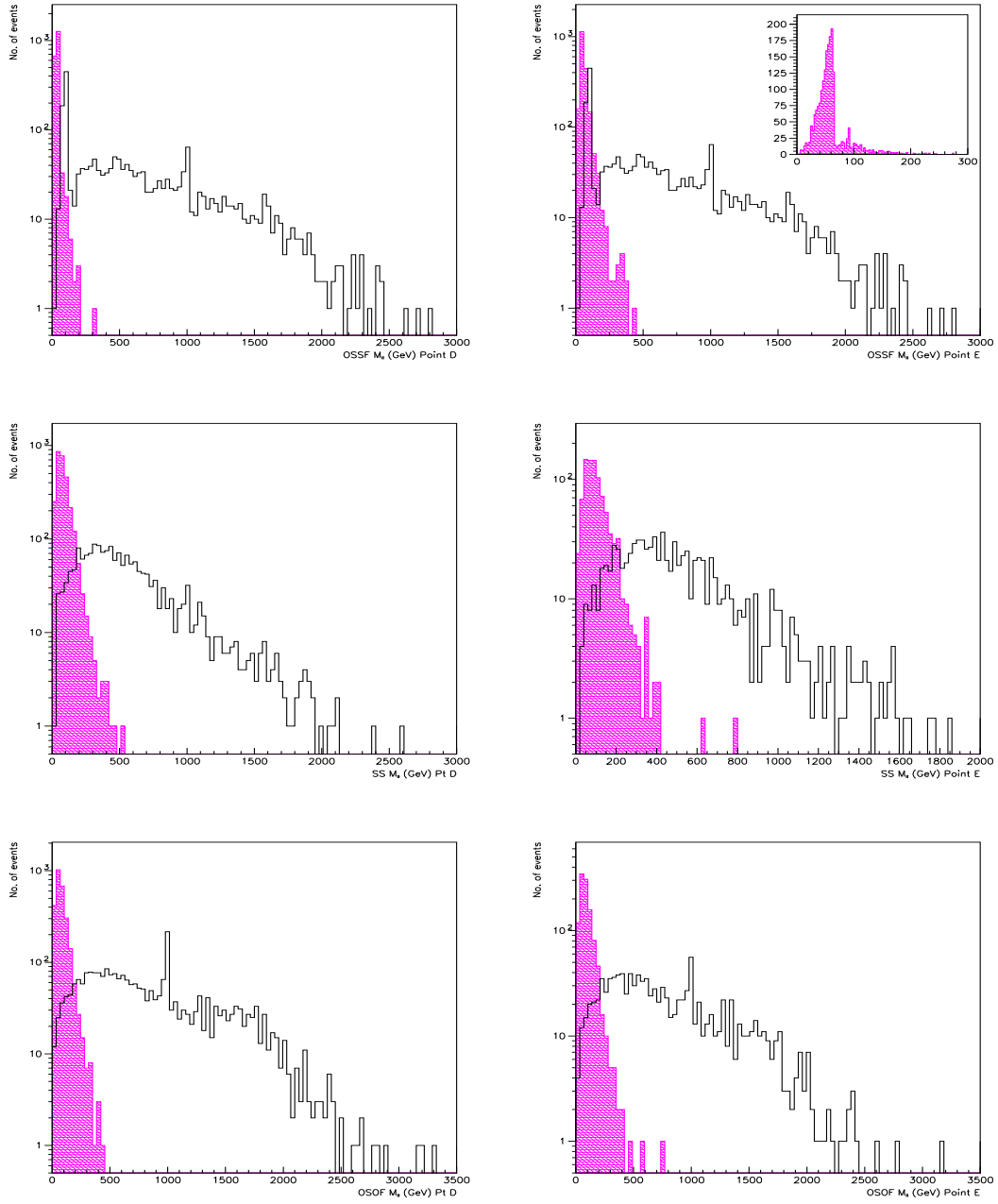


Figure 4.14: Invariant mass distributions at point D (left panels) and point E (right panels). Top Panel: Distribution of 2000 SUSY and BH OSSF dilepton events. At point E there is enhanced Z^0 production because of a high value of $\tan\beta$. Middle Panel: Event distribution for ~ 1700 SUSY and BH SS dilepton events. The SM background is negligible. Bottom Panel: SUSY and BH distribution for ~ 2600 OSOF events. The major SM background due to $\bar{t}t$ is negligible.

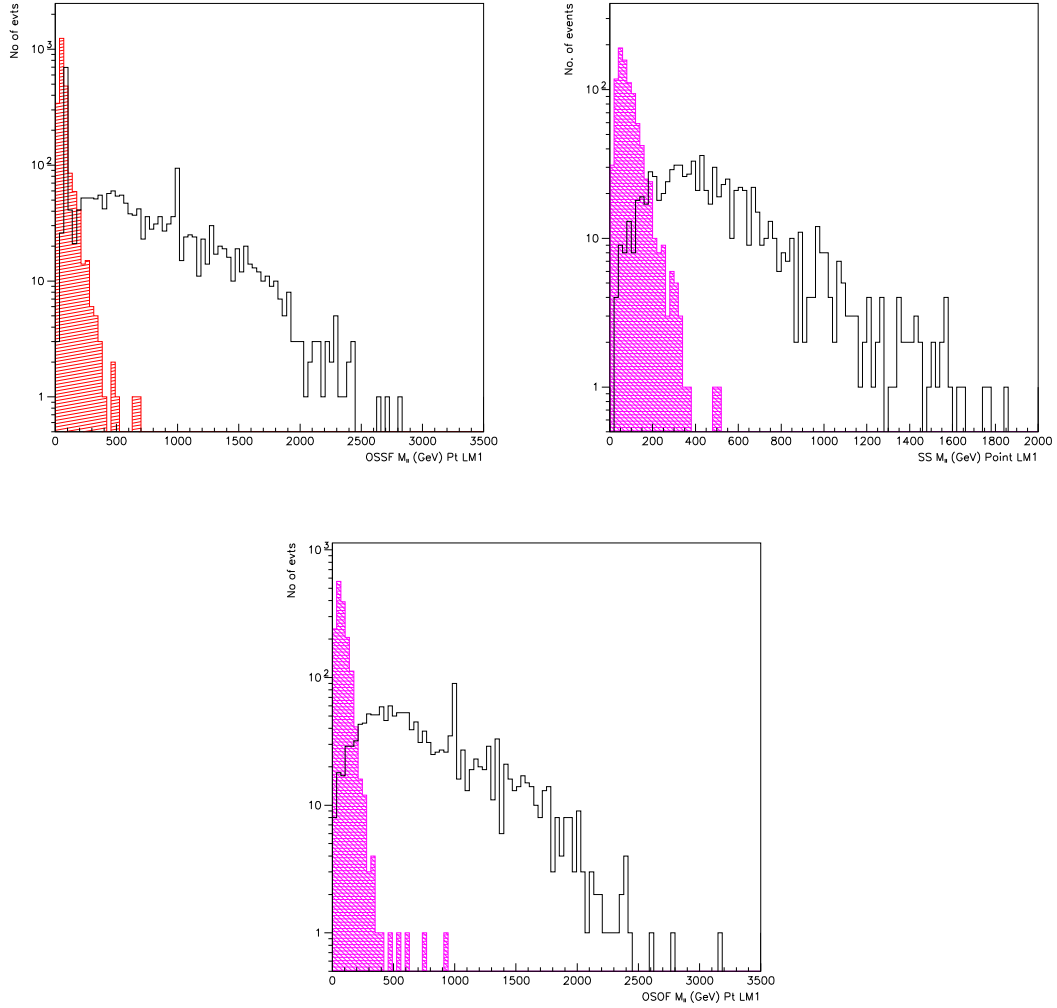


Figure 4.15: *Top Left Panel: Invariant mass distribution for SUSY and BH OSSF dilepton events for the CMS benchmark point LM1. Likewise to point A, the SUSY distribution shows the endpoint due to the presence of the LSP. Top Right Panel: invariant mass distribution for same sign dileptons. Bottom Panel: OSOF invariant mass distribution. A high value of $\tan\beta$ enhances the production of OSOF dileptons as explained in the text.*

4.2 ED and BH Event Analysis

In this section we present our original analysis of BH and graviton events at the LHC. Simulation results using energy, momentum and event shape variables as discriminators are first presented followed by an analysis of dileptons.

4.2.1 Energy, Momentum and Event shape variables

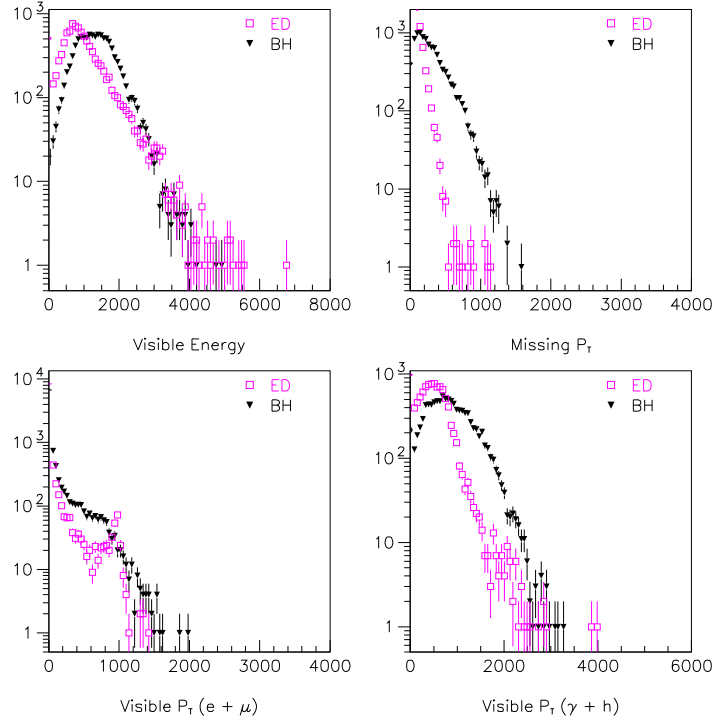


Figure 4.16: Comparison of 10,000 RS graviton and BH benchmark events. Visible energy and \cancel{P}_T (top panels) are comparable due to the presence of invisible channels in both models. Bottom panels show visible P_T due to leptons (left panel) and photons and hadrons (right panel).

Figure 4.16 shows visible energy, \cancel{P}_T and P_T of leptons and hadrons & photons for 10,000 RS graviton emission and BH benchmark events. The amount of visible energy is comparable for the two scenarios, even in the absence of a BH remnant. The \cancel{P}_T is due to the presence of neutrinos for the RS graviton model. Graviton decays are also capable of producing isolated leptons with high P_T . This explains the peak at 1 TeV in the visible P_T distribution of leptons. As with SUSY and BH, isolated leptons may provide a discriminating signature between BH and graviton decays (See Sect. 4.2.2).

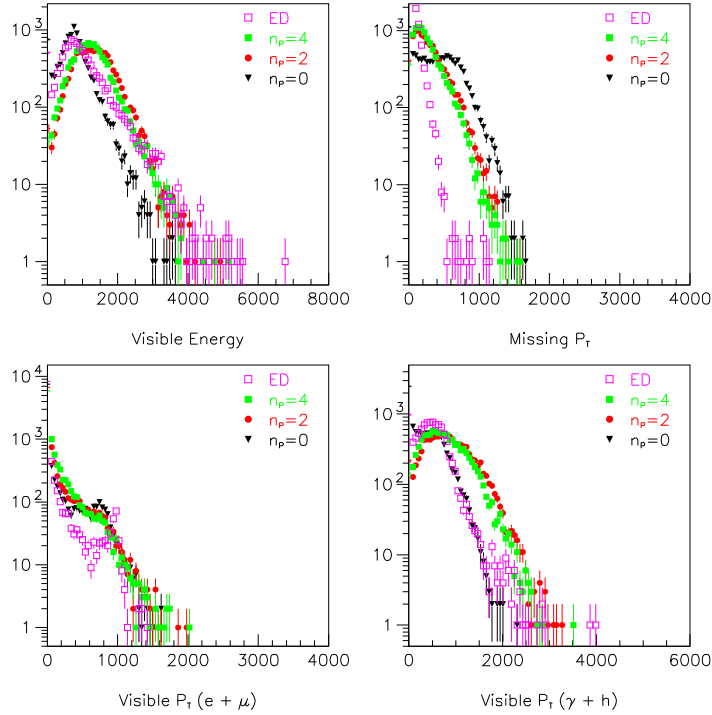


Figure 4.17: Distribution of visible energy, \cancel{P}_T and transverse momenta of leptons and hadrons & photons. RS graviton plots are shown as pink open squares. The four plots show the effect of different decay modes in the Planck phase of ten-dimensional BHs: remnant formation ($n_p = 0$, black filled triangles), two-body decay ($n_p = 2$, red filled circles) and four-body decay ($n_p = 4$, green filled squares). The fundamental Planck scale is $M_\star = 1$ TeV.

Fig. 4.17 compares BH events with zero-, two- and four-body final decay to graviton events. The variation of visible energy, \cancel{P}_T , and visible transverse momenta of leptons and hadrons & photons for different values of the fundamental Planck scale is shown in Fig. 4.18.

The above analysis is complemented by studying event shape variables. Graviton decays are dominated by jets. Formation of a BH remnant and high values of the fundamental scale lead to significant higher sphericity than graviton decays (top panels of Fig. 4.19). The 2nd Fox-Wolfram moment (middle panels of Fig. 4.19) is stable versus changes in the BH Planck phase and provides a good graviton/BH discriminator. BH models with higher M_\star can be differentiated more easily from events with graviton decays. Thrust (bottom panels of Fig. 4.19) conveys a similar information.

Similar conclusions can be reached by looking at jet the masses and at the number of jets. Graviton events generate more lighter jets than the BH model due to the mass of the graviton being lower than the mass of the BHs (Fig. 4.20). The difference is specially significant for high values of M_\star and in the

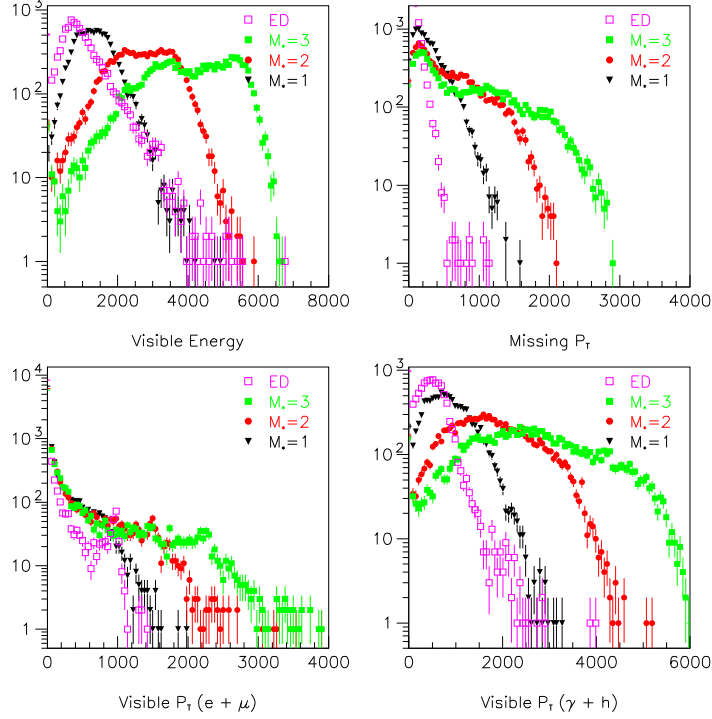


Figure 4.18: Distribution of visible energy, \cancel{P}_T and transverse momenta of leptons and hadrons & photons. RS graviton results are shown as pink open squares. The four plots show the effect of varying the fundamental Planck scale: $M_\star = 1$ TeV (black filled triangles), $M_\star = 2$ TeV (red filled circles) and $M_\star = 3$ TeV (green filled squares). The ten-dimensional BHs decay in two hard quanta at the end of the evaporation phase.

presence of BH remnants.

4.2.2 High- P_T leptons

Graviton decay into dileptons provides a cleaner signature. The ATLAS and CMS detectors are expected to detect gravitons with mass as high as 3.5 and 2.08 TeV for $c=0.1$ and 0.01, respectively [167, 168, 169]. The discovery reach is better with electrons than with muons because of a better energy resolution of electrons.

The SM background is removed by imposing the following cuts on leptons to remove the SM background: $P_{Tl} \geq 15$ GeV, $|\eta_l| < 2.5$, isolation cut $\sum_i P_{T_i} < 7$ GeV in a cone of $R = 0.2$ and $\cancel{P}_T \geq 100$ GeV where the symbols have their usual meanings.

In the RS scenario, the majority of high P_T leptons originate from the decay of the graviton and the Z^0 boson. The neutral graviton decays into a

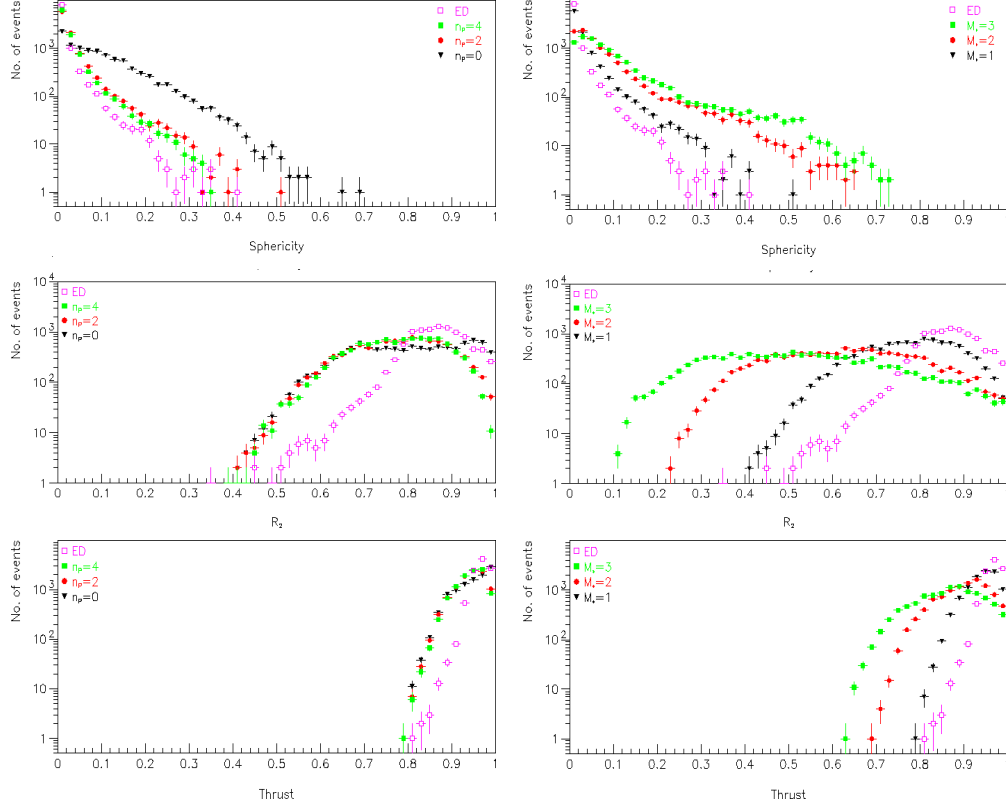


Figure 4.19: *Sphericity (top panels) and 2nd Fox-Wolfram moment (middle panels) and thrust (bottom panels) for 10,000 BH and graviton events (pink open squares). The left panels show the effect of different Planckian decay modes: BH remnant (black filled triangles), two-body decay (red filled circles) and four-body decay (green filled squares). The fundamental scale is $M_\star = 1$ TeV and the number of EDs is six. The right panels show the effect of different fundamental scales: $M_\star = 1$ TeV (black filled triangles), 2 TeV (red filled circles) and 3 TeV (green filled squares). Here, the ten-dimensional BHs decay in two quanta at the end of the Hawking phase.*

pair of OS dileptons with a OF-to-SF ratio of $\sim 1:14$. OSOF lepton pairs are originated either from the graviton decay into W bosons or from t quark pairs, where the top quark decays into leptons. Production of OSSF dileptons is less frequent in the BH model than in the RS graviton model. This is because of graviton decays in the Z^0 channel with the Z^0 decaying into leptons. Our analysis shows a 1:7 ratio of BH-to-ED dilepton events at fixed luminosity.

Figure 4.21 shows the dilepton invariant mass distribution for RS graviton production (shaded pink plot) and the BH model with final two-body decay. The RS graviton scenario is characterized by two peaks in the invariant mass distribution, at ~ 90 GeV and a second peak at 1 TeV. The first peak is due to dilepton events produced from the decay of Z^0 bosons. The second peak at ~ 1 TeV is due to graviton decay into a pair of leptons. The tail of the BH distribution is due to uncorrelated leptons from the decay phase. Since there

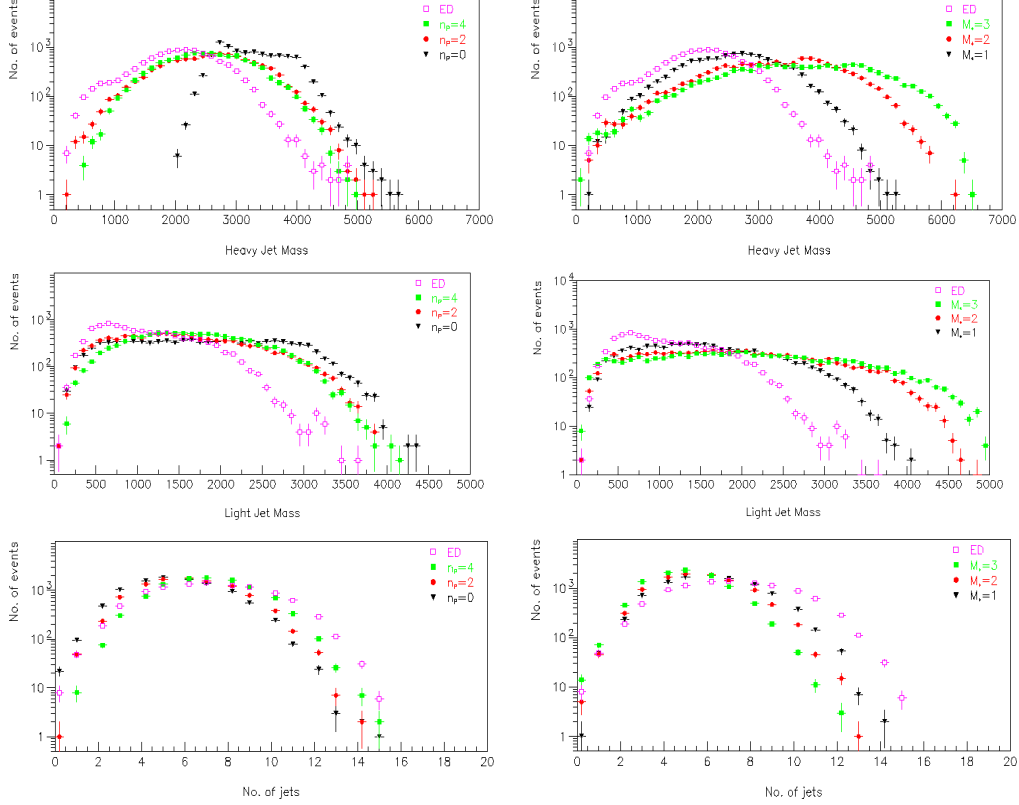


Figure 4.20: Heavy and light jet masses (top and middle panels) and number of jets (bottom panels) for 10,000 BH and graviton events. Symbols are like in previous figures.

is no similar process in the RS scenario to generate leptons, the invariant mass distribution of the graviton does not have a tail at high energies.

Table 4.3 shows the BR's of 1000 high- P_T isolated dileptons for the RS graviton model and the BH model. OSSF dileptons are dominant in both cases. However, due to the flavor conserving nature of the graviton decay, the number of SS dileptons produced in the RS scenario is virtually zero. This is not the case for BH events, where SS dileptons account for 18% of the total dileptons produced. Therefore, the SS dilepton invariant mass would be a promising discriminating signature for RS graviton events and BH events.

It is worthwhile to study the decay of the Z' boson which is predicted by many extensions of the SM [1, 170, 171]. The Z' boson is a heavy, (mass > 500 GeV) [1], colorless, neutral, spin 1 particle. As a result, Z' decay into leptons could compete with graviton decay in the same channel². This is especially significant for the LHC which could probe Z' masses in the TeV range. The observation of a TeV resonance in the dilepton and diphoton channels could

²However, the decay of Z' into photons is suppressed.

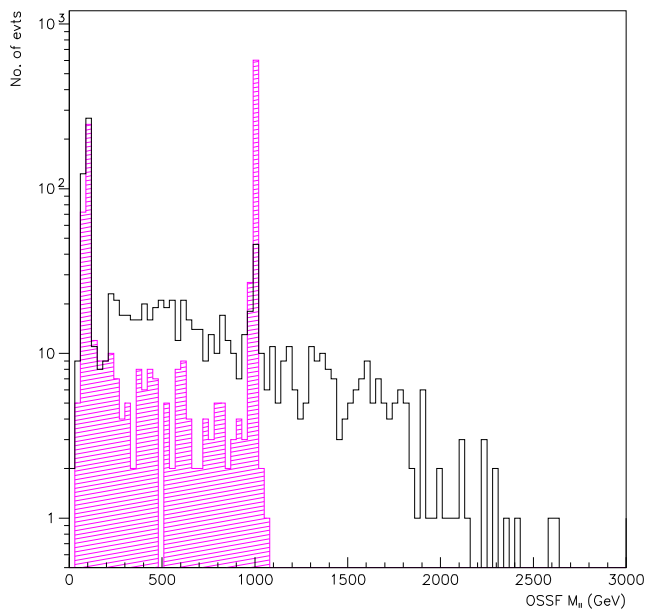


Figure 4.21: *Invariant mass distribution of 1100 OSOF dilepton events. Most high- P_T leptons in the RS model come from the decay of the graviton and Z^0 bosons. This is indicated by the two peaks in the invariant mass distribution. As discussed before in Sect. 4.1, the BH distribution is also characterized by two peaks. The discriminating signature is the high- P_T tail in the BH invariant mass distribution.*

provide a strong evidence of a RS graviton, distinguishing it from a Z' boson. An additional discriminating property between the graviton and the Z' is the angular distribution of the emitted particles, which is dependent on the spin of the resonance [171]. The angular distribution is strongly dependent on the production mechanism. The angular distributions of the G^* and Z' are shown in Table 4.4 [167] and the corresponding distributions are shown in Fig. 4.22. Gluon fusion predominates at the LHC. For graviton production, the quark-antiquark fusion contribution tends to flatten the angular distribution[168].

Table 4.3: BRs of high- P_T isolated dileptons for the RS and the BH models. Respectively 2.8×10^4 and 10^6 events were simulated in the two cases, yielding approximately 1000 dilepton events.

High P_T isolated dileptons	Graviton	%	BH	%
OSSF	987	99	523	50
OSOF	13	1	341	32
SS	0	0	190	18

Table 4.4: Angular distributions of Z' boson and graviton decay into dielectrons. θ is the angle between the beam direction and the electron in the rest frame of the resonance.

Process	Distribution
$gg \rightarrow G^* \rightarrow e^+e^-$	$1 - \cos^4 \theta$
$q\bar{q} \rightarrow G^* \rightarrow e^+e^-$	$1 - 3 \cos^2 \theta + 4 \cos^4 \theta$
$q\bar{q}, gg \rightarrow Z' \rightarrow e^+e^-$	$1 + \cos^2 \theta$

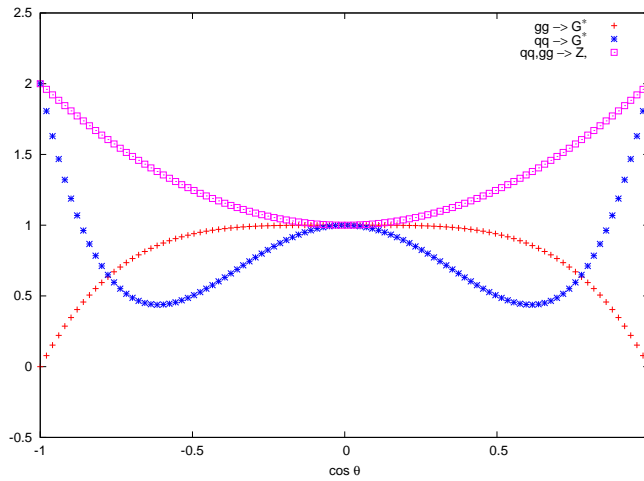


Figure 4.22: Angular distributions of electron from Z' and graviton decays.

4.3 SR and SM Event Analysis

Events with high- P_T photons are a powerful discriminator of SR events from the SM background. SR events are characterized by high values of visible energy and P_T as the photon and the jet originate directly from the 2×2 interaction. Isolated photons provide a further means to extract string signals: being directly produced from the SR, they are harder than SM photons. Analysis of event shape variables enhance the effectiveness of the above method. String simulations use the following benchmark: $M_s=1$ TeV and $P_{Tmin}=50$ GeV. Our analysis uses ~ 10000 and 200 string events for $M_s=1$ and 2 TeV produced from a sample run of 10^7 events at an integrated LHC luminosity of 1 fb^{-1} , respectively.

Figure 4.23 shows the visible energy (top panel) and the P_T of hadrons & photons (bottom panel) for 10 million string+SM and SM only events. The visible energy and the P_T are produced by the hard photons and the jets of the string decay. Their distributions are characterized by a long tail. The observation of events with P_T (visible energy) in excess of 3 (6) TeV would provide strong evidence of the existence of a SR.

In our analysis of the photon momentum, we select the hadronic jets according to the following criteria. The detector is assumed to have an absolute value of pseudorapidity of 2.6. This ensures that the jets are originated in the hard 2×2 scattering rather than in multiple interactions or from the beam remnants. The contribution of jets which do not originate in the hard scattering are minimized by fixing the minimum transverse energy of all particles comprising the jet ($\sum_i E_{T_i}$) to 40 GeV [172]. The particles of the jet must be within a cone of $R = \sqrt{(\Delta\eta^2 + \Delta\phi^2)} = 0.2$ from the jet initiator, where θ and ϕ are the azimuthal and polar angles of the particle w.r.t. the beam axis, respectively. Following Ref. [172], the cuts on the photon jets are $P_{T_\gamma} \geq 80$ GeV, $\eta < 2.6$ and an isolation cut $\sum_n P_T < 7$ GeV in a cone of $R = 0.4$.

The top panel of Fig. 4.24 shows the distribution of the highest P_{T_γ} of isolated photons for string+SM and SM only events. Single photons from SR are expected to have a higher P_{T_γ} than SM photons because they are the direct products of the string decay. The main source of background for direct photons are jet fluctuations and photons originating from the initial and final state radiation [172]. In the former case, a jet consists of a few particles including high- P_T π_0 's which decay into a pair of photons with a $\sim 99\%$ BR [172]. Due to the high boost, the photons have a relatively small angular separation and therefore “fake” a single photon in the electromagnetic calorimeter. The rate of this process is 1 out of $\sim 10^3$ to 10^4 events [172]. Other sources of fake photons are $H \rightarrow \gamma\gamma$ [173] or processes from other exotic phenomena, e.g. SUSY [174] or LEDs [88, 99, 100]. Isolation cuts on the photon can effectively reduce the number of fake photons.

The invariant mass plot of the two highest P_T jets for each event is shown

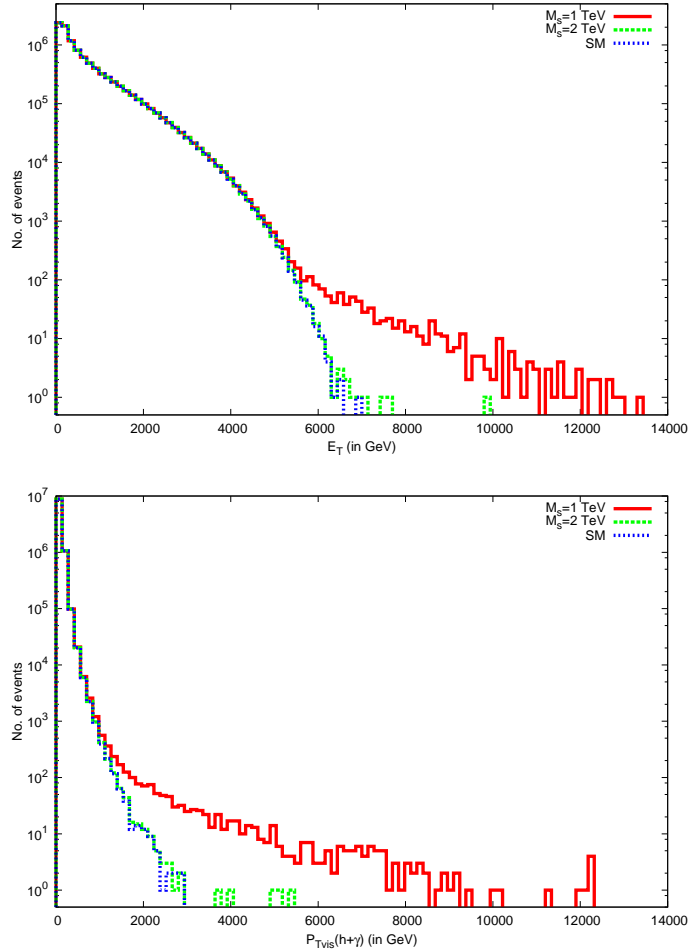


Figure 4.23: *Top panel: Visible energy distribution for string+SM and SM only events. The result for string events is shown by the solid red histogram ($M_s=1$ TeV) and the dashed green histogram ($M_s=2$ TeV). String events can be identified from the high- E_T tail for $M_s=1$ TeV. Bottom panel: Distribution of visible P_T for γ +hadrons. The high- P_T tail is a strong indicator of the presence of SR.*

in the bottom panel of Fig. 4.24. Due to the nature of the interaction under consideration, the bulk of the events for both string+SM and SM only events are comprised of dijets. These were selected using the same cuts as before. As is expected, the SM invariant mass distribution is negligible beyond a certain threshold (~ 4 TeV). This is due to the production of direct soft photons and jets from the SM interaction. The string+SM distribution is characterized by a long tail of energy up to several TeV (three times more than the SM). This tail is originated from the decay of string resonances into hard jets and photons. Therefore, the measure of a large invariant mass would provide strong evidence of a string mediated interaction.

Histograms for different event shape variables are shown in Fig. 4.25. String

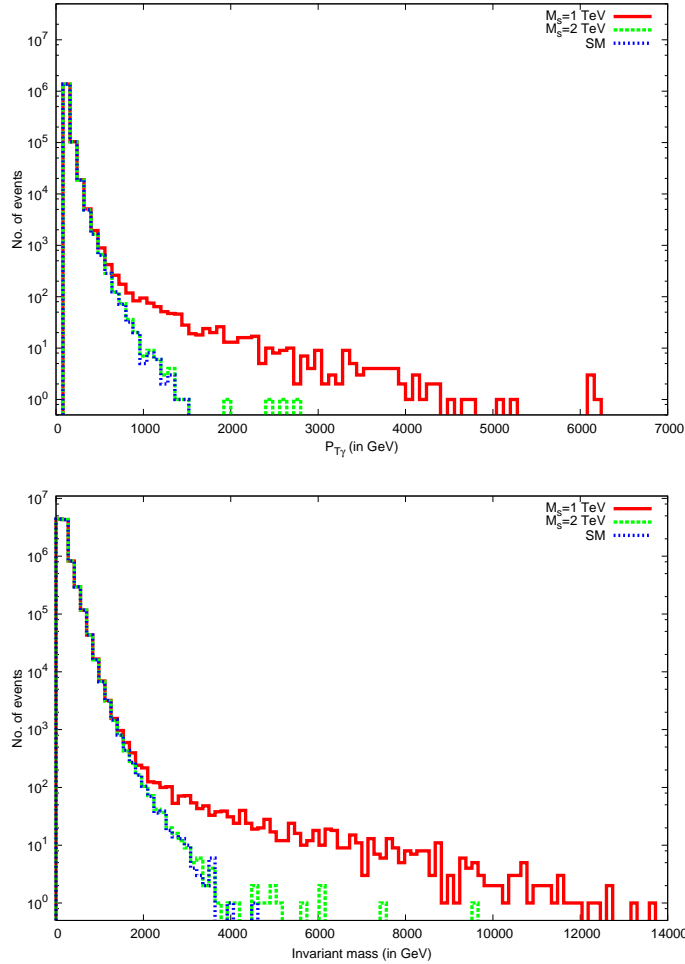


Figure 4.24: Top panel: Distribution of the highest $P_{T\gamma}$ for each event. γ 's with high P_T created in the string decay are the source of the long tail. Bottom panel: Dijet invariant mass distribution. String decays may result in large invariant mass.

events tend to be more spherical than the background: string+SM decays generally produce a distribution of high P_T jets at slightly higher values than the SM background. The jets originate from the decay of SRs into photons and hadrons. The SM generates less heavier jets than its string counterpart as shown in the middle and bottom panels of Fig. 4.25.

Before ending this section, let us briefly discuss the discovery reach of SRs at the LHC. Fig. 4.26 shows the signal-to-noise (SNR) ratio for two values of the integrated luminosity as a function of M_\star when $P_{Tmin}=50$ GeV. The instantaneous luminosity is assumed to be the LHC design luminosity of $10^{-34}cm^{-2}s^{-1}$ corresponding to an integrated luminosity of ~ 1300 (300) fb^{-1} in 4 (1) years. The SNR ratio for an integrated luminosity of $300 fb^{-1}$ is ~ 10 times less than the value obtained at $1300 fb^{-1}$. In an optimistic scenario, SRs at the TeV scale could be discovered after a successful year of running the

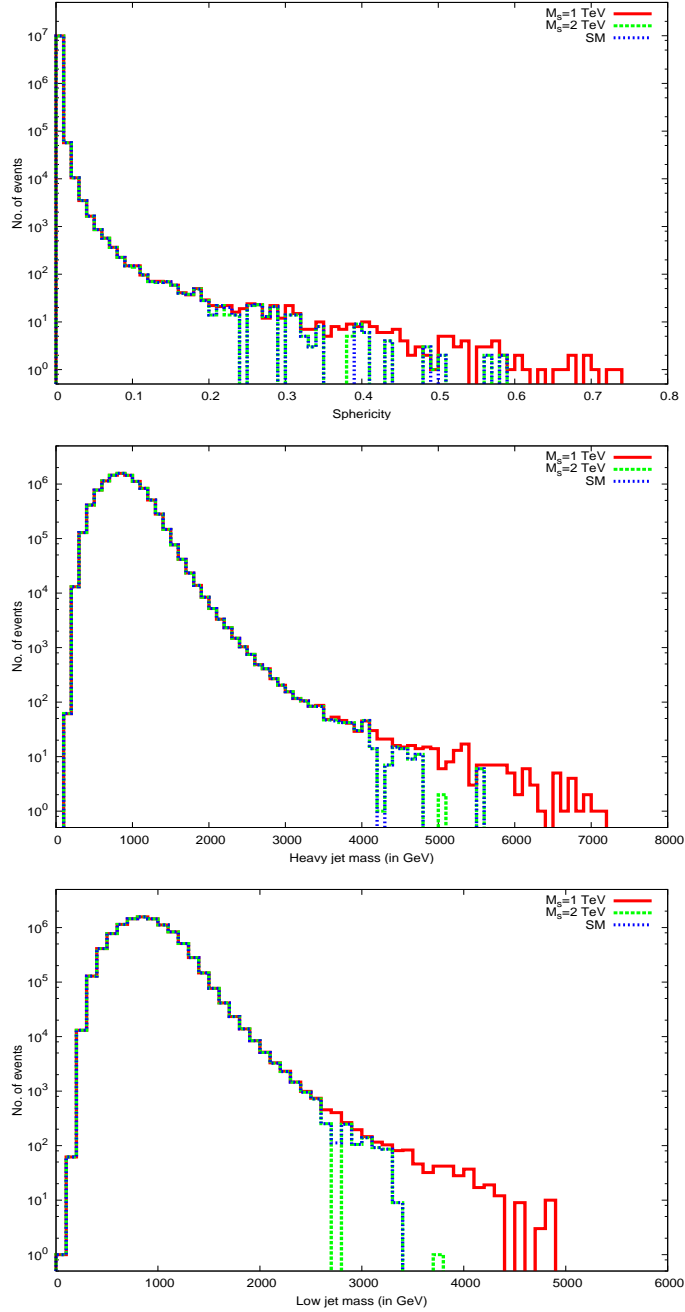


Figure 4.25: Histograms of event shape variables for 10 million string+SM and SM only events. String events are shown in solid red ($M_s=1$ TeV) and dashed green ($M_s=2$ TeV). SM events are shown in dotted blue. String events have on the average a slightly higher sphericity than SM events due to the slight increase in the number of jets (top panel). Similar conclusions are reached from the heavy and low jet mass distributions (middle and bottom panels, respectively).

LHC, assuming a signal-to noise ratio of 10.

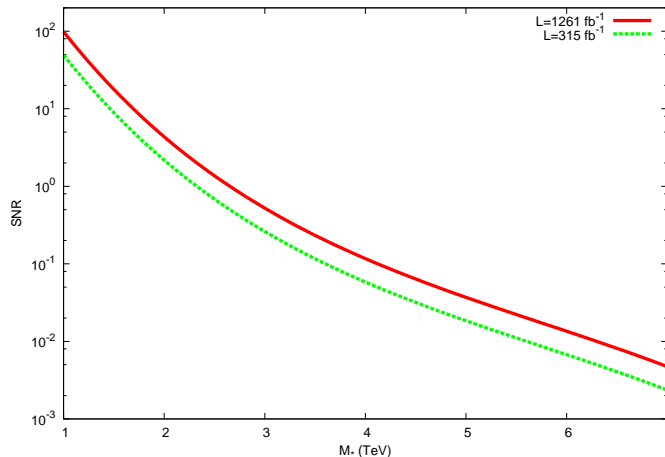


Figure 4.26: SNR for a integrated luminosity of 1300 fb^{-1} (solid red line) and 300 fb^{-1} (dashed green line), corresponding to 4 year and 1 year at an instantaneous luminosity of $10^{34} \text{ cm}^{-2} \text{ s}^{-1}$, respectively.

4.4 SR and BH Event Analysis

A powerful way of discriminating BH and string events would be searching for a Z^0 mass peak in the invariant mass of high- P_T leptons. Z^0 production is highly suppressed in case of string events [129]. On the contrary BH decay is characterized by the production of a variety of particles with high P_T . A rough counting of the number of degrees of freedom of these particles shows that the estimated rate of hadron-to-lepton production is 5:1 and the rate of Z^0 and γ production is comparable ($\sim 2\%$ to 3%) with the Z^0 bosons decaying into opposite-sign leptons with a 3.4% BR. The invariant mass distribution of BH events peaks at $\sim 92 \text{ GeV}$, confirming the production of a Z^0 boson [81]. Therefore, the presence of a peak at $\sim 92 \text{ GeV}$ in the invariant mass of leptons would effectively rule out formation of SRs in favor of BH production. Due to the nature of the Hawking radiation, BH events are also expected to have on average higher sphericity and a larger number of jets than string events. This is because in the $pp \rightarrow \gamma + jet$ channel string events are dominated by dijets, whereas BH decay produces multijets.

Conclusions

In this thesis we studied different scenarios for physics beyond the SM: SUSY, EDs and SRs.

Signatures of SUSY and TeV-scale BH events at the LHC have been discussed in Sect. 4.1. A combined analysis of event-shape variables and dilepton events has shown that it is possible to distinguish BHs and SUSY at the ATLAS and CMS detectors. Event shape variables alone cannot unequivocally discriminate between SUSY and BHs. For example, the thrust distribution for BH events with no remnant production is indistinguishable from the thrust distribution for SUSY events. However event shape variables may prove useful when combined with the analysis of the leptonic channel. Isolated dileptons could provide the “smoking gun” for detecting BHs at the LHC. The BH dilepton invariant mass shows a tail at high energy which is absent in the SM or MSSM. This analysis can be further strengthened by looking at the number and flavor of isolated leptons.

The possibility of discriminating BH and graviton events was discussed in Sect. 4.2. Our simulations showed that by analyzing the dilepton channel, BH and graviton events can be clearly discriminated at the LHC. As with SUSY and BHs, event shape variables provide additional means of discrimination.

Creation of SRs at the LHC was investigated in Sect. 4.3. If the string scale is ~ 1 TeV, our analysis has shown that SRs can be detected. With the LHC operating at a luminosity of $2 \times 10^{33} \text{ cm}^{-2} \text{ s}^{-1}$ SRs could be detected within a year of the start of the LHC. String events show higher sphericity and higher visible energy than the SM background. These quantities provide an effective means of detection when combined with the measure of the P_T of isolated photons and the dijet invariant mass. Since the final products of the SR are directly produced from the string decay, the dijet invariant mass is characterized by a tail at high energies which is absent in the SM. A powerful way of discriminating between BH and string events would be searching for a Z^0 mass peak in the invariant mass of high- P_T leptons. SR decay into leptons and photons may be another effective method for distinguishing SRs and BHs.

The investigations in this thesis provide a starting point for a quantitative study of discrimination of BHs from SUSY, graviton events and SRs at the LHC. However, many open questions remain unanswered. For

example, our work has not dealt in depth with sources of background at the LHC. The actual sensitivity of the method for specific experiments (CMS or ATLAS) is also not discussed here. Moreover, the kinematical cuts implemented in Chapter 4 although commonly used in the literature, lack a study at the generator level of their efficiency. Finally, it would also be worthwhile to study the detector response with CMSSW, the software framework which is used for simulation and analysis of high energy collisions at the CMS detector.

Bibliography

- [1] <http://pdg.lbl.gov>.
- [2] W. Greiner, S. Schramm, and E. Stein, “Quantum chromodynamics,” *Berlin, Germany: Springer (2002) 551 p* .
- [3] D. J. Gross and F. Wilczek, “Ultraviolet behavior of non-abelian gauge theories,” *Phys. Rev. Lett.* **30** (1973) 1343–1346.
- [4] D. J. Gross and F. Wilczek, “Asymptotically Free Gauge Theories 1,” *Phys. Rev.* **D8** (1973) 3633–3652.
- [5] D. J. Gross and F. Wilczek, “Asymptotically Free Gauge Theories 2,” *Phys. Rev.* **D9** (1974) 980–993.
- [6] B. C. Allanach *et al.*, “The Snowmass points and slopes: Benchmarks for SUSY searches,” *Eur. Phys. J.* **C25** (2002) 113–123, [arXiv:hep-ph/0202233](https://arxiv.org/abs/hep-ph/0202233).
- [7] F. E. Paige, S. D. Protopopescu, H. Baer, and X. Tata, “ISAJET 7.69: A Monte Carlo event generator for p p, anti-p p, and e+ e- reactions,” [arXiv:hep-ph/0312045](https://arxiv.org/abs/hep-ph/0312045).
- [8] “ATLAS detector and physics performance. Technical design report. Vol. 2,” *CERN-LHCC-95-15* . <http://atlas.web.cern.ch/Atlas/GROUPS/PHYSICS/TDR/access.html>.
- [9] **CMS and ATLAS** Collaboration, A. Drozdetskiy, “The standard model Higgs boson at LHC: Recent developments,” *CERN-CMS-CR-2007-022* . Prepared for 42nd Rencontres de Moriond on QCD and Hadronic Interactions, La Thuile, Italy, 17-24 Mar 2007.
- [10] D. Kcira, “Determination of the Discovery Potential for Higgs Bosons in MSSM,” [arXiv:0710.1957](https://arxiv.org/abs/0710.1957) [[hep-ex](https://arxiv.org/abs/hep-ex)].
- [11] **CMS** Collaboration, G. L. Bayatian *et al.*, “CMS technical design report, volume II: Physics performance,” *J. Phys.* **G34** (2007) 995–1579.

- [12] W. K. H. Panofsky, “The Evolution of Particle Accelerators & Colliders,” SLAC Beam Line, 27N1:36-44 1999.
www.slac.stanford.edu/pubs/beamline/27/1/27-1-panofsky.pdf.
- [13] K. R. Dienes, “String Theory and the Path to Unification: A Review of Recent Developments,” *Phys. Rept.* **287** (1997) 447–525,
[arXiv:hep-th/9602045](http://arxiv.org/abs/hep-th/9602045).
- [14] F. E. Paige, “Supersymmetry signatures at the CERN LHC,”
[arXiv:hep-ph/9801254](http://arxiv.org/abs/hep-ph/9801254).
- [15] K. R. Dienes, “New directions for new dimensions: An introduction to Kaluza-Klein theory, large extra dimensions, and the brane world,”. Prepared for Theoretical Advanced Study Institute in Elementary Particle Physics (TASI 2002): Particle Physics and Cosmology: The Quest for Physics Beyond the Standard Model(s), Boulder, Colorado, 2-28 Jun 2002.
- [16] M. Cavaglià, “Black hole and brane production in TeV gravity: A review,” *Int. J. Mod. Phys. A* **18** (2003) 1843–1882,
[arXiv:hep-ph/0210296](http://arxiv.org/abs/hep-ph/0210296).
- [17] C. Lefevre, “LHC: the guide (unpublished), Jan. 2008.”.
- [18] “The CERN website.” <http://www.cern.ch>.
- [19] T. Affolder, H. Akimoto, A. Akopian, M. G. Albrow, P. Amaral, D. Amidei, K. Anikeev, J. Antos, G. Apollinari, T. Arisawa, A. Artikov, T. Asakawa, W. Ashmanskas, F. Azfar, P. Azzi-Bacchetta, N. Bacchetta, H. Bachacou, S. Bailey, P. de Barbaro, A. Barbaro-Galtieri, V. E. Barnes, B. A. Barnett, S. Baroiant, M. Barone, G. Bauer, F. Bedeschi, and S. Belforte, “Charged jet evolution and the underlying event in proton-antiproton collisions at 1.8 tev,” *Phys. Rev. D* **65** (Apr, 2002) 092002.
- [20] M. Gell-Mann, “A schematic model of baryons and mesons,” *Physics Letters* **8** (1964) no. 3, 214 – 215.
- [21] V. E. Barnes *et al.*, “Observation of a Hyperon with Strangeness -3,” *Phys. Rev. Lett.* **12** (1964) 204–206.
- [22] G. Zweig, “An SU(3) model for strong interaction symmetry and its breaking,” *CERN-TH-401* .
- [23] G. Zweig, “An SU(3) model for strong interaction symmetry and its breaking. 2,” *CERN-TH-412* .

- [24] J. J. Sakurai, “Introduction to Electroweak Gauge Theory,”. Lectures presented at Int. Workshop on Neutral Current Interactions in Atoms, Cargese, France, Sep 10-14, 1979 UCLA-79-TEP-18.
- [25] C. Rubbia, P. McIntyre, and D. Cline, “Producing massive neutral intermediate vector bosons with existing accelerators,”. Presented at International Neutrino Conference, 8-12 Jun 1976, Aachen, Germany.
- [26] **UA2** Collaboration, M. Banner *et al.*, “Observation of single isolated electrons of high transverse momentum in events with missing transverse energy at the CERN anti-p p collider,” *Phys. Lett.* **B122** (1983) 476–485.
- [27] **UA2** Collaboration, P. Bagnaia *et al.*, “Evidence for Z^0 to $e^+ e^-$ at the CERN anti-p p collider,” *Phys. Lett.* **B129** (1983) 130–140.
- [28] **UA1** Collaboration, G. Arnison *et al.*, “Experimental observation of isolated large transverse energy electrons with associated missing energy at $s^{*1/2} = 540\text{-GeV}$,” *Phys. Lett.* **B122** (1983) 103–116.
- [29] **UA1** Collaboration, G. Arnison *et al.*, “Experimental observation of lepton pairs of invariant mass around $95\text{-GeV}/c^{*2}$ at the CERN SPS collider,” *Phys. Lett.* **B126** (1983) 398–410.
- [30] F. Englert and R. Brout, “Broken symmetry and the mass of gauge vector mesons,” *Phys. Rev. Lett.* **13** (1964) 321–322.
- [31] P. W. Higgs, “Broken symmetries and the masses of gauge bosons,” *Phys. Rev. Lett.* **13** (1964) 508–509.
- [32] E. . Appelquist, T., E. . Chodos, A., and E. . Freund, P. G. O. *Modern Kaluza-Klein Theories* . Reading, USA: Addison-Wesley (1987) 619 P. (Frontiers in Physics, 65).
- [33] S. P. Martin, “A Supersymmetry Primer,” [arXiv:hep-ph/9709356](https://arxiv.org/abs/hep-ph/9709356).
- [34] M. E. Peskin, “Supersymmetry in Elementary Particle Physics,” [arXiv:0801.1928](https://arxiv.org/abs/0801.1928) [hep-ph].
- [35] P. C. Argyres, S. Dimopoulos, and J. March-Russell, “Black holes and sub-millimeter dimensions,” *Phys. Lett.* **B441** (1998) 96–104, [arXiv:hep-th/9808138](https://arxiv.org/abs/hep-th/9808138).
- [36] T. Banks and W. Fischler, “A model for high energy scattering in quantum gravity,” [arXiv:hep-th/9906038](https://arxiv.org/abs/hep-th/9906038).
- [37] S. Dimopoulos and G. L. Landsberg, “Black Holes at the LHC,” *Phys. Rev. Lett.* **87** (2001) 161602, [arXiv:hep-ph/0106295](https://arxiv.org/abs/hep-ph/0106295).

- [38] S. B. Giddings and S. D. Thomas, “High energy colliders as black hole factories: The end of short distance physics,” *Phys. Rev.* **D65** (2002) 056010, [arXiv:hep-ph/0106219](#).
- [39] E.-J. Ahn, M. Cavaglià, and A. V. Olinto, “Brane factories,” *Phys. Lett.* **B551** (2003) 1–6, [arXiv:hep-th/0201042](#).
- [40] E.-J. Ahn and M. Cavaglià, “A new era in high-energy physics,” *Gen. Rel. Grav.* **34** (2002) 2037–2042, [arXiv:hep-ph/0205168](#).
- [41] V. P. Frolov and D. Stojkovic, “Black hole as a point radiator and recoil effect on the brane world,” *Phys. Rev. Lett* **89** (2002) 151302, [arXiv:hep-th/0208102](#).
- [42] V. P. Frolov and D. Stojkovic, “Black hole radiation in the brane world and recoil effect,” *Phys. Rev.* **D66** (2002) 084002, [arXiv:hep-th/0206046](#).
- [43] M. Cavaglià, S. Das, and R. Maartens, “Will we observe black holes at LHC?,” *Class. Quant. Grav.* **20** (2003) L205–L212, [arXiv:hep-ph/0305223](#).
- [44] A. Chamblin, F. Cooper, and G. C. Nayak, “Interaction of a TeV scale black hole with the quark gluon plasma at LHC,” *Phys. Rev.* **D69** (2004) 065010, [arXiv:hep-ph/0301239](#).
- [45] M. Cavaglià and S. Das, “How classical are TeV-scale black holes?,” *Class. Quant. Grav.* **21** (2004) 4511–4522, [arXiv:hep-th/0404050](#).
- [46] A. Chamblin, F. Cooper, and G. C. Nayak, “SUSY production from TeV scale blackhole at LHC,” *Phys. Rev.* **D70** (2004) 075018, [arXiv:hep-ph/0405054](#).
- [47] C. M. Harris *et al.*, “Exploring higher dimensional black holes at the large hadron collider,” *JHEP* **0505** (2005) 053, [arXiv:hep-ph/0411022](#).
- [48] J. Tanaka, T. Yamamura, S. Asai, and J. Kanzaki, “Study of black holes with the ATLAS detector at the LHC,” *Eur. Phys. J.* **C41** (2005) 19–33, [arXiv:hep-ph/0411095](#).
- [49] B. Webber, “Black holes at accelerators,” [arXiv:hep-ph/0511128](#).
- [50] L. Lonnblad, M. Sjordahl, and T. Akesson, “QCD-suppression by black hole production at the LHC,” *JHEP* **0509** (2005) 019, [arXiv:hep-ph/0505181](#).
- [51] J. L. Hewett, B. Lillie, and T. G. Rizzo, “Black holes in many dimensions at the LHC: Testing critical string theory,” *Phys. Rev. Lett.* **95** (2005) 261603, [arXiv:hep-ph/0503178](#).

- [52] G. C. Nayak and J. Smith, “Higgs boson production from black holes at the LHC,” *Phys. Rev.* **D74** (2006) 014007, [arXiv:hep-ph/0602129](#).
- [53] H. Stoecker, “Stable TeV - black hole remnants at the LHC: Discovery through di-jet suppression, mono-jet emission and a supersonic boom in the quark-gluon plasma,” *Int. J. Mod. Phys.* **D16** (2007) 185–205, [arXiv:hep-ph/0605062](#).
- [54] G. L. Alberghi *et al.*, “Probing quantum gravity effects in black holes at LHC,” [arXiv:hep-ph/0601243](#).
- [55] B. Koch, M. Bleicher, and H. Stoecker, “Black holes at LHC?,” *J. Phys.* **G34** (2007) S535–542, [arXiv:hep-ph/0702187](#).
- [56] J. L. Feng and A. D. Shapere, “Black hole production by cosmic rays,” *Phys. Rev. Lett.* **88** (2002) 021303, [arXiv:hep-ph/0109106](#).
- [57] A. Ringwald and H. Tu, “Collider versus cosmic ray sensitivity to black hole production,” *Phys. Lett.* **B525** (2002) 135–142, [arXiv:hep-ph/0111042](#).
- [58] L. A. Anchordoqui, J. L. Feng, H. Goldberg, and A. D. Shapere, “Black holes from cosmic rays: Probes of extra dimensions and new limits on TeV-scale gravity,” *Phys. Rev.* **D65** (2002) 124027, [arXiv:hep-ph/0112247](#).
- [59] E.-J. Ahn, M. Ave, M. Cavaglià, and A. V. Olinto, “TeV black hole fragmentation and detectability in extensive air-showers,” *Phys. Rev.* **D68** (2003) 043004, [arXiv:hep-ph/0306008](#).
- [60] J. I. Illana, M. Masip, and D. Meloni, “TeV gravity at neutrino telescopes,” *Phys. Rev.* **D72** (2005) 024003, [arXiv:hep-ph/0504234](#).
- [61] V. Cardoso, M. C. Espirito Santo, M. Paulos, M. Pimenta, and B. Tome, “Microscopic black hole detection in UHECR: The double bang signature,” *Astropart. Phys.* **22** (2005) 399–407, [arXiv:hep-ph/0405056](#).
- [62] **ATIC-1** Collaboration, H. S. Ahn *et al.*, “ATIC experiment: Elemental spectra from the flight in 2000,”. Prepared for 28th International Cosmic Ray Conferences (ICRC 2003), Tsukuba, Japan, 31 Jul - 7 Aug 2003.
- [63] A. Cafarella, C. Coriano, and T. N. Tomaras, “Cosmic ray signals from mini black holes in models with extra dimensions: An analytical / Monte Carlo study,” *JHEP* **0506** (2005) 065, [arXiv:hep-ph/0410358](#).

- [64] E.-J. Ahn and M. Cavaglià, “Simulations of black hole air showers in cosmic ray detectors,” *Phys. Rev.* **D73** (2006) 042002, [arXiv:hep-ph/0511159](#).
- [65] M. Cavaglià and A. Roy, “QCD and spin effects in black hole airshowers,” *Phys. Rev.* **D76** (2007) 044005, [arXiv:0707.0274 \[hep-ph\]](#).
- [66] R. Casadio, S. Fabi, and B. Harms, “On the Possibility of Catastrophic Black Hole Growth in the Warped Brane-World Scenario at the LHC,” [arXiv:0901.2948 \[hep-ph\]](#).
- [67] R. Emparan, “Black hole production at a TeV,” [arXiv:hep-ph/0302226](#).
- [68] S. Hossenfelder, “What black holes can teach us,” [arXiv:hep-ph/0412265](#).
- [69] P. Kanti, “Black holes in theories with large extra dimensions: A Review,” *Int. J. Mod. Phys.* **A19** (2004) 4899–4951, [arXiv:hep-ph/0402168](#).
- [70] G. L. Landsberg, “Black Holes at Future Colliders and Beyond,” *J. Phys.* **G32** (2006) R337–R365, [arXiv:hep-ph/0607297](#).
- [71] G. F. Giudice, R. Rattazzi, and J. D. Wells, “Quantum gravity and extra dimensions at high-energy colliders,” *Nucl. Phys.* **B544** (1999) 3–38, [arXiv:hep-ph/9811291](#).
- [72] E. A. Mirabelli, M. Perelstein, and M. E. Peskin, “Collider signatures of new large space dimensions,” *Phys. Rev. Lett.* **82** (1999) 2236–2239, [arXiv:hep-ph/9811337](#).
- [73] S. Cullen and M. Perelstein, “SN1987A constraints on large compact dimensions,” *Phys. Rev. Lett.* **83** (1999) 268–271, [arXiv:hep-ph/9903422](#).
- [74] **TeV4LHC Working Group** Collaboration, S. Abdullin *et al.*, “Tevatron-for-LHC Report: Preparations for Discoveries,” [arXiv:hep-ph/0608322](#).
- [75] T. G. Rizzo, “Probes of universal extra dimensions at colliders,” *Phys. Rev.* **D64** (2001) 095010, [arXiv:hep-ph/0106336](#).
- [76] C. Macesanu, C. D. McMullen, and S. Nandi, “Collider implications of universal extra dimensions,” *Phys. Rev.* **D66** (2002) 015009, [arXiv:hep-ph/0201300](#).

- [77] A. Datta, K. Kong, and K. T. Matchev, “Discrimination of supersymmetry and universal extra dimensions at hadron colliders,” *Phys. Rev.* **D72** (2005) 096006, [arXiv:hep-ph/0509246](#).
- [78] M. Battaglia, A. K. Datta, A. De Roeck, K. Kong, and K. T. Matchev, “Contrasting supersymmetry and universal extra dimensions at colliders,” [arXiv:hep-ph/0507284](#).
- [79] M. Battaglia, A. Datta, A. De Roeck, K. Kong, and K. T. Matchev, “Contrasting supersymmetry and universal extra dimensions at the CLIC multi-TeV e+ e- collider,” *JHEP* **0507** (2005) 033, [arXiv:hep-ph/0502041](#).
- [80] P. Konar and P. Roy, “Event shape discrimination of supersymmetry from large extra dimensions at a linear collider,” *Phys. Lett.* **B634** (2006) 295–301, [arXiv:hep-ph/0509161](#).
- [81] A. Roy and M. Cavaglià, “Discriminating Supersymmetry and Black Holes at the Large Hadron Collider,” *Phys. Rev.* **D77** (2008) 064029, [arXiv:0801.3281 \[hep-ph\]](#).
- [82] A. Roy and M. Cavaglià, “Supersymmetry versus black holes at the LHC,” *Mod. Phys. Lett.* **A23** (2008) 2987–2996, [arXiv:0710.5490 \[hep-ph\]](#).
- [83] A. Roy and M. Cavaglià, “String resonances at the Large Hadron Collider,” [arXiv:0902.1473 \[hep-ph\]](#).
- [84] J. F. Donoghue, E. Golowich, and B. R. Holstein, “Dynamics of the standard model,” *Camb. Monogr. Part. Phys. Nucl. Phys. Cosmol.* **2** (1992) 1–540.
- [85] R. N. Mohapatra, “Beyond the standard model,” *Prog. Part. Nucl. Phys.* **26** (1991) 1–89.
- [86] B. C. Allanach *et al.*, “Les Houches ‘Physics at TeV colliders 2005’ Beyond the standard model working group: Summary report 2005,” [arXiv:hep-ph/0602198](#).
- [87] Tevatron New Phenomena and Higgs working group for the CDF and DZero collaboration, “Combined CDF and DZero Upper Limits on Standard Model Higgs-Boson Production with up to 4.2 fb⁻¹ of Data,” [arXiv:0903.4001 \[hep-ex\]](#).
- [88] N. Arkani-Hamed, S. Dimopoulos, and G. R. Dvali, “The hierarchy problem and new dimensions at a millimeter,” *Phys. Lett.* **B429** (1998) 263–272, [arXiv:hep-ph/9803315](#).

- [89] L. Randall and R. Sundrum, “An alternative to compactification,” *Phys. Rev. Lett.* **83** (1999) 4690–4693, [arXiv:hep-th/9906064](#).
- [90] M. Schmaltz, “Physics beyond the standard model (theory): Introducing the little higgs,” *Nuclear Physics B - Proceedings Supplements* **117** (2003) 40 – 49. 31st International Conferences on High Energy Physics.
- [91] G. L. Kane, “Modern Elementary Particle Physics,”. Redwood City, USA: Addison-Wesley (1987) 344 P. (The Advanced Book Program).
- [92] J. R. Ellis, G. Ridolfi, and F. Zwirner, “Higgs boson properties in the standard model and its supersymmetric extensions,” *Comptes Rendus Physique* **8** (2007) 999–1012, [arXiv:hep-ph/0702114](#).
- [93] J. Wess and B. Zumino, “A Lagrangian Model Invariant Under Supergauge Transformations,” *Phys. Lett.* **B49** (1974) 52.
- [94] S. Weinberg, “The quantum theory of fields. Vol. 3: Supersymmetry,”. Cambridge, UK: Univ. Pr. (2000) 419 p.
- [95] E. Richter-Was *et al.*, “Minimal supersymmetric standard model Higgs rates and backgrounds in ATLAS,” *Int. J. Mod. Phys. A* **13** (1998) 1371–1494.
- [96] A. Bartl *et al.*, “Supersymmetry at LHC,”. Presented at 1996 DPF / DPB Summer Study on New Directions for High-Energy Physics (Snowmass 96), Snowmass, CO, 25 Jun - 12 Jul 1996 LBL-39413.
- [97] M. Dittmar, “SUSY discovery strategies at the LHC,” [arXiv:hep-ex/9901004](#).
- [98] L. S. Stark, P. Hafliger, A. Biland, and F. Pauss, “New allowed mSUGRA parameter space from variations of the trilinear scalar coupling A_0 ,” *JHEP* **0508** (2005) 059, [arXiv:hep-ph/0502197](#).
- [99] I. Antoniadis, N. Arkani-Hamed, S. Dimopoulos, and G. R. Dvali, “New dimensions at a millimeter to a Fermi and superstrings at a TeV,” *Phys. Lett.* **B436** (1998) 257–263, [arXiv:hep-ph/9804398](#).
- [100] N. Arkani-Hamed, S. Dimopoulos, and G. R. Dvali, “Phenomenology, astrophysics and cosmology of theories with sub-millimeter dimensions and TeV scale quantum gravity,” *Phys. Rev.* **D59** (1999) 086004, [arXiv:hep-ph/9807344](#).
- [101] L. Randall and R. Sundrum, “A large mass hierarchy from a small extra dimension,” *Phys. Rev. Lett.* **83** (1999) 3370–3373, [arXiv:hep-ph/9905221](#).

- [102] T. Appelquist, H.-C. Cheng, and B. A. Dobrescu, “Bounds on universal extra dimensions,” *Phys. Rev.* **D64** (2001) 035002, [arXiv:hep-ph/0012100](#).
- [103] J. A. R. Cembranos, J. L. Feng, and L. E. Strigari, “Exotic collider signals from the complete phase diagram of minimal universal extra dimensions,” *Phys. Rev.* **D75** (2007) 036004, [arXiv:hep-ph/0612157](#).
- [104] J. Polchinski, “String theory. Vol. 1: An introduction to the bosonic string,”. Cambridge, UK: Univ. Pr. (1998) 402 p.
- [105] J. Polchinski, “String theory. Vol. 2: Superstring theory and beyond,”. Cambridge, UK: Univ. Pr. (1998) 531 p.
- [106] B. Zwiebach, “A first course in string theory,”. Cambridge, UK: Univ. Pr. (2004) 558 p.
- [107] C. M. Harris, “Physics beyond the standard model: Exotic leptons and black holes at future colliders,” [arXiv:hep-ph/0502005](#).
- [108] O. J. P. Eboli, T. Han, M. B. Magro, and P. G. Mercadante, “Diphoton signals for large extra dimensions at the Tevatron and CERN LHC,” *Phys. Rev.* **D61** (2000) 094007, [arXiv:hep-ph/9908358](#).
- [109] D. J. Kapner *et al.*, “Tests of the gravitational inverse-square law below the dark-energy length scale,” *Phys. Rev. Lett.* **98** (2007) 021101, [arXiv:hep-ph/0611184](#).
- [110] S. Ask, “Search for extra dimensions at LEP,” [arXiv:hep-ex/0410004](#).
- [111] H. Davoudiasl, J. L. Hewett, and T. G. Rizzo, “Phenomenology of the Randall-Sundrum Gauge Hierarchy Model,” *Phys. Rev. Lett.* **84** (2000) 2080, [arXiv:hep-ph/9909255](#).
- [112] K. Cheung, “Black hole, string ball, and p-brane production at hadronic supercolliders,” *Phys. Rev. D*, .
- [113] S. Dimopoulos and R. Emparan, “String balls at the LHC and beyond,” *Phys. Lett.* **B526** (2002) 393–398, [arXiv:hep-ph/0108060](#).
- [114] P. Jain, S. Kar, and S. Panda, “Brane-production and the neutrino nucleon cross section at ultra high energies in low scale gravity models,” *Int. J. Mod. Phys.* **D12** (2003) 1593–1602, [arXiv:hep-ph/0201232](#).
- [115] L. A. Anchordoqui, J. L. Feng, and H. Goldberg, “p-Branes and the GZK paradox,” *Physics Letters B* **535** (2002) no. 1-4, 302 – 308.
- [116] K. Thorne, “Magic without magic: John Archibald Wheeler,”. edited by J. Klauder (Freeman, San Francisco, 1972).).

- [117] V. Cardoso, E. Berti, and M. Cavaglià, “What we (don’t) know about black hole formation in high- energy collisions,” *Class. Quant. Grav.* **22** (2005) L61–R84, [arXiv:hep-ph/0505125](#).
- [118] P. C. Aichelburg and R. U. Sexl, “On the Gravitational field of a massless particle,” *Gen. Rel. Grav.* **2** (1971) 303–312.
- [119] H. Yoshino and Y. Nambu, “Black hole formation in the grazing collision of high- energy particles,” *Phys. Rev.* **D67** (2003) 024009, [arXiv:gr-qc/0209003](#).
- [120] H. Yoshino and V. S. Rychkov, “Improved analysis of black hole formation in high-energy particle collisions,” *Phys. Rev.* **D71** (2005) 104028, [arXiv:hep-th/0503171](#).
- [121] E. Berti, M. Cavaglià, and L. Gualtieri, “Gravitational energy loss in high energy particle collisions: Ultra-relativistic plunge into a multidimensional black hole,” *Phys. Rev.* **D69** (2004) 124011, [arXiv:hep-th/0309203](#).
- [122] L. A. Anchordoqui, J. L. Feng, H. Goldberg, and A. D. Shapere, “Updated limits on TeV-scale gravity from absence of neutrino cosmic ray showers mediated by black holes,” *Phys. Rev.* **D68** (2003) 104025, [arXiv:hep-ph/0307228](#).
- [123] S. W. Hawking, “Particle Creation by Black Holes,” *Commun. Math. Phys.* **43** (1975) 199–220.
- [124] R. Emparan, G. T. Horowitz, and R. C. Myers, “Black holes radiate mainly on the brane,” *Phys. Rev. Lett.* **85** (2000) 499–502, [arXiv:hep-th/0003118](#).
- [125] M. Cavaglià, “Black hole multiplicity at particle colliders (Do black holes radiate mainly on the brane?),” *Phys. Lett.* **B569** (2003) 7–13, [arXiv:hep-ph/0305256](#).
- [126] V. Cardoso, M. Cavaglià, and L. Gualtieri, “Hawking emission of gravitons in higher dimensions: Non- rotating black holes,” *JHEP* **0602** (2006) 021, [arXiv:hep-th/0512116](#).
- [127] V. Cardoso, M. Cavaglià, and L. Gualtieri, “Black hole particle emission in higher-dimensional spacetimes,” *Phys. Rev. Lett.* **96** (2006) 071301, [arXiv:hep-th/0512002](#).
- [128] P. Burikham, T. Figy, and T. Han, “TeV-scale string resonances at hadron colliders,” *Phys. Rev.* **D71** (2005) 016005, [arXiv:hep-ph/0411094](#).

- [129] L. A. Anchordoqui, H. Goldberg, S. Nawata, and T. R. Taylor, “Direct photons as probes of low mass strings at the LHC,” *Phys. Rev.* **D78** (2008) 016005, [arXiv:0804.2013 \[hep-ph\]](#).
- [130] L. A. Anchordoqui *et al.*, “Dijet signals for low mass strings at the LHC,” *Phys. Rev. Lett.* **101** (2008) 241803, [arXiv:0808.0497 \[hep-ph\]](#).
- [131] S. Cullen, M. Perelstein, and M. E. Peskin, “TeV strings and collider probes of large extra dimensions,” *Phys. Rev.* **D62** (2000) 055012, [arXiv:hep-ph/0001166](#).
- [132] F. Cornet, J. I. Illana, and M. Masip, “TeV strings and the neutrino nucleon cross section at ultra-high energies,” *Phys. Rev. Lett.* **86** (2001) 4235–4238, [arXiv:hep-ph/0102065](#).
- [133] J. J. Friess, T. Han, and D. Hooper, “TeV string state excitation via high energy cosmic neutrinos,” *Phys. Lett.* **B547** (2002) 31–36, [arXiv:hep-ph/0204112](#).
- [134] P. Burikham, T. Han, F. Hussain, and D. W. McKay, “Bounds on four fermion contact interactions induced by string resonances,” *Phys. Rev.* **D69** (2004) 095001, [arXiv:hep-ph/0309132](#).
- [135] J. Pumplin *et al.*, “New generation of parton distributions with uncertainties from global QCD analysis,” *JHEP* **0207** (2002) 012, [arXiv:hep-ph/0201195](#).
- [136] **ATLAS** Collaboration, W. W. Armstrong *et al.*, “ATLAS: Technical proposal for a general-purpose p p experiment at the Large Hadron Collider at CERN,”. CERN-LHCC-94-43.
- [137] “CMS, the Compact Muon Solenoid: Technical proposal,”. CERN-LHCC-94-38.
- [138] P. W. Higgs, “Broken symmetries, massless particles and gauge fields,” *Phys. Lett.* **12** (1964) 132–133.
- [139] G. S. Guralnik, C. R. Hagen, and T. W. B. Kibble, “Global conservation laws and massless particles,” *Phys. Rev. Lett.* **13** (1964) 585–587.
- [140] P. W. Higgs, “Spontaneous Symmetry Breakdown without Massless Bosons,” *Phys. Rev.* **145** (1966) 1156–1163.
- [141] A. Djouadi, “The Anatomy of electroweak symmetry breaking. I: The Higgs boson in the standard model,” *Phys. Rept.* **457** (2008) 1–216, [arXiv:hep-ph/0503172](#).

- [142] H. Baer, C.-h. Chen, F. Paige, and X. Tata, “Signals for minimal supergravity at the CERN large hadron collider: Multi - jet plus missing energy channel,” *Phys. Rev.* **D52** (1995) 2746–2759, [arXiv:hep-ph/9503271](#).
- [143] H. Baer, C.-h. Chen, F. Paige, and X. Tata, “Signals for Minimal Supergravity at the CERN Large Hadron Collider II: Multilepton Channels,” *Phys. Rev.* **D53** (1996) 6241–6264, [arXiv:hep-ph/9512383](#).
- [144] T. Sjostrand, S. Mrenna, and P. Skands, “PYTHIA 6.4 Physics and Manual,” *JHEP* **0605** (2006) 026, [arXiv:hep-ph/0603175](#).
- [145] <http://projects.hepforge.org/pythia6>.
- [146] M. Cavaglià, R. Godang, L. Cremaldi, and D. Summers, “Catfish: A Monte Carlo simulator for black holes at the LHC,” *Comput. Phys. Commun.* **177** (2007) 506–517, [arXiv:hep-ph/0609001](#).
- [147] M. Cavaglià, R. Godang, L. M. Cremaldi, and D. J. Summers, “Signatures of black holes at the LHC,” *JHEP* **0706** (2007) 055, [arXiv:0707.0317](#) [[hep-ph](#)].
- [148] D. M. Gingrich, “Missing energy in black hole production and decay at the Large Hadron Collider,” *JHEP* **0711** (2007) 064, [arXiv:0706.0623](#) [[hep-ph](#)].
- [149] I. Hinchliffe, F. E. Paige, M. D. Shapiro, J. Soderqvist, and W. Yao, “Precision SUSY measurements at CERN LHC,” *Phys. Rev.* **D55** (1997) 5520–5540, [arXiv:hep-ph/9610544](#).
- [150] B. Koch, M. Bleicher, and S. Hossenfelder, “Black hole remnants at the LHC,” *JHEP* **0510** (2005) 053, [arXiv:hep-ph/0507138](#).
- [151] P. Meade and L. Randall, “Black Holes and Quantum Gravity at the LHC,” *JHEP* **0805** (2008) 003, [arXiv:0708.3017](#) [[hep-ph](#)].
- [152] P. Kanti and J. March-Russell, “Calculable corrections to brane black hole decay. I: The scalar case,” *Phys. Rev.* **D66** (2002) 024023, [arXiv:hep-ph/0203223](#).
- [153] P. Kanti and J. March-Russell, “Calculable corrections to brane black hole decay. II: Greybody factors for spin 1/2 and 1,” *Phys. Rev.* **D67** (2003) 104019, [arXiv:hep-ph/0212199](#).
- [154] C. M. Harris and P. Kanti, “Hawking radiation from a (4+n)-dimensional black hole: Exact results for the Schwarzschild phase,” *JHEP* **0310** (2003) 014, [arXiv:hep-ph/0309054](#).

- [155] D. Ida, K.-y. Oda, and S. C. Park, “Rotating black holes at future colliders: Greybody factors for brane fields,” *Phys. Rev.* **D67** (2003) 064025, [arXiv:hep-th/0212108](#).
- [156] A. S. Cornell, W. Naylor, and M. Sasaki, “Graviton emission from a higher-dimensional black hole,” *JHEP* **0602** (2006) 012, [arXiv:hep-th/0510009](#).
- [157] G. Polesello, L. Poggioli, E. Richter-Was, and J. Soderqvist, “Precision SUSY measurements with ATLAS for SUGRA point 5,”. ATLAS Internal Note, PHYS-No-111, October 1997.
- [158] H. Baer, C.-h. Chen, M. Drees, F. Paige, and X. Tata, “Probing minimal supergravity at the CERN LHC for large $\tan(\beta)$,” *Phys. Rev.* **D59** (1999) 055014, [arXiv:hep-ph/9809223](#).
- [159] D. Denegri, W. Majerotto, and L. Rurua, “Constraining the minimal supergravity model parameter $\tan(\beta)$ by measuring the dilepton mass distribution at LHC,” *Phys. Rev.* **D60** (1999) 035008, [arXiv:hep-ph/9901231](#).
- [160] Y. Andreev, N. Krasnikov, and A. Toropin, “Using the $e^\pm\mu^\mp + E_T^{miss}$ and $l^+l^- + E_T^{miss}$ Signatures in the Search for Supersymmetry and Constraining the MSSM model at LHC,” [arXiv:0706.2578 \[hep-ph\]](#).
- [161] S. Abdullin and F. Charles, “Search for SUSY in (leptons +) jets + E(T)(miss) final states,” *Nucl. Phys.* **B547** (1999) 60–80, [arXiv:hep-ph/9811402](#).
- [162] M. Chiorboli, M. Galanti, and A. Tricomi, “SUSY searches with opposite sign dileptons at CMS,” *Acta Phys. Polon.* **B38** (2007) 559–566.
- [163] **D0** Collaboration, B. Abbott *et al.*, “Measurement of the top quark mass using dilepton events. DØ Collaboration,” *Phys. Rev. Lett.* **80** (1998) 2063–2068, [arXiv:hep-ex/9706014](#).
- [164] H. Baer, X. Tata, and J. Woodside, “Gluino cascade decay signatures at the Tevatron collider,” *Phys. Rev.* **D41** (1990) 906.
- [165] H. Baer, X. Tata, and J. Woodside, “Multi - lepton signals from supersymmetry at hadron super colliders,” *Phys. Rev.* **D45** (1992) 142–160.
- [166] H. Baer *et al.*, “Low-energy supersymmetry phenomenology,” [arXiv:hep-ph/9503479](#).

- [167] B. C. Allanach, K. Odagiri, M. A. Parker, and B. R. Webber, “Searching for narrow graviton resonances with the ATLAS detector at the Large Hadron Collider,” *JHEP* **0009** (2000) 019, [arXiv:hep-ph/0006114](#).
- [168] B. C. Allanach *et al.*, “Exploring small extra dimensions at the large hadron collider,” *JHEP* **0212** (2002) 039, [arXiv:hep-ph/0211205](#).
- [169] C. Collard, M. C. Lemaire, P. Traczyk and G. Wrochna, “Prospects for Study of Randall-Sundrum Gravitons in the CMS Experiment, CMS-NOTE-2002-050,”.
- [170] A. Leike, “The Phenomenology of extra neutral gauge bosons,” *Phys. Rept.* **317** (1999) 143–250, [arXiv:hep-ph/9805494](#).
- [171] T. G. Rizzo, “ Z' phenomenology and the LHC,” [arXiv:hep-ph/0610104](#).
- [172] P. Gupta, B. C. Choudhary, S. Chatterji, S. Bhattacharya, and R. K. Shivpuri, “Direct Photon plus Jet Study for CMS,” [arXiv:0705.2740 \[hep-ex\]](#).
- [173] M. Pieri *et al.*, “Inclusive search for the Higgs boson in the H to gamma gamma channel,”. CERN-CMS-NOTE-2006-112.
- [174] CDF Collaboration, A. Abulencia *et al.*, “Search for heavy, long-lived particles that decay to photons at CDF II,” *Phys. Rev. Lett.* **99** (2007) 121801, [arXiv:0704.0760 \[hep-ex\]](#).
- [175] D. M. Gingrich and K. Martell, “Study of highly-excited string states at the Large Hadron Collider,” *Phys. Rev.* **D78** (2008) 115009, [arXiv:0808.2512 \[hep-ph\]](#).
- [176] J. D. Lykken, “Weak scale superstrings,” *Phys. Rev.* **D54** (1996) 3693–3697, [arXiv:hep-th/9603133](#).
- [177] D. H. Perkins, “Introduction to High-Energy Physics,”. Reading, USA: Addison-Wesley (1982) 437p.

Appendix A: Units

In this thesis we use 3 different system of units: high energy, SI and natural. Table 1 shows the value of the fundamental constants in the 3 systems of units. Conversion factors between these 3 systems are summarised in Table 2.

Table 1: *Fundamental constants.*

Quantity	High energy units	SI units	Natural units
\hbar	6.588×10^{-28} GeV s	1.055×10^{-34} J s	1
c	2.998×10^{23} fm/s	2.998×10^8 m/s	1
G_4	6.707×10^{-39} GeV	$6.674 \times 10^{-11} \text{m}^3 \text{kg}^{-1} \text{s}^{-2}$	M_{PL}^{-2}

Table 2: *Conversion factors.*

Quantity	High energy units	SI units	Natural units
Length	1.97×10^{-20} fm	1.97×10^{-35} m	$1 M_{PL}^{-1}$
Mass	1.22×10^{19} GeV	1.78×10^{-8} kg	$1 M_{PL}$
Energy	1.22×10^{19} GeV	1.95×10^9 J	$1 M_{PL}$
Time	8.2×10^{-20} GeV ⁻¹	6.58×10^{-44} s	$1 M_{PL}^{-1}$
Temperature	1.22×10^{19} GeV	1.42×10^{32} K	$1 M_{PL}$

Appendix B: Acronyms

ADD	ArkaniHamed-Dimopoulos-Dvali
BD	Black Disk
BH	BlackHole
BR	Branching Ratio
CERN	European Organization for Nuclear Research
CL	Confidence Level
CM	Center-of-Mass
CP	Charge-Parity
dof	degrees of freedom
ED	Extra Dimension
GUT	Grand Unified Theory
KK	Kaluza-Klein
LED	Large Extra Dimension
LEP	Large Electron-Positron
LHC	Large Hadron Collider
LSP	Lightest Supersymmetric Particle
MC	Monte Carlo
MSSM	Minimal Supersymmetric extension of the SM
mSUGRA	minimum SuperGRAvity
OSOF	Opposite Sign Opposite Flavor
OSSF	Opposite Sign Same Flavor
PDF	Parton Distribution Function
QCD	Quantum ChromoDynamics
QED	Quantum ElectroDynamics
RS	Randall-Sundrum
SM	Standard Model
SR	String Resonance
SSOF	Same Sign Opposite Flavor
SSSF	Same Sign Same Flavor
ST	String Theory
SUSY	SUperSYmmetry
TS	Trapped Surface

Appendix C: Symbols

m_{bare}	Bare Higgs mass
m_{Higgs}	Physical Higgs mass
Λ (Sect. 1.2)	Higgs mass cutoff
X and μ (Sect. 1.2)	Momentum transfer scale
b_i	Numerical prefactors
m_0	common mass of scalar particles at M_{GUT}
$m_{\frac{1}{2}}$	common mass of gauginos and Higgsino at M_{GUT}
A_0	trilinear coupling at M_{GUT}
$\tan \beta$	ratio of vacuum expectation values of two Higgs fields
μ	sign of the Higgsino mass parameter
L(B)	Lepton (baryon) number
\mathbf{s}	Particle spin
n	Number of extra-spatial dimensions
R	Size of ED in ADD model
ψ	Scalar field
m_ψ	Mass of the scalar field
x_i	3 spatial coordinates
G_4	4-dimensional Newton's constant
G_{n+4}	(n+4)-dimensional Newton's constant
S_d	Surface area of unit sphere in d dimensions
F_4	Force between two test masses in 4 dimensions
F_{n+4}	Force between two test masses in (n+4) dimensions
D	Total number of dimensions
$\phi_{g(4)}$	4-dimensional gravitational potential
$\phi_{g(n+4)}$	(n+4)-dimensional gravitational potential
ρ_m	Mass density
V_n	Volume of ED in ADD model
x_n	Bessel function roots
Λ (Sect. 1.4.3)	Strength of graviton-matter coupling in RS model
σ	cross section
M_{PL}	Planck mass
M	BH mass
\hat{s}	Parton square CM energy
s	Particle square CM energy

Q (Sect. 1.5)	Momentum transfer scale
T_H	Hawking temperature
τ	BH lifetime
α'	Slope parameter
l_s	String length scale
M_s	String mass scale
g_s	String coupling
θ_W	Weinberg angle
p_z	Momentum along z axis
L	Luminosity
f	Proton bunch crossing frequency
n_b	Number of protons in each bunch
A	Bunch area
S	Sphericity
T	Thrust
R_2	Second Fox-Wolfram moment
E_{vis}	Visible energy
P_T	Transverse momenta
P_{Tmin}	Minimum transverse momenta
P_{Tl}	Transverse momenta of leptons
$P_{T\gamma}$	Transverse momenta of photons
\cancel{P}_T	Missing transverse momenta
\cancel{E}_T	Missing transverse energy
η	Pseudorapidity
